

2

AD-A258 884



WL-TR-91-4079

**MECHANICAL BEHAVIOR OF TITANIUM ALUMINIDE
UNDER ENGINE OPERATING CONDITIONS**

N. Jayaraman
SYSTRAN Corporation
4126 Linden Avenue
Dayton, Ohio 45432

August 1992

Final Report for Period 1 July 1988 - 30 September 1990

Approved for public release; distribution unlimited.

MATERIALS DIRECTORATE
WRIGHT LABORATORY
AIR FORCE SYSTEMS COMMAND
WRIGHT-PATTERSON AFB, OHIO 45433-6533

DTIC
ELECTE
DEC 21 1992
S E D

92-32389



129 ps

92 12 18 079

NOTICE

When Government drawings, specifications, or other data are used for any purpose other than in connection with a definitely Government-related procurement, the United States Government incurs no responsibility nor any obligation whatsoever. The fact that the government may have formulated, or in any way supplied the said drawings, specifications, or other data, is not to be regarded by implication or otherwise in any manner construed, as licensing the holder or any other person or corporation, or as conveying any rights or permission to manufacture, use, or sell any patented invention that may in any way be related thereto.

This report is releasable to the National Technical Information Service (NTIS). At NTIS, it will be available to the general public, including foreign nations.

This technical report has been reviewed and is approved for publication.



STEPHEN J. BALSONE
Project Engineer
Materials Behavior Branch
Metals and Ceramics Division

FOR THE COMMANDER



KATHERINE A. WILLIAMS
Technical Area Manager
Materials Behavior Branch
Metals and Ceramics Division



ALLAN W. GUNDERSON, Chief
Materials Behavior Branch
Metals and Ceramics Division

If your address has changed, if you wish to be removed from our mailing list, or if the addressee is no longer employed by your organization, please notify WL/MLLN, Wright-Patterson AFB, OH 45433-6533 to help us maintain a current mailing list.

Copies of this report should not be returned unless return is required by security considerations, contractual obligations, or notice on a specific document.

REPORT DOCUMENTATION PAGE				Form Approved OMB No. 0704-0188	
1a. REPORT SECURITY CLASSIFICATION Unclassified			1b. RESTRICTIVE MARKINGS None		
2a. SECURITY CLASSIFICATION AUTHORITY			3. DISTRIBUTION/AVAILABILITY OF REPORT Approved for public release; distribution is unlimited.		
2b. DECLASSIFICATION/DOWNGRADING SCHEDULE					
4. PERFORMING ORGANIZATION REPORT NUMBER(S)			5. MONITORING ORGANIZATION REPORT NUMBER(S) WL-TR-91-4079		
6a. NAME OF PERFORMING ORGANIZATION SYSTRAN Corporation		6b. OFFICE SYMBOL (If applicable)	7a. NAME OF MONITORING ORGANIZATION Wright Laboratory, Materials Directorate Materials Behavior Branch (WL/MLLN)		
6c. ADDRESS (City, State, and ZIP Code) 4126 Linden Avenue Dayton, OH 45432			7b. ADDRESS (City, State, and ZIP Code) Wright-Patterson AFB, OH 45433-6533		
8a. NAME OF FUNDING/SPONSORING ORGANIZATION Wright Laboratory Materials Behavior Branch		8b. OFFICE SYMBOL (If applicable) WL/MLLN	9. PROCUREMENT INSTRUMENT IDENTIFICATION NUMBER F33615-88-C-5408		
8c. ADDRESS (City, State, and ZIP Code) Wright-Patterson AFB, OH 45433			10. SOURCE OF FUNDING NUMBERS		
			PROGRAM ELEMENT NO. 65502F	PROJECT NO. 3005	TASK NO. 51
11. TITLE (Include Security Classification) Mechanical Behavior of Titanium Aluminide Under Engine Operating Conditions					
12. PERSONAL AUTHOR(S) N. Jayaraman, Ph.D., Professor Materials Science and Engineering, University of Cincinnati - Technical Consultant to SYSTRAN.					
13a. TYPE OF REPORT Final		13b. TIME COVERED From To 7/1/88 9/30/90		14. DATE OF REPORT (Year, Month, Day) 92/08	
15. PAGE COUNT 128					
16. SUPPLEMENTARY NOTATION This is a Small Business Innovation Report.					
17. COSATI CODES			18. SUBJECT TERMS (Continue on reverse if necessary and identify by block number) Fatigue Crack Growth Elevated Temperature Heat Treatment Titanium Aluminide Plus Niobium Environmental Influence Fractography		
FIELD	GROUP	SUB-GROUP			
13. ABSTRACT (Continue on reverse if necessary and identify by block number) A brief study to optimize the heat treatment for a useful balance of mechanical properties in Ti-25%Al-10%Nb-3%V-1%Mo (atomic percent) was conducted. The selected heat treatment consisted of solution treatment at 1115°C (in the $\alpha + \beta$ field, about 25°C below the transus temperature) in vacuum for 1 hour followed by cooling to room temperature in argon, followed by aging at 760°C in vacuum for 8 hours, followed by cooling at room temperature in argon. This treatment resulted in fine transformed microstructure with high (25%) volume fraction of primary α_2 -phase. This treatment resulted in superior fatigue crack growth resistance while still maintaining good tensile and creep properties. This solution + age heat treatment was used for study of the effects of several factors such as temperature (25, 425, 540, and 650°C), environment (air and ultrahigh vacuum), frequency (0.01 to 1 Hz), R-ratio (0.1 and 0.8), and orientation (parallel and perpendicular to the final rolling direction) on the fatigue crack growth behavior.					
20. DISTRIBUTION/AVAILABILITY OF ABSTRACT <input type="checkbox"/> UNCLASSIFIED/UNLIMITED <input type="checkbox"/> SAME AS RPT. <input type="checkbox"/> DTIC USERS			21. ABSTRACT SECURITY CLASSIFICATION Unclassified		
22a. NAME OF RESPONSIBLE INDIVIDUAL Stephen J. Balsone			22b. TELEPHONE 513-255-1346		22c. OFFICE SYMBOL WL/MLLN

19. ABSTRACT (cont.)

Both in air and in ultrahigh vacuum environments, fatigue crack growth rates were generally higher at higher temperatures between 425 °C and 650 °C. At room temperature, the crack growth rate was higher compared to the high-temperature growth rates, especially at higher stress intensity ranges. Crack closure effects were not significant in the crack growth process, particularly at low stress intensities. $K_{closure}$ values were found to increase with increasing K_{max} and in general $K_{closure}$ was about 10% of the K_{max} value. It is not clear whether the variation in $K_{closure}$ is associated with the increase in K_{max} or increase in crack length. This is due to the observation that at a constant K_{max} the crack growth rates were found to be slower at longer crack lengths. At elevated temperatures, crack growth rates in air environment are about an order of magnitude faster than in ultrahigh vacuum environment. Generally, the low temperature (25 °C and 425 °C) fracture mechanisms are crystallographic cleavage fracture. At high temperature, in air, the fracture surface showed evidence of fatigue striations and also evidence of extensive oxidation. In vacuum, the fracture mode was predominantly crystallographic cleavage with some evidence of tearing of α_2 -plates.

Fatigue crack growth rates were not affected by the orientation of the sample with reference to the final rolling direction of the plate material. The crack growth rates were not very different when tested in two orientations, parallel and normal to the final rolling direction. However, the alloy seems to be tougher in the longitudinal direction.

Fatigue frequency plays an important role in the crack growth rates at elevated temperatures. In general, slower crack growth was seen at higher frequencies. The frequency effect seems to be more pronounced when the conditions are generally favorable for slower crack growth, such as low K_{max} and R-ratio. This indicated that environment plays a significant role in the way frequency affects crack growth rate. There seems to be a crack growth rate dependence on the crack length at a constant K_{max} , R-ratio and frequency. This dependence could be due to either crack branching, crack-length-dependence closure, or both.

SUMMARY

The main objective of this program is to develop an understanding of the room-temperature and high-temperature mechanical behavior of α_2 -titanium aluminide in laboratory air and ultrahigh vacuum conditions. Under this program, a systematic study of the various aspects of structure - property - environment relationships relevant to the anticipated uses of this class of alloys has been conducted. The problems of fatigue, fracture and creep of α_2 -titanium aluminide have been addressed. The influence of parameters such as frequency, temperature, load amplitude and environment on crack growth behavior have also been addressed. This final report presents all of the data generated during the course of this program, and it presents comprehensive analyses and discussion of the research work performed under this program.

Initially, the effects of various heat treatment conditions was studied with the intent to optimize the microstructure for a useful balance of mechanical properties in Ti-25%Al-10%Nb-3%V-1%Mo (atomic percent). Tensile, creep, and fatigue crack growth studies were conducted on material subjected to three heat treatments A, B, and C. Heat treatment A consisted of a β -solution at 1175°C and slow cool to 816°C, followed by furnace cooling. This resulted in large colonies of transformed microstructure. Heat treatment B consisted of 1175°C solution and cooled in argon to room temperature followed by an 8 hour aging at 760°C. This resulted in fine transformed microstructure with large prior- β grains. Heat treatment C was done at 1115°C (in the α_2 - β region) and cooled in argon to room temperature followed by aging at 760°C. This resulted in fine transformed microstructure with high volume fraction of α_2 . In tensile fracture, the packet morphology of the coarse transformed structure dominated the fracture mechanism in the material with heat treatment A resulting in low strength, while the grain boundaries of the coarse prior β -grains play a major role in the fracture process for the material subjected to heat treatment B. In heat treatment C, the fine scale microstructural units govern the failure mode. The material subjected to heat treatment C showed superior creep resistance, compared to the other two heat treatments. Similarly, a comparison of the fatigue crack growth behavior showed that the material with heat treatment C has higher threshold and slower crack growth rates. Based on these observations, heat treatment C was selected for more detailed studies.

The selected heat treatment consisted of solution treatment at 1115°C (in the $\alpha+\beta$ field, about 25°C below the β -transus temperature of this specific alloy) in vacuum for 1 hour followed by cooling to room temperature in argon, followed by aging at 760°C in vacuum for 8 hours

followed by cooling to room temperature in argon. This treatment resulted in fine transformed microstructure with high (25%) volume fraction of primary α_2 -phase. This heat treatment resulted in superior fatigue crack growth resistance while still maintaining good tensile and creep properties.

This solution + age heat treatment was used for study of the effects of several factors such as temperature (25°C, 425°C, 540°C, and 650°C), environment (air, and ultrahigh vacuum), frequency (0.01 to 1 Hz), R-ratio (0.1, and 0.8) and orientation (parallel and perpendicular to the final rolling direction) on the fatigue crack growth behavior. Both in air and in ultrahigh vacuum environments fatigue crack growth rates were generally higher at higher temperatures between 425°C and 650°C. At room temperature, the crack growth rate was higher compared to the high-temperature growth rates, especially at higher stress intensity ranges. Crack closure effects were not significant in the crack growth process, particularly at low stress intensities. $K_{closure}$ values were found to increase with increasing K_{max} and in general $K_{closure}$ was about 10% of the K_{max} value. It is not clear whether the variation in $K_{closure}$ is associated with the increase in K_{max} or increase in crack length. This is due to the observation that at a constant K_{max} the crack growth rates were found to be slower at longer crack lengths. At elevated temperatures, crack growth rates in air environment are about an order of magnitude faster than in ultra-high vacuum environment. Generally, the low temperature (25°C and 425°C) fracture mechanisms are crystallographic cleavage fracture. At high temperature, in air, the fracture surface showed evidence of fatigue striations and also evidence of extensive oxidation. In vacuum, the fracture mode was predominantly crystallographic cleavage with some evidence of tearing of α_2 -plates.

Fatigue crack growth rates were not affected by the orientation of the sample with reference to the final rolling direction of the plate material. The crack growth rates were not very different when tested in two orientations, parallel and normal to the final rolling direction. However, the alloy seems to be tougher in the longitudinal direction.

Fatigue frequency plays an important role in the crack growth rates at elevated temperatures. In general, slower crack growth is obvious at higher frequencies. The frequency effect seem to be more pronounced when the conditions are generally favorable for slower crack growth, such as low K_{max} and high R-ratio. This indicates that environment plays a significant role in the way frequency affects crack growth rate. There seems to be a crack growth rate dependence on the crack length at a constant K_{max} , R-ratio and frequency. This dependence could be due to either crack branching, crack length dependent closure, or both.

FOREWORD

This research program was conducted under Air Force Small Business Innovation Research - Phase II research contract No. F33615-88-C-5408 "Mechanical Behavior of Titanium Aluminide Under Engine Operating Conditions." The Air Force Program Monitor was Mr. S. Balsone. This program has been performed by the SYSTRAN Corporation, Dayton, Ohio. The Principal Investigator for the period 1 July 1988 to 30 November 1989 was Dr. S.V. Ram. Dr. N. Jayaraman was the Principal Investigator since 11 December 1989. The Program Manager was Mr. M.E. Zellmer and Mr. J. Hanrahan is the Research Assistant.

This final report presents all the details of the studies conducted and the results obtained from the work performed under the contract for the entire period from 1 July 1988 through 31 December 1990.

Accession For	
NTIS CRA&I	<input checked="checked" type="checkbox"/>
DTIC TAB	<input type="checkbox"/>
Unannounced	<input type="checkbox"/>
Justification	
By	
Distribution /	
Availability Codes	
Dist	Avail and/or Special
A-1	

TABLE OF CONTENTS

	Page No.
SUMMARY - - - - -	iii
FOREWORD - - - - -	v
LIST OF FIGURES - - - - -	vii
LIST OF TABLES - - - - -	xii
INTRODUCTION - - - - -	1
 ALLOY PROCESSING AND SELECTION OF MICROSTRUCTURE TO OBTAIN BALANCED PROPERTIES - - - - -	 2
<i>Heat Treatment Studies and Microstructural Analyses</i>	
- Preliminary Screening	3
<i>Heat Treatment Studies and Microstructural Analyses</i>	
- Final Selection of Microstructure Based on Balanced Mechanical Properties	4
 EXPERIMENTAL TECHNIQUES - - - - -	 5
<i>Tensile Test Procedures</i>	6
<i>Creep Test Procedures</i>	6
<i>Fatigue Crack Growth Testing Procedure</i>	7
 MECHANICAL PROPERTIES OF Ti-25%Al-10%Nb-3%V-1%Mo ALLOY - EFFECT OF MICROSTRUCTURE AND FINAL SELECTION OF MICROSTRUCTURE FOR BALANCED PROPERTIES - - - - -	 9
<i>Tensile Test Results and Fractography</i>	9
<i>Creep Test Results and Fractography</i>	12
<i>Fatigue Crack Growth Test Results and Fractography</i>	13
 MECHANICAL BEHAVIOR OF Ti-25%Al-10%Nb-3%V-1%Mo ALLOY WITH FINE TRANSFORMED MICROSTRUCTURE - - - - -	 16
<i>Tensile Behavior - Effects of Environment and Temperature</i>	16
<i>Fatigue Crack Growth Behavior</i>	19
<i>Effect of Temperature and Environment</i>	19
<i>Effect of Orientation</i>	23
<i>Effect of Frequency and R-Ratio</i>	24
 CONCLUSIONS - - - - -	 28
 REFERENCES - - - - -	 30
 Figures 1 through 118	 31

LIST OF FIGURES

Figure No.		Page No.
1.	The as rolled microstructure.	31
2.	Heat treatment #1 - Solution at 1125°C(1 hr); Slow cool to 816°C; Furnace cool to RT.	32
3.	Heat treatment #2 - Solution at 1175°C(1 hr); Slow cool to 816°C; Furnace cool to RT.	33
4.	Heat treatment #3 - Solution at 1175°C(1 hr); Quench to 760°C and age for 8 hours; Furnace cool to RT.	34
5.	Heat treatment #4 - Solution at 1100°C(1 hr); Air cool to RT; Age at 760°C for 8 hours and cool to RT.	35
6.	Heat treatment #5 - Solution at 1125°C(1 hr); Cool in argon to RT; Age at 760°C for 8 hours and cool to RT.	36
7.	Heat treatment A - Solution at 1175°C(1 hr); Slow cool to 816°C; Furnace cool to RT.	37
8.	Heat treatment B - Solution at 1175°C(1 hr); Cool in argon to RT; age at 760°C for 8 hours; Cool in argon to RT.	38
9.	Heat treatment C - Solution at 1115°C(1 hr); Cool in argon to RT; age at 760°C for 8 hours; Cool in argon to RT.	39
10.	Tensile specimen	40
11.	Tensile creep specimen	40
12.	Metric compact tension specimen	41
13.	Ultra-high vacuum mechanical test facility.	42
14.	Compliance-measured crack length versus Optically-measured crack length.	43
15.	Typical example of a plot of crack length versus cycles for a decreasing-stress-intensity-threshold test.	44
16.	Typical example of a plot of crack length versus cycles for a constant-load-increasing-stress-intensity test.	45
17.	Typical load-displacement plot for a specimen exhibiting closure.	45
18.	Comparison of the elastic modulus at 25°C for the three heat treatments	46
19.	Comparison of the elastic modulus at 650°C for the three heat treatments	46
20.	Comparison of the yield strength at 25°C for the three heat treatments	47
21.	Comparison of the yield strength at 650°C for the three heat treatments	47
22.	Comparison of the UTS at 25°C for the three heat treatments	48
23.	Comparison of the UTS at 650°C for the three heat treatments	48
24.	Comparison of the % elongation at 25°C for the three heat treatments	49
25.	Comparison of the %elongation at 650°C for the three heat treatments.	49
26.	Tensile samples tested at RT in air - Heat treatment A.	50
27.	Tensile samples tested at RT in air - Heat treatment B.	51

LIST OF FIGURES

Figure No.		Page No.
28.	Tensile samples tested at RT in air - Heat treatment C.	52
29.	Tensile samples tested at 650°C in air - Heat treatment A.	53
30.	Tensile samples tested at 650°C in vacuum - Heat treatment A.	54
31.	Tensile samples tested at 650°C in air - Heat treatment B.	55
32.	Cross-sectional view of tensile sample tested at 650°C in air - Heat treatment B.	56
33.	Tensile samples tested at 650°C in vacuum - Heat treatment B.	57
34.	Tensile samples tested at 650°C in air-Heat treatment C.	58
35.	Tensile samples tested at 650°C in vacuum - Heat treatment C.	59
36.	Creep strain versus time plots for specimens tested from the three heat treatments.	60
37.	Creep rupture specimens tested at 650°C in air - Heat treatment A.	61
38.	Creep rupture specimens tested at 650°C in air - Heat treatment B.	62
39.	Creep rupture specimens tested at 650°C in air - Heat treatment C.	63
40.	da/dN vs ΔK for the three heat treatments at test temperature of 540°C	64
41.	da/dN vs $\Delta K_{\text{effective}}$ for the three heat treatments at test temperature of 540°C	64
42.	da/dN vs ΔK for the three heat treatments at test temperature of 650°C	65
43.	da/dN vs $\Delta K_{\text{effective}}$ for the three heat treatments at test temperature of 650°C	65
44.	Fatigue crack growth specimens tested at 650°C in air - Heat treatment A.	66
45.	Fatigue crack growth specimens tested at 540°C in air - Heat treatment A.	67
46.	Fatigue crack growth specimens tested at 650°C in air - Heat treatment B.	68
47.	Fatigue crack growth specimens tested at 540°C in air - Heat treatment B.	69
48.	Fatigue crack growth specimens tested at 650°C in air - Heat treatment C.	70
49.	Fatigue crack growth specimens tested at 540°C in air - Heat treatment C.	71
50.	Elastic modulus versus test temperature in air and ultra-high vacuum environment for heat treatment C.	72
51.	Yield strength versus test temperature in air and ultra-high vacuum environment for heat treatment C.	72
52.	UTS versus test temperature in air and ultra-high vacuum environment for heat treatment C.	73
53.	%elongation versus test temperature in air and ultra-high vacuum environment for heat treatment C.	73
54.	Tensile samples tested at 650°C in vacuum - Heat treatment C.	74
55.	Tensile samples tested at 540°C in vacuum - Heat treatment C.	75
56.	Tensile samples tested at 425°C in vacuum - Heat treatment C.	76
57.	Tensile samples tested at 315°C in vacuum - Heat treatment C.	77

LIST OF FIGURES

Figure No.		Page No.
58.	Tensile samples tested at 650°C in air - Heat treatment C.	78
59.	Tensile samples tested at 540°C in air - Heat treatment C.	79
60.	Tensile samples tested at 425°C in air - Heat treatment C.	80
61.	Tensile samples tested at 315°C in air - Heat treatment C.	81
62.	da/dN versus ΔK and da/dN versus $\Delta K_{\text{effective}}$ at test temperature of 25°C.	82
63.	K_{closure} versus K_{max} at test temperature of 25°C in air.	82
64.	da/dN versus ΔK and da/dN versus $\Delta K_{\text{effective}}$ at test temperature of 425°C in air.	83
65.	K_{closure} versus K_{max} at test temperature of 425°C in air.	83
66.	da/dN versus ΔK and da/dN versus $\Delta K_{\text{effective}}$ at test temperature of 540°C in air.	84
67.	K_{closure} versus K_{max} at test temperature of 540°C in air.	84
68.	da/dN versus ΔK and da/dN versus $\Delta K_{\text{effective}}$ at test temperature of 650°C in air.	85
69.	K_{closure} versus K_{max} at test temperature of 650°C in air.	85
70.	da/dN versus ΔK at test temperature of 540°C in ultra-high vacuum.	86
71.	da/dN versus ΔK at test temperature of 650°C in ultra-high vacuum.	86
72.	Summary of plots of da/dN versus ΔK for all the tests run in air.	87
73.	Summary of plots of da/dN versus $\Delta K_{\text{effective}}$ for all the tests run in air.	87
74.	Comparison of crack growth rates at 540°C between air and ultra-high vacuum environments.	88
75.	Comparison of crack growth rates at 650°C between air and ultra-high vacuum environments.	88
76.	Summary of plots of K_{closure} versus K_{max} showing the effect of test temperature in air - Constant load test condition.	89
77.	Summary of plots of K_{closure} versus K_{max} showing the effect of test temperature in air - Constant load and threshold test condition.	89
78.	Load-displacement of a typical fatigue crack growth test conducted in ultra-high vacuum showing the lack of closure effects.	90
79.	SEM fractographs of fatigue crack growth specimen at 25°C in air.	91
80.	SEM fractographs of fatigue crack growth specimen at 425°C in air.	92
81.	SEM fractographs of fatigue crack growth specimen at 540°C in air.	93
82.	SEM fractographs of fatigue crack growth specimen at 650°C in air.	94
83.	SEM fractographs of fatigue crack growth specimen at 650°C in ultra-high vacuum.	95
84.	da/dN versus ΔK and $\Delta K_{\text{effective}}$ for fatigue crack growth test done at 650°C - specimen S89C60V	96

LIST OF FIGURES

Figure No.		Page No.
85.	da/dN versus ΔK and $\Delta K_{\text{effective}}$ for fatigue crack growth test done at 650°C - specimen S89C70V	96
86.	da/dN versus ΔK and $\Delta K_{\text{effective}}$ for fatigue crack growth test done at 650°C - specimen S89C64V	97
87.	da/dN versus ΔK and $\Delta K_{\text{effective}}$ for fatigue crack growth test done at 540°C - specimen S89C61V	97
88.	da/dN versus ΔK and $\Delta K_{\text{effective}}$ for fatigue crack growth test done at 425°C - specimen S89C62V	98
89.	Summary of all the crack growth data for the transverse orientation.	98
90.	Kclosure versus Kmax for fatigue crack growth test done at 650°C for specimen with transverse orientation - Specimen S89C60V	99
91.	Kclosure versus Kmax for fatigue crack growth test done at 650°C for specimen with transverse orientation - Specimen S89C64V	99
92.	Kclosure versus Kmax for fatigue crack growth test done at 650°C for specimen with transverse orientation - Specimen S89C70V	100
93.	Kclosure versus Kmax for fatigue crack growth test done at 540°C for specimen with transverse orientation - Specimen S89C61V	100
94.	Kclosure versus Kmax for fatigue crack growth test done at 425°C for specimen with transverse orientation - Specimen S89C62V	101
95.	Typical examples of crack branching seen in the fatigue crack growth tests conducted at constant maximum stress -intensity, but at different frequencies - Specimen #S89C65	102
96.	Typical examples of crack branching seen in the fatigue crack growth tests conducted at constant maximum stress -intensity, but at different frequencies - Specimen #S89C18	103
97.	Typical examples of crack branching seen in the fatigue crack growth tests conducted at constant maximum stress -intensity, but at different frequencies - Specimen #S89C21	104
98.	Typical crack length versus cycles for a fatigue crack growth test conducted at constant maximum stress -intensity, but at different frequencies - specimen #S89C18	105
99.	Typical crack length versus cycles for a fatigue crack growth test conducted at constant maximum stress -intensity, but at different frequencies - specimen #S89C65	106
100.	Typical crack length versus cycles for a fatigue crack growth test conducted at constant maximum stress -intensity, but at different frequencies - specimen #S89C66	106
101.	Typical crack length versus cycles for a fatigue crack growth test conducted at constant maximum stress intensity, but at different frequencies - specimen #S89C21	107

LIST OF FIGURES

Figure No.		Page No.
102.	Typical crack length versus cycles for a fatigue crack growth test conducted at constant maximum stress intensity, but at different frequencies - specimen #S89C69&30	107
103.	da/dN versus frequency for test conducted at room temperature, K_{max} of 15 MPa√m, and R-ratio of 0.1.	108
104.	da/dN versus frequency for test conducted at a temperature of 425°C, K_{max} of 15 MPa√m, and R-ratio of 0.1.	108
105.	da/dN versus frequency for test conducted at a temperature of 650°C, K_{max} of 15 MPa√m, and R-ratio of 0.1.	109
106.	da/dN versus frequency for test conducted at a temperature of 650°C, K_{max} of 15 MPa√m, and R-ratio of 0.8.	109
107.	da/dN versus frequency for test conducted at a temperature of 650°C, K_{max} of 25 MPa√m, and R-ratio of 0.1.	110
108.	da/dN versus frequency for test conducted at a temperature of 650°C, K_{max} of 25 MPa√m, and R-ratio of 0.8.	110
109.	Summary of plots of da/dN versus frequency for test conducted under different set of conditions.	111
110.	Effect of temperature on the da/dN versus frequency plots for tests conducted at K_{max} =15 MPa√m, R=0.1.	111
111.	Effect of R-ratio on the da/dN versus frequency plots for tests conducted at 650°C and K_{max} =15 MPa√m.	112
112.	Effect of R-ratio on the da/dN versus frequency plots for tests conducted at 650°C and K_{max} =25 MPa√m.	112
113.	Effect of K_{max} on the da/dN versus frequency plots for tests conducted at 650°C and R-ratio=0.1.	113
114.	Effect of K_{max} on the da/dN versus frequency plots for tests conducted at 650°C and R-ratio=0.8.	113
115.	$K_{closure}$ versus crack length for fatigue crack growth tests conducted at constant K_{max} and constant R-ratio, but at different frequencies - specimen #S89C18	114
116.	$K_{closure}$ versus crack length for fatigue crack growth tests conducted at constant K_{max} and constant R-ratio, but at different frequencies - specimen #S89C65	114
117.	$K_{closure}$ versus crack length for fatigue crack growth tests conducted at constant K_{max} and constant R-ratio, but at different frequencies - specimen #S89C21	115
118.	$K_{closure}$ versus crack length for fatigue crack growth tests conducted at constant K_{max} and constant R-ratio, but at different frequencies - specimen #S89C69&30	115

LIST OF TABLES

Table No.		Page No.
1.	Summary of Preliminary Heat Treatment Conditions and the Microstructures	4
2.	Tensile Properties of Ti-25%Al-10%Nb-3%V-1%Mo after different heat treatments	10
3.	Creep Rupture Results for Ti-25%Al-10%Nb-3%V-1%Mo at 650°C	12
4.	List of Specimens and Test Conditions Used for Selection of Heat Treatment.	15
5.	Tensile Data for Ti-25%Al-10%Nb-3%V-1%Mo Alloy (Heat Treatment C)	17
6.	Summary of Fatigue Crack Growth Experiments (Heat Treatment C)	20

INTRODUCTION

Improvements in high performance aircraft gas turbine engines require materials that can operate at increasingly higher temperatures over long periods of time. Materials with high strength-to-weight ratio are essential to meet these requirements. In the past, major advances in engine technology have been made using nickel- and cobalt- base superalloys and the conventional α - β titanium alloys. With the anticipated future engine design requirements surpassing the capabilities of these materials, there is a need for the development of new classes of lightweight materials with superior elevated temperature performance. Titanium-based intermetallic compounds have been identified as possible materials with such superior weight specific properties.

The main benefit of intermetallic compounds is their superior strength properties over a wide range of temperature up to almost their melting points. However, a major limitation is the lack of ductility and toughness particularly at lower temperatures. One compound that is of considerable interest to the US Air Force is the α 2-titanium aluminide (Ti_3Al). This intermetallic has been extensively investigated by the Wright Laboratory Materials Directorate and major engine manufacturers(1,2). These studies have shown that significant weight savings and improved engine performance can be achieved by using these materials.

The α 2-titanium aluminide in the ordered state is stiffer than conventional titanium-based alloys, and these mechanical properties continue to be good even at elevated temperatures(3). This compound has both excellent oxidation resistance and good creep strength at elevated temperatures(4,5). These superior properties are generally attributed to the strong inter-atomic bonding between the titanium and aluminum atoms. Attempts have been made to improve the ductility of α 2-titanium aluminide through alloy additions such as niobium, tungsten, etc., which has made possible the mechanical processing of large ingots(6).

In order for the Air Force to fully exploit the potential of this class of materials, there has been a need to understand their behavior under complex stress/temperature/environment/time conditions. One particular area of interest is the crack growth behavior of these materials. A basic understanding of the crack growth is needed for

application to design and life management procedures. For example, both the Retirement For Cause (RFC) and Engine Structural Integrity Program (ENSIP) require life prediction analyses based on reliable crack growth rates. Under the RFC design philosophy, periodic inspection of critical components need to be made to monitor the formation and growth of damage (i.e., cracks) at critical locations, and the part will not be taken out of service (retired) until the critical damage state is reached. The inspection intervals are designed based on extensive knowledge of the crack growth behavior of the material used. Generally, these are obtained from crack growth experiments conducted under realistic engine operating conditions of sustained load, cyclic load, elevated temperatures, and different environments. This research program follows a similar concept of crack growth studies on laboratory scale specimens made of α 2-titanium aluminide alloy to determine the suitability of this material for engine applications.

The main objective of this program is to develop an understanding of the room-temperature and high-temperature mechanical behavior of α 2-titanium aluminide in laboratory air and ultrahigh vacuum conditions. Under this program, a systematic study of the various aspects of structure - property - environment relationships relevant to the anticipated uses of this class of alloys has been conducted. The problems of fatigue, fracture and creep of α 2-titanium aluminide have been addressed. The influence of parameters such as frequency, temperature, load amplitude and environment on crack growth behavior have also been addressed. Most of the results have been presented in several half-yearly reports (7-9). This final report presents all of the data generated during the course of this program, and it presents comprehensive analyses and discussion of the research work performed under this program.

ALLOY PROCESSING AND SELECTION OF MICROSTRUCTURE TO OBTAIN BALANCED MECHANICAL PROPERTIES

Fifty pounds of Ti-25%Al-10%Nb-3%V-1%Mo (all in atom %) alloy was procured from Alta Group, Fombell, PA. The alloy was double-melted from high-purity raw materials into a 6-inch-diameter ingot with the following impurity specifications: Fe < 0.004%, O < 0.08%, N < 0.02% (all in weight %) and all other impurity elements < 0.1 gram in the ingot. This ingot was then forged into a 2-inch thick slab. The forging was started at a temperature between 1150°C and 1205°C and was

finish forged at about 1040°C in order to obtain a $\alpha_2 + \beta$ microstructure. The β -transus temperature for this alloy chemistry is quoted as 1099°C (12). The slab was further rolled down to 1 inch thick plate at 1040°C in 15% reduction per pass and was finally sectioned and cross-rolled to 13-mm thick plate again at 1040°C in 15% reduction per pass. The final product was in the form of five plates of dimensions 330 mm X 165 mm X 13 mm. Plates were in good condition with no visible defects or cracks. The as-rolled microstructure of the material, as shown in Figure 1, contained elongated primary α_2 in the final rolling direction and fine grain size resulting from forging and rolling in the $\alpha_2 + \beta$ phase field. The cross-rolling of the slabs was designed to minimize the effects of preferred orientation that result from the rolling operation. However, it appears from some of the results of this study that cross-rolling did not fully remove preferred orientation effects. For example, although the crack growth rates were not significantly affected between different orientations in the material, the toughness was greater along the final rolling direction compared to the transverse direction.

Heat Treatment Studies and Microstructural Analyses - Preliminary Screening

The purpose of the preliminary heat treatment study was to determine the effects of solution and aging treatment temperatures on the microstructure of the alloy and to select three heat treatment schedules for more detailed analyses. One of these three heat treatments was then selected for further studies, based on the microstructure and some preliminary tensile, creep, and fatigue crack growth data for the alloy with the three different microstructures. Several small coupons of size 10 mm X 10 mm X 10 mm were cut for preliminary heat treatment and microstructural analysis. The heat treatment conditions and the resulting microstructures are summarized in Table 1. Details of the microstructures are available in the first half-yearly report (7), and they are also presented in Figures 2 through 6. These results show that the alloy from this study has a β -transus temperature well above the previously reported 1099°C(12). In fact, even after solution treatment at 1125°C followed by furnace cooling or aging, the microstructure consisted of primary α_2 and transformed microstructures. Only solutionizing at 1175°C yielded large prior β -grains, a clear indication of β -solution treatment. This leads to the conclusion that the β -transus temperature is in between 1125°C and 1175°C.

Table 1. Summary of Preliminary Heat Treatment Conditions and the Microstructures

Heat Treatment	Microstructures
1. Solutionize at 1125°C/1hr Slow cool (0.04°C/sec.) to 816°C Furnace cool to room temperature. (All done in a vacuum furnace)	Large volume (about 25%) of primary α_2 + coarse transformed α_2 + β (indicates that the solution treat was below β -transus)
2. Solutionize at 1175°C/1hr Slow cool (0.04°C/sec.) to 816°C Furnace cool to room temperature. (All done in vacuum furnace)	Large prior β grains + primary α_2 decorating g.b.s Coarse transformed struct. was found in large colonies.
3. Solutionize at 1175°C/1hr Quench to 760°C and age for 8hrs. (All done in vacuum encapsulated quartz tube)	Large prior β grains + fine Widmanstätten struct. No primary α_2 .
4. Solutionize at 1100°C/1hr Air cool to room temperature Age at 760°C/8hrs and cool. (All done in vacuum encapsulated quartz tube)	Fine transformed α_2 + β struc. Large volume fraction (about 25%) of primary α_2 .
5. Solutionize at 1125°C/1hr Air cool to room temperature Age at 760°C/8hrs and cool. (All done in vacuum encapsulated quartz tube)	Coarse transformed α_2 + β struc. Low volume fraction (about 10%) of primary α_2 .

Heat Treatment and Microstructure Analyses - Final Selection of Microstructure Based on Balanced Mechanical Properties

Based on microstructural analyses of these five heat treatments, the following three heat treatment conditions were identified for further analyses.:

Heat Treatment A - Beta solution at 1175°C for 1 hr in vacuum and slow cool at 0.04°C/second to 816°C and then furnace cool to room temperature. This resulted in a large colony of transformed microstructure.

Heat Treatment B - Beta solution at 1175°C for 1 hr in vacuum and cool in argon atmosphere to room temperature; age at 760°C for 8 hrs in

vacuum and cool to room temperature in argon. This resulted in a fine transformed microstructure with large prior β grains.

Heat Treatment C - α_2 + β solution at 1115°C for 1 hr in vacuum and cool to room temperature in argon; age at 760°C for 8 hrs in vacuum and cool to room temperature in argon. This resulted in a fine transformed microstructure with large volume fraction of primary α_2 . The solution temperature of 1115°C, is in the 2-phase region of the alloy of this study, since the β -transus temperature was found to be above 1125°C, which is well above the previously reported value of 1099°C(12).

These three heat treatments were conducted on plates of dimension 175 mm X 150 mm X 13 mm at Metal Treating Corporation, Cincinnati, Ohio. Results of the microstructural analyses are presented in Figures 7, 8, and 9. Mechanical properties of specimens with these three microstructures were evaluated. The test procedures are described in the next section on Experimental Techniques, and the results of the testing are presented in the following sections. As we will see later, heat treatment C was considered to produce a microstructure that would give balanced mechanical properties, such as tensile, creep, and fatigue crack growth. Based on this selection of microstructure, more detailed tensile and fatigue crack growth behaviors of this alloy were studied, and results of these are presented in the following sections.

EXPERIMENTAL TECHNIQUES

Tensile, creep-rupture, and fatigue crack growth behavior of this alloy after the three heat treatments were studied with the intent of selecting one of the heat treatments for more detailed examination. Then based on the selection of the heat treatment C as the one that produces the desired microstructure, more detailed tensile and fatigue crack growth experiments were performed. For this purpose, sub-sized round tensile specimens (Figure 10), tensile creep rupture specimens (Figure 11), and metric compact tension specimens (Figure 12) were fabricated from each of the heat-treated plates at the Trutex Corporation, Cincinnati, Ohio, using EDM (Electro-Discharge Machining) followed by low-stress grinding. All tensile and creep specimens were fabricated with the loading axis parallel to the final rolling direction. Majority of the specimens for fatigue crack growth (i.e., compact tension

specimens) were made with the loading axis parallel to the final rolling direction. A few compact tension specimens were made with the loading axis perpendicular to the rolling direction. These specimens were used to determine the effect of orientation with respect to rolling axis on the crack growth behavior of these alloys.

Tensile Test Procedures:

Tensile tests under stroke control were conducted on the sub-sized round tensile specimens at temperatures between room temperature ($RT \approx 25^{\circ}\text{C}$) and 650°C in air and in ultrahigh vacuum (3×10^{-9} torr) environment at a slow strain rate of 8.33×10^{-5} mm/mm in computer controlled close-looped servo-hydraulic mechanical testing machines. Since the ultrahigh vacuum mechanical test system is a unique system, a picture of the system is shown in Figure 13. We used MTS extensometers at gage lengths of 12.7 mm (with quartz rod extension arms) for air and 16 mm (with alumina rod extension arms) for vacuum, and the load-displacement data were collected. In the case of air tests, the extensometer was mounted from outside of the furnace, while for vacuum tests the whole extensometer system was mounted inside the vacuum chamber. Tests in air atmosphere were conducted in a test frame equipped with a box-type resistance heating oven, while the ultrahigh vacuum tests were conducted using a 12-kilowatt induction heating unit. In both cases, the temperature of the specimen was monitored by a thermocouple spot-welded to the specimen. The ultrahigh vacuum usually resulted in a vacuum of better than 3×10^{-9} torr with a typical gas composition of $\text{H}_2(2.0 \times 10^{-10}$ torr), $\text{N}(9.0 \times 10^{-12}$ torr), $\text{O}(9.3 \times 10^{-11}$ torr), $\text{OH}^+(4.3 \times 10^{-10}$ torr), $\text{H}_2\text{O}(1.8 \times 10^{-9}$ torr), $\text{N}_2(2.4 \times 10^{-10}$ torr), $\text{O}_2(3.2 \times 10^{-11}$ torr), and $\text{CO}_2(1.6 \times 10^{-10}$ torr). Mechanical properties such as elastic modulus, 0.2% yield strength, ultimate tensile strength and strain to failure were determined from the stress-strain data. Tensile tests were conducted at room temperature and 650°C from specimens subjected to heat treatments A, B, and C in order to select the appropriate heat treatment for further studies. More detailed testing at room temperature, 315, 425, 540, and 650°C was done for the selected microstructure (from heat treatment C).

Creep Test Procedures

Creep rupture behavior at 650°C in air environment for the three microstructure conditions (corresponding to heat treatments A, B, and C) was examined using an Arcweld sustained-load creep frame with 9070 kg (20 kips) capacity and 20 to 1 lever arm ratio. Tensile creep-rupture

specimens of dimensions shown in Figure 12 were used. Constant load creep tests were conducted; stress changes continually during test as specimen deforms. The creep elongation was measured using a LVDT extensometer with a gage length of 50.4 mm. The specimen was heated by an electrical resistance furnace. One set of creep rupture tests were conducted at a constant load having an initial stress level of 380 MPa, and another set was conducted at a constant load having an initial test stress/yield strength ratio of 0.64 (about 2/3rds of the yield strength). This resulted in initial stresses of 223, 380, and 310 MPa, respectively for the specimens subjected to heat treatments A, B, and C. While the tests conducted at 380 MPa enabled a comparison of the relative creep behavior at one initial stress level, the tests conducted at a initial fixed fraction of the yield strength might be considered as a fair comparison of the relative creep behavior. Details of these results along with the corresponding fracture mechanisms are discussed in the next section.

Fatigue Crack Growth Testing Procedure

Fatigue crack growth tests were conducted for all three heat treatments using the metric compact tension specimens (Figure 11). Two types of fatigue crack growth tests were conducted, a decreasing stress intensity threshold test and a constant load amplitude increasing stress intensity test. For the microstructural screening, tests were conducted on specimens from the three heat treatments only at 540 and 650°C in laboratory air environment. More detailed testing at room temperature, 425, 540, and 650°C was done for the selected microstructure (from heat treatment C). Effects of orientation, frequency, and R-ratio were also examined. The details of the fatigue crack growth experiments are presented below. These same procedures were used for the more extensive studies on the selected microstructure described later in this report.

Fatigue crack growth tests were conducted in an automated servo-hydraulic MTS test machine under computer control. The specimen was maintained at constant temperature in resistance heated oven with windows for observing the crack growth using a traveling microscope. The primary crack length data were obtained using compliance measurements from the load-displacement data. Crack mouth opening displacements were obtained with the aid of an extensometer with quartz rod extension arms. The extensometer was mounted outside the oven. Compliance was determined from a least-squares linear fit over a range from 90% of maximum load to a lower window of 60% of

maximum load, which in all cases was above the observed closure loads. The compliance determined crack lengths were verified through optical surface crack length measurements. Typical plot of crack length determined by optical measurements versus crack length measured by compliance measurements is shown in Figure 14. As shown in this plot, the optical crack lengths are within 400 microns (this being the worst case) of the compliance measured crack length. Generally the optically measured cracks are shorter than the compliance crack lengths. This could be attributed to some crack tunneling that may be present. Sinusoidal wave-forms with a frequency of 1Hz and a R-ratio ($\sigma_{\min}/\sigma_{\max}$) of 0.1 were used for all of the tests in this preliminary screening of microstructures. Initially the specimen is precracked at test temperature following the ASTM Standard E647. Following the precracking, decreasing-stress-intensity-threshold test was initiated. These tests involved load shedding with crack growth following the relationship

$$\Delta K = \Delta K_o \exp \{c(a-a_o)\}$$

where ΔK_o is the initial stress intensity range, c is a constant with a unit of reciprocal length, a is crack length at any given time, and a_o is the initial crack length. A starting stress intensity of $10.9 \text{ MPa}\sqrt{\text{m}}$ ($10 \text{ ksi}\sqrt{\text{in}}$) and the c parameter of 78.74 /meter (-2 /inch) was used. Load shedding was continued according to the above equation until crack arrest occurred. In general, we considered the crack arrested when there was no crack growth over a period of 1 to 3 days. The constant load amplitude test was then conducted at the end of the threshold test after crack arrest occurs. Typical examples of plots of crack length versus cycles are shown in Figures 15 and 16. These examples show that the end of threshold test is identified when the crack length versus cycles plot reaches a plateau.

Closure measurements were made during all of the above mentioned tests. At set intervals, traces of load versus displacement and load versus differential displacement were recorded. Crack closure load values were determined from the unloading portion of the fatigue cycle using an intercept method which defines the closure load at the intersection of the slope lines drawn along the two linear sections of the load differential displacement plot. Figure 17 shows a typical load-displacement plot in a specimen exhibiting closure. In general, the fatigue crack growth tests conducted in ultrahigh vacuum test conditions showed very little closure, while those run in air

environment showed some closure (with $K_{closure}$ around 10% of the K_{max}). The exact mechanisms contributing to closure are not clear. However, the experiments conducted to evaluate the frequency effect indicated that closure may be dependent on crack-length (even at constant K_{max}), and this was attributed to the crack branching observed under some fatigue crack growth conditions. These aspects are discussed in more detail later in this report.

The fatigue crack growth data for both the threshold and the constant load amplitude tests were reduced to the form of da/dN versus ΔK using a modified incremental polynomial method (10). This procedure limits the scatter normally obtained using an ASTM standard seven point polynomial, especially below the 'knee' portion of the da/dN versus ΔK plot. In general, for most of the crack growth analyses, both threshold type test and constant load amplitude test were performed using the same specimen. In addition, duplicate or triplicate specimens were tested under the same conditions to assure reproducibility of data and also to cover the entire range of ΔK values. From the fatigue crack growth experiments, a number of different data correlations have been made. Typically, da/dN vs ΔK , $K_{closure}$ vs K_{max} , da/dN vs $\Delta K_{effective}$ are plotted from these experiments.

MECHANICAL PROPERTIES OF Ti-25%Al-10%Nb-3%V-1%Mo ALLOY - EFFECT OF MICROSTRUCTURE AND FINAL SELECTION OF MICROSTRUCTURE FOR BALANCED PROPERTIES

This section will discuss mechanical test results along with fractographic and metallographic information for the initial phase of the program to select the optimum microstructure for a balance of properties. More detailed test results and discussion on the selected microstructure are described in the latter part of this section.

Tensile Test Results and Fractography

The tensile data for all three heat treatment (microstructural) conditions are listed in Table 2. A minimum of two specimens were tested for all but one heat treatment condition. These mechanical properties are also plotted as bar-graphs in Figures 18 through 25. Figures 18 and 19 compare the elastic moduli of the three heat-treated alloys at 25°C and 650°C respectively. Figures 20 through 25 make similar comparison for the yield strengths, UTS and %elongation.

Table 2. Tensile Properties of Ti-25%Al-10%Nb-3%V-1%Mo after different heat treatments.

Specimen No. (Heat Treatment)	Test Temp. °C, (Env)	Modulus GPa	Yield Strength MPa	UTS MPa	% Elong.
A4-1 (A)	25(Air)	112	567	577	0.73
A4-2 (A)	25(Air)	104	542	576	0.92
B4-1 (B)	25(Air)	114	851	951	1.80
B4-2 (B)	25(Air)	112	809	917	1.80
C4-1 (C)	25(Air)	133	727	818	1.18
C4-3 (C)	25(Air)	120	670	762	1.31
A4-3 (A)	650(Air)	88	348	438	2.78
A4-4 (A)	650(Air)	82	347	468	3.22
A4-5 (A)	650(Vac)	--	396	586	13.82
A4-6 (A)	650(Vac)	--	435	632	9.80
B4-3 (B)	650(Air)	88	603	756	3.09
B4-4 (B)	650(Air)	88	582	748	4.05
B4-5 (B)	650(Vac)	97	696	876	14.30
B4-6 (B)	650(Vac)	97	827	869	8.11
C4-2 (C)	650(Air)	87	461	610	5.15
C4-4 (C)	650(Air)	101	513	676	4.02
C4-5 (C)	650(Air)	99	483	632	5.18
C4-6 (C)	650(Vac)	92	550	841	12.90

We made some general observations from these tensile data. For a given heat treatment, modulus, and strength values at room temperature are higher than at elevated temperature. However, the ductility is better at elevated temperature. While the modulus was relatively unaffected by the ultrahigh vacuum environment, both strength and ductility seem to show significant improvement under ultrahigh vacuum environment. At room temperature, the elastic modulus was the highest for the microstructural condition

corresponding to heat treatment C with intermediate strength and ductility, and at 650°C, this heat treatment condition showed relatively high modulus combined with intermediate strength and elongation, both in air and ultrahigh vacuum environment. These observations seem to be consistent with the microstructures obtained for the different heat treatment conditions. For example, both the material subjected to heat treatment conditions A and B were solution treated in the single phase β -region while the material subjected to heat treatment C was solution treated in the 2-phase ($\alpha+\beta$) region. Thus, only the microstructure resulting from heat treatment C contained a controlled amount of primary α_2 -phase, uniformly distributed in the microstructure. The presence of primary α_2 -phase appears to be contributing to the increased elastic modulus and high temperature ductility, while maintaining reasonable strength levels.

In general, fractographic analyses supported these correlations. Figures 26 through 28 show the tensile fracture appearance of the three heat-treated materials tested at room temperature. Brittle fracture was the basic mechanism in all cases. However, in the case of coarse transformed structure (heat treatment A), the fracture surface was tortuous, following the packet type microstructural morphology (Figures 7 and 26) as compared to the flat fracture surface for heat treatment C (Figure 28). For the fine transformed structure (heat treatment B), the fracture path followed the prior beta grain morphology (Figure 27). The coarse transformed structure (heat treatment A) also exhibited rough fracture surface at 650°C when tested in air, Figure 29. Though a few surface cracks were visible, the extent of such cracking was much less when compared to that found in Ti-24%Al-11%Nb (a/o) alloy (11). Brittle failure at the microstructural scale was also observed as shown in Figure 29. We saw no surface cracking in vacuum tested sample for heat treatment A, as indicated in Figure 30. The fracture surface was still tortuous following packet morphology, and ductile areas along lath boundaries were observed with brittle failure within α_2 laths, as evidenced by the quasi-cleavage fracture features in α_2 laths. Secondary cracks along grain boundaries were observed in the case of fine transformed structure (heat treatment B) material, when tested in air at 650°C, Figure 31. The grain boundary separation for this case is clearly indicated in the cross sectional view of the fracture surface shown in Figure 32. Although major fracture mode was brittle failure, as indicated by the macroscopically crystalline fracture feature in Figure 31a and quasi-cleavage in Figure 31b, we saw some ductile features, as evidenced by the dimples seen in Figure 31c. The brittle and ductile features are actually seen on different grain facets. The

vacuum tested sample also showed grain boundary separation as shown in Figures 33c and 33d. Heat treatment C provided a flat fracture surface as indicated in Figure 34 for a test at 650°C in air. Brittle fracture morphology was observed in this case. Texture from rolling is also visible on the fracture surface. The vacuum tested sample for this heat treatment showed slightly rough fracture surface at 650°C with ductile failure morphology as shown in Figure 35. Brittle failure of the primary α_2 is also visible in Figure 35b. In summary, for heat treatment A, the packet morphology of the coarse transformed structure dominates the fracture mechanism, resulting in low strength, while the grain boundaries of the coarse prior beta grains play a major role in the fracture process of heat treatment B. In heat treatment C, the fine scale microstructural units govern the failure mode.

Creep Test Results and Fractography

Test results are presented in Table 3. Figure 36 shows the plots of corresponding creep strain versus time for the specimens tested.

Table 3. Creep Rupture Results for Ti-25%Al-10%Nb-3%V-1%Mo at 650°C

Heat Treat	Stress, MPa ($\sigma_{\text{applied}}/\sigma_{\text{ys}}$)	Rupture time, Hrs	Elongation, %
A	380 (1.1)	25.50	2.6
A	223 (0.64)	331.17*	0.8
B	380 (0.64)	171.97	2.0
C	380 (0.80)	209.87	3.6
C	310 (0.64)	404.58*	1.9

*Note: Did not rupture; test suspended.

Although only a limited number of creep tests were conducted, some interesting observations can be made. The creep behavior of the alloy with three different microstructures were examined at a constant initial stress of 380 MPa and at a constant initial stress of 0.64 times the yield strength. The former test condition helped to determine the relative creep life and failure strain for a constant initial stress for all microstructural conditions, while the latter test condition made a similar comparison possible for a initial test stress normalized with respect to the corresponding yield strength. At the constant initial test stress of 380 MPa, the microstructure from heat treatment condition B, with fine

transformed microstructure, and coarse prior β grain size had the highest creep resistance, while heat treatment condition A, with coarse transformed microstructure showed the least resistance. Heat treatment C had intermediate creep resistance. It also showed maximum creep ductility among the three heat treatments, an observation very similar to the previously observed tensile ductility at 650°C. In contrast, at constant initial test stress to yield strength ratio of 0.64, the microstructure from heat treatment B showed the least creep resistance and that from A showed the highest creep resistance.

Fractographic analyses of creep-tested specimens supported these observations. In beta solutioned materials, fine Widmanstätten α_2 platelets provide superior creep resistance (11 and 12). However, the amount of retained beta phase is also critical in controlling the improvement in creep behavior. The creep data obtained in this study are consistent with this finding. The coarse α_2 platelets in the case of heat treatment A results in poor creep resistance while fine transformed microstructure from heat treatment B provides superior creep resistance at 650°C and 380 MPa. The presence of primary α_2 phase from heat treatment condition C provides this microstructure with the intermediate creep resistance in the stress range studied here. Fractographic results are presented in Figures 37 through 39. These show the creep-rupture morphologies for the three heat-treated microstructures tested at 650°C and at 380 MPa. Brittle failure mode was observed for the heat treatment condition A (37), with the fracture path following the packet type microstructural features. Considerable secondary cracking was also observed, since the stress level was much higher than the yield strength. For microstructure from heat treatment B, strong influence of the grain size is shown in Figures 38a and 38b. Brittle intergranular fracture morphology was observed in initiation region while the fast crack regions appeared to show some ductility (Figure 38d). We saw moderately ductile transgranular fracture in the case of the material with heat treatment C, while the secondary cracking was absent (Figure 39).

Fatigue Crack Growth Test Results and Fractography

A list of specimens tested for the different microstructures is given in Table 4. Results from these fatigue crack growth experiments are summarized in da/dN vs ΔK plots in Figures 40 and 41 for 540°C, and Figures 42 and 43 for 650°C. In these figures, both measured ΔK

($K_{\max} - K_{\min}$) and the closure corrected ΔK ($K_{\max} - K_{\text{closure}}$) have been plotted. K_{closure} values were determined by obtaining the closures loads as described earlier and computing the corresponding K values. In addition, fractographic analyses were performed on specimens tested from all three heat treatments and at the two temperatures.

The following observations may be made from these preliminary fatigue crack growth data. In general, at 540°C, the crack growth rates for the three heat treatments are similar. However, the material subjected to heat treatment B showed a lower threshold stress intensity range ($4 \text{ MPa}\sqrt{\text{m}}$) as compared to the material subjected to the other two heat treatments ($5.5 \text{ MPa}\sqrt{\text{m}}$). At 650°C, the material subjected to heat treatment B showed not only lower threshold value ($4 \text{ MPa}\sqrt{\text{m}}$) but also much higher crack growth rates compared to the material subjected to the other two heat treatments. At this temperature, the material subjected to heat treatment C showed the slowest crack growth rates. In general, the closure effects are minimum in these heat treatments, i.e., as indicated earlier, K_{closure} was less than 10% of the K_{\max} value, and as a result, the da/dN vs $\Delta K_{\text{effective}}$ plots were only slightly different from the da/dN vs ΔK plots.

The crack growth process was dominated by the packet morphology of the coarse transformed structure (heat treatment A) as illustrated in fractographs in Figures 44 and 45. The fracture appearance corresponds to α_2 platelet microstructure (Figures 44c and 45c). In contrast, the prior β grain boundaries dominated the crack growth process for the microstructure obtained from heat treatment B, as shown in Figures 46 and 47. However, the failure morphology is slightly ductile and it corresponds to the sub-grain microstructure, as seen in Figures 46c and 47c. The fine transformed structure along with primary α_2 phase resulting from heat treatment C (Figures 48 and 49) appears to be responsible for the improved fatigue crack growth behavior. For all of these heat treatment conditions, the fracture surface is relatively flat, as seen in the low magnification fractographs (Figures 44a, 46a and 48a). However, for heat treatment conditions A and B, the prior β grain size is large and the whole microstructure is dominated by the transformed Widmanstatten plates. The resulting fracture at the microscopic level is dominated by fracture through these plates. In contrast, for the heat treatment condition C, the microstructure is a mixture of prior α_2 and fine transformed structure, both of which participate in the fracture process. This is evident in figures 48b and 49b. Based on these observations, the microstructure corresponding to

heat treatment condition C shows excellent fatigue crack growth properties and a good combination of tensile, and creep properties. One of the main thrusts of this study is to evaluate the fatigue crack growth behavior of the alloy and therefore, the heat treatment condition that showed the best fatigue crack growth behavior was chosen for further study.

Table 4. List of specimens and test conditions used for selection of heat treatment / resulting microstructure

Specimen No.	Heat Treatment	Test Temp.	Test Types
sa1	A	650°C	Threshold, Const. Ampl.
sa3	A	650°C	Threshold, Const. Ampl.
sa2	A	540°C	Threshold, Const. Ampl.
sa4	A	540°C	Threshold, Const. Ampl.
sb3	B	650°C	Threshold
sb4	B	650°C	Threshold Const. Ampl.
mb1	B	540°C	Threshold
mb2	B	540°C	Threshold Const. Ampl.
sc2	C	650°C	Threshold, Const. Ampl.
sc3	C	540°C	Threshold, Const. Ampl.

MECHANICAL BEHAVIOR OF Ti-25%Al-10%Nb-3%V-1%Mo ALLOY WITH FINE TRANSFORMED MICROSTRUCTURE CONTAINING PRIMARY α_2 PARTICLES

Based on the microstructural information obtained from five different heat treatments, three heat treatments (A, B, and C) were selected for more detailed evaluation of mechanical properties. We examined tensile properties in air atmosphere at room temperature and 650°C and in ultra-high vacuum environment at 650°C. We determined creep rupture properties at 650°C in air atmosphere were determined. Fatigue crack growth behavior in air at 540°C and 650°C. Based on the superior fatigue crack growth behavior, and intermediate tensile and creep properties, the material condition for heat treatment C (with resulting fine transformed microstructure distributed in primary α_2) was selected for studying more detailed tensile behavior and fatigue crack growth behavior considering the effects of temperature, frequency, R-ratio, environment, and crack orientation. Results of these studies are presented in the following sections.

Tensile Behavior - Effects of Environment and Temperature

Tensile tests were performed using closed-loop controlled servo-hydraulic MTS mechanical testing machines both in air and ultra-high vacuum environments, at several temperatures in the range between room temperature and 650°C. Again, tensile specimens similar to the ones described in the previous section were made with the loading axis parallel to the final rolling direction. The test conditions used are similar to the ones described earlier. All the tests were performed under stroke control with a nominal strain rate of 8.33×10^{-5} mm/mm/s. From these tensile tests, properties such as elastic modulus, 0.2% offset yield strength, ultimate tensile strength, and % elongation were determined. Results of these tests are presented in Table 5 and also in Figures 50 to 53. Figure 50 shows a plot of elastic modulus vs. temperature for both test conditions in air and high vacuum. Figures 51 through 53 show similar plots for yield strength, UTS and %elongation, respectively.

The tensile test results from this study compares very well with those reported by Ward and Balsone (12). For example, we consider the microstructure in this study is of intermediate fine structure. Accordingly, the yield and tensile strengths are intermediate between the values reported for the coarse and fine microstructures as defined in reference (12). Similar to the findings of Ward and Balsone, in

Table 5. Tensile data for Ti-25%Al-10%Nb-3%V-1%Mo alloy (Heat Treatment C)

Spec. No.	Temp.°C (Env.)	Modulus GPa	Y.S. MPa	UTS MPa	Elong. %
S89C34	25(Air)	139	731	876	1.54
S89C35	25(Air)	132	758	903	1.85
S89C43	315(Air)	133	658	995	9.83
S89C44	315(Air)	132	626	907	5.31
S89C46	315(Air)	130	638	913	4.98
S89C49	315(Vac)	120	634	935	8.02
S89C50	315(Vac)	120	654	940	7.13
S89C40	425(Air)	121	576	875	8.29
S89C42	425(Air)	123	607	903	7.72
S89C47	425(Vac)	114	614	1022	18.64
S89C48	425(Vac)	119	636	988	11.37
S89C36	540(Air)	118	570	793	4.37
S89C38	540(Air)	107	581	786	4.27
S89C41	540(Vac)	104	584	952	26.12
S89C45	540(Vac)	112	625	987	26.14
S89C32	650(Air)	105	567	717	2.62
S89C33	650(Air)	92	547	703	4.38
S89C39	650(Air)	110	543	903	3.81
S89C31	650(Vac)	101	684	793	14.07
S89C37	650(Vac)	114	593	848	13.40

general, the tensile properties in ultrahigh vacuum are much better than the corresponding properties in air environment, especially at higher temperatures. For example, the yield strength, ultimate tensile strength, and ductility are all superior under high vacuum environment compared to the air environment (Figures 51 and 53). And, the elastic modulus and the yield strength showed a decreasing trend with increasing temperatures in both air and vacuum environments. The ultimate tensile strength showed an increase with temperature up to about 425°C and a decrease above this temperature in vacuum environment, while in air the UTS at 315°C was higher than at room

temperature and it decreased with temperature above 315°C. The ductility increases significantly (from less than 2% elongation at room temperature to over 25% elongation at 540°C) with temperature up to 540°C in vacuum and decreases above that temperature. A more moderate increase in ductility up to 425°C was observed in air followed by a decrease at higher temperatures. The increased ductility in ultrahigh vacuum might be associated with the increase in the UTS as compared to that in air environment. These trends are similar to the trends observed by Ward and Balsone in this alloy with four different microstructures.

The fractographs from these tensile fracture surfaces are shown in Figures 54 through 61. Let us first consider the fracture mechanisms in vacuum. At 650°C, the macro fractograph (Figure 54a) shows two flat failure region connected by a ledge in the center. Ductile failure of primary α_2 /matrix interface along with ductile failure of surrounding region was observed (Figure 54c). At 540°C (Figure 55), significant primary α_2 particle cracking is obvious and so were regions of dimple fracture. At lower temperatures (Figures 56 and 57), some evidence of primary α_2 particle cracking is also obvious. These fracture mechanisms are similar to those observed by Ward and Balsone (12). They also found a change in the fracture mechanism with increasing temperatures in vacuum. At low temperatures (427°C) there was significant primary α_2 particle cracking, and associated ductility in the surrounding matrix helps to blunt the cracks. While at 650°C fracture is due to a ductile rupture mechanism with void nucleation at the α_2 /matrix interface. In air environment, generally all these mechanisms appear to be shifted towards lower temperatures. At 650°C, the fracture surface was rough and a slight amount of ductility was observed on the fracture surface along with some secondary cracks (Figure 58). We saw no evidence of primary α_2 particles taking part in the fracture process. At 540°C, the macro fractograph showed two regions on the failure surface (Figure 59a) occurred on two different planes and were connected with the ledge in the center. We noted limited ductility (no significant dimples or tearing) in the flat regions while the connecting ledge region showed signs of some ductility in the form of dimples. There is some evidence of tearing at the primary α_2 /matrix interface. At lower temperatures, there is more evidence of primary α_2 particle cracking (Figures 60 and 61). From these it is apparent that between air and vacuum environments, the general fracture mechanisms are somewhat similar, except that the specific mechanisms seem to become operative at slightly higher temperatures in vacuum environment. This

again was evident in Ward and Balson's work where they compare their vacuum results with the air results of Rosenthal (13). In summary, the effect of temperature on ductility (as evidenced by % elongation) has the effect of changing fracture mechanism from one of primary α_2 cracking below the peak ductility temperature (around 400 in air and 500 in vacuum) to one of fracture/tearing at the interface. It is interesting to note that the former mechanism leads to increasing ductility with increasing temperature, while the latter leads to reduction in ductility.

Fatigue Crack Growth Behavior

As stated earlier in this report, the main objective of this investigation is to develop a basic understanding of the roles of different factors on the damage evolution during crack growth in monolithic titanium aluminides. In this regard, fatigue crack growth experiments were conducted to study the effects of temperature, environment, frequency, and R-ratio. The list of all the different tests performed and the parameters controlled are listed in Table 6. In general, most of the testing were conducted in specimens with the loading axis parallel to the final rolling direction. In order to test any possible effects of anisotropy, a few tests were done in the transverse direction. These specimens were identified with a 'V' (for longitudinal orientation) in the specimen code. The following sections present results from these experiments analyzing specific aspects such as the effect of temperature, environment, etc., on the crack growth behavior. The original intent of this program was to conduct a considerable number of tests in ultrahigh vacuum to fully document the effects of environment. High-vacuum experiments were much more time-consuming (because of specimen set-up and long waiting periods for achieving the ultra-high vacuum conditions) and difficult compared to the air tests. In addition, several equipment problems, mainly associated with computer data acquisition affected the experimental results. The source of the problem is the RF-Induction heater introducing a high level of noise in the data acquisition system. Several attempts to correct the problem were not successful. Therefore, the comparison of ultra-high vacuum tests to air tests had to be limited to just the base-line data. The influences of frequency and orientation on the environmental effects were therefore not fully studied.

Table 6. Summary of fatigue crack growth experiments

Spec. No.	Temp.°C (Environ.)	Test Type	Freq. Hz.	R-Ratio	Orie.
S89T17	RT (Air)	Threshold Constant load	1.0	0.1	Trans.
S89T25	425 (Air)	Threshold	1.0	0.1	Trans.
S89T27	425 (Air)	Threshold Constant load	1.0	0.1	Trans.
S89T23	540(Air)	Threshold Constant load	1.0	0.1	Trans.
S89C24	540(Air)	Constant load	1.0	0.1	Trans.
S89T16	650(Air)	Threshold Constant load	1.0	0.1	Trans.
S89T20	650(Vac)	Threshold Constant load	1.0	0.1	Trans.
S89C22	650(Vac)	Constant load	1.0	0.1	Trans.
S89C19	540(Vac)	Threshold Constant Load	1.0	0.1	Trans.
S89C60V	650(Air)	Threshold Constant Load	1.0	0.1	Long.
S89C70V	650(Air)	Threshold Constant Load	1.0	0.1	Long.
S89C64V	650(Air)	Threshold Constant Load	1.0	0.1	Long.
S89C61V	540(Air)	Threshold Constant Load	1.0	0.1	Long.
S89C62V	425(Air)	Threshold Constant Load	1.0	0.1	Long.
S89C63V	650(Vac)	Threshold	1.0	0.1	Long.
S89C26	650(Air)	Frequency $K_{max} = 15 \text{ MPa}\sqrt{\text{m}}$	1.0, 0.1 0.01, 0.001	0.1	Trans.
S89C27	650(Air)	Frequency $K_{max} = 15 \text{ MPa}\sqrt{\text{m}}$	1.0, 0.01 0.01, 0.001	0.1	Trans.
S89C18	650(Air)	Frequency $K_{max} = 15 \text{ MPa}\sqrt{\text{m}}$	1.0, 0.5 0.1, 0.05	0.1	Trans.
S89C29	650(Air)	Frequency $K_{max} = 15 \text{ MPa}\sqrt{\text{m}}$	1.0, 0.1 0.05	0.8	Trans.
S89C65	650(Air)	Frequency $K_{max} = 25 \text{ MPa}\sqrt{\text{m}}$	1, 0.1 0.05	0.1	Trans.
S89C66	650(Air)	Frequency $K_{max} = 25 \text{ MPa}\sqrt{\text{m}}$	1.0, 0.5 0.1, 0.05	0.8	Trans.
S89C21	425(Air)	Frequency $K_{max} = 15 \text{ MPa}\sqrt{\text{m}}$	1.0, 0.5 0.1, 0.05	0.1	Trans.
S89C69	25(Air)	Frequency $K_{max} = 15 \text{ MPa}\sqrt{\text{m}}$	1.0, 0.5 0.1, 0.05	0.1	Trans.
S89C30	25(Air)	Frequency $K_{max} = 15 \text{ MPa}\sqrt{\text{m}}$	0.05	0.1	Trans.

Effect of Temperature and Environment

The overall goal of the program is to understand the effect of several parameters such as temperature, environment, frequency (time), R-ratio, and crack orientation with respect to the rolling direction on the fatigue crack growth behavior of titanium aluminide. In order to understand the effects of these different variables, baseline information on fatigue crack growth was first generated. Tests were conducted in air and in ultrahigh vacuum at room temperature, 425°C, 540°C and 650°C, both under decreasing stress intensity threshold testing conditions and under increasing stress intensity constant load amplitude testing conditions. All tests were carried out in automated servo-hydraulic testing machines under computer control. Fatigue test procedure and the methods of data analyses are described in detail in a previous section of this report.

The fatigue crack growth data are presented in two different types of plots for all the tests that were run at different temperatures. At a given temperature, a plot of da/dN versus ΔK represents the crack growth rate plotted against calculated (uncorrected) ΔK ($K_{max} - K_{min}$). A plot of da/dN versus $\Delta K_{effective}$ ($K_{max} - K_{closure}$) corrected for closure is presented in the same plot. The second one is the plot of $K_{closure}$ versus K_{max} . A series of these plots are shown in Figures 62 and 63 for room temperature, 64 and 65 for 425°C, 66 and 67 for 540°C and 68 and 69 for 650°C tests all run in laboratory air environment. For tests run in ultrahigh vacuum environment at 540°C and 650°C plots of da/dN versus ΔK are presented in Figures 70 and 71, respectively. Since the vacuum tests showed very little closure, $K_{closure}$ and $\Delta K_{effective}$ were not computed for these tests. In all these plots, the data generated from threshold experiments and constant loading experiments are plotted together. In some cases, more than one specimen was involved. In general the test data from different tests at a given temperature were continuous and overlapped very well at intermediate stress intensity ranges.

Figures 72 and 73 show a summary of all the crack growth rate versus ΔK and $\Delta K_{effective}$ plots, respectively for tests run in laboratory air environment. The room temperature test exhibited a slightly higher threshold (about 6 MPa \sqrt{m}) compared to the elevated temperature tests (about 5 MPa \sqrt{m}). At low ΔK (below about 10 MPa \sqrt{m}), the effect of increased temperature appears to result in increased crack growth rate. At ΔK higher than about 15 MPa \sqrt{m} the room temperature test

showed crack growth rates higher than the elevated temperature tests. However, with in the elevated temperature tests (i.e., between 425°C and 650°C) the ranking remained the same i.e., the higher the temperature the faster the crack growth rate.

Figures 74 and 75 compare the crack growth rate data from tests run at 540 and 650°C both in air and in ultrahigh vacuum. Clearly the ultrahigh vacuum tests show crack growth rates that are about an order of magnitude slower than the corresponding tests run in laboratory air environment. The threshold stress intensity factor is mildly affected by the environment at 650°C while at 540°C the vacuum test showed a much higher threshold compared to the air tested sample. These observations lead us to believe that the crack growth is adversely affected by the oxidizing environment.

Figures 76 and 77 show a comparison of $K_{closure}$ for the tests run in laboratory air environment under both decreasing stress intensity threshold testing conditions and constant amplitude increasing stress intensity conditions. In general, at all temperatures, the $K_{closure}$ increased with increasing K_{max} . Also, the increase in $K_{closure}$ is greater for lower temperatures. For example, in the temperature range studied here, Figures 76 and 77 show that the room temperature $K_{closure}$ values are usually the highest and the corresponding values for the 650°C are the lowest.

The fatigue crack growth tests conducted in ultra-high vacuum showed very little or no closure effects. Therefore, no effort was made to compute the $K_{closure}$ values. Figure 78 shows a typical load versus deflection data for the fatigue crack growth test run in ultra-high vacuum under constant load amplitude test conditions at 650°C. Although there is considerable scatter in the data shown in this figure, the plot supports the conclusion that there is little closure. In comparison, the load-deflection plot shown earlier in Figure 17 for a test run in air environment shows a definite closure effect.

In general, the fracture surfaces of specimens tested in laboratory air environment showed different degrees of oxidation. For example, the specimen tested at room temperature (S89C17) showed no oxidation on the surface. At 425°C in air, (S89C25), both the precracked region and the fatigue cracked region showed some sign of oxidation. A thin yellowish brown oxide scale was found on the fracture surface. At 540°C in air, (S89C23), the precrack region showed some strong signs of oxidation, while the fatigue crack growth region showed a thin

yellowish brown oxide layer. At 650°C in air, (S89C26), the fracture surface showed very dark oxide layer. At 650°C in vacuum, the fracture surface was bright and no oxidation was evident. We saw similar surface oxidation in other specimens tested at high temperatures (between 425°C and 650°C) in air.

Figures 79 - 83 show typical fractographs of specimens tested at different temperatures. These fractographs were taken from regions of the fracture surface in the mid-range of the stress intensity range (about 10-12 MPa \sqrt{m}). In general, the room temperature specimen showed relatively crystallographic fracture with some evidence of cleavage fracture. We saw similar fracture features for tests run in ultrahigh vacuum conditions. In contrast, the specimen tested at 650°C showed evidence of fatigue damage as evidenced by apparent fatigue striations in figure 82. This is the same specimen that showed significant oxidation of the fracture surface. At intermediate temperatures (540°C and 425°C) the fracture surface showed mixed (crystallographic and fatigue) fracture mode.

Effect of Orientation

Fatigue crack growth experiments (both decreasing-stress-intensity threshold tests and increasing-stress-intensity constant load tests) were conducted in air environment at elevated temperatures (425°C, 540°C, and 650°C) on compact tension specimens oriented so that the loading axis is perpendicular to the final rolling direction (longitudinal orientation). This was done to help us understand any possible effects of orientation on the crack growth behavior. Several experiments under ultrahigh vacuum conditions were also planned. But, because of previously stated difficulties with the data acquisition system, this aspect of the problem was not studied in detail.

Results of individual tests are presented in the form of plots of da/dN versus ΔK and $\Delta K_{\text{effective}}$ in Figures 84 through 86 are results from tests conducted at 650°C, and Figures 87 and 88 show similar plots for 540°C and 425°C. Compared to the base-line data from specimens with transverse (i.e., the loading axis parallel to the final rolling direction) orientation, these data show a large amount of scatter. A summary of results for all the temperatures is shown in Figure 89. Again, as shown in the base-line data, the crack growth rates were faster at higher temperature. The threshold stress intensities for all the test temperatures were similar to the values found for the transverse orientation. However, in the transverse orientation, the specimens

appear to have stable crack growth even at relatively high stress intensities ($30 \text{ MPa}\sqrt{\text{m}}$ or higher), while in the longitudinal orientation, the none of the specimens appear to have gone beyond about $15 \text{ MPa}\sqrt{\text{m}}$. It is unclear from this study as to whether this means an inherently lower toughness (K_C or K_{IC}) for this orientation, while the fatigue crack growth rates are relatively unaffected. Comparison of data at the same temperature between two orientations show no significant differences in crack growth rates at all the three temperatures. In fact, attempts to plot data from the two orientations in one plot resulted in significant overlap of the data that it became difficult to distinguish between them. Therefore, such combined plots are not presented here.

Closure analyses were done with the fatigue crack growth data and the results are presented as plots of K_{closure} versus K_{max} in Figures 90 through 94. Again, there appears to be very little closure in these tests.

Effect of Frequency and R-Ratio

Both environment and creep are known to play important roles in the fatigue damage of these alloys (14). For example, earlier in this investigation, the effect of environment was demonstrated so that the fatigue crack growth rates at elevated temperatures were more than an order of magnitude faster in air than in ultrahigh vacuum. This would imply that elevated temperature crack growth rates would also be significantly affected by changes in fatigue frequency or a hold period in the cycles. In this section, experimental results from the study on the effects of frequency and R-ratio on fatigue crack growth rates are presented.

Experiments were originally designed to study the effects of frequency over several orders of magnitude ranging from about 0.001 Hz to about 10 Hz. We soon realized that there were severe constraints on the computer data acquisition system, which affected the quality of the data collected over the five orders of magnitude of frequencies. At very high frequencies the data collection rate of the interface board was not adequate to collect sufficient data per cycle to do any meaningful analyses. We should remember that the tests were conducted using a PC-based computer control-data acquisition system. At very low frequencies, data acquisition rates could not be matched with the frequency of testing. This resulted in the computer "hanging-up" in the middle of a data acquisition stage. This in turn gave erroneous crack

growth rates. For example, the first two specimens tested in this category (specimens S89C26 and S89C27) were tested at several frequencies ranging from 1 Hz down to 0.001 Hz. Results from this first tests showed no definite trend in the crack growth rates, and this was primarily attributed to difficulties in experimental data acquisition. Subsequent studies were therefore restricted to fatigue frequencies between 1 Hz and 0.01 Hz. Usually experiments were conducted at 1, 0.5, 0.1, and 0.05 Hz. In this small range of frequencies, there were no experimental problems, and even with this limited data, the crack growth rates showed very definite trends. Results of these experiments are presented and discussed in this section.

In general, specimens tested for frequency effects were prepared by precracking at the test temperature, using procedures that were described earlier. After the precracking, the crack growth rate at the first frequency (usually the highest frequency of 1 Hz) was determined by imposing a constant K_{max} , ΔK , and R-ratio on the specimen and monitoring the crack length. After a growth of about 2000 to 2500 microns (i.e., after the crack growth rate stabilizes for a given frequency), the test was put on hold. The frequency of testing was altered to the next lower frequency, and the crack growth was monitored. When testing at all the four frequencies (i.e., 1, 0.5, 0.1, and 0.05 Hz) were completed, some repeat measurements were made at chosen frequencies. This procedure was repeated until the total crack length was about 25 mm. This meant that in one sample, particularly when the crack growth rates are slow, several measurements of crack growth rate at a given frequency could be made. These repeat measurements were not feasible in those conditions which showed faster crack growth rates. In general, in many of these repeat measurements, the crack growth rates were slower at longer crack lengths, but at the same frequency. For example, in Figure 99, segments A and D showed significant differences in crack growth rates, when tested at the same frequency of 0.05 Hz, but at two different crack lengths. When this apparent discrepancy was first observed, additional attention was paid to the local cracking behavior at the crack front and the possible effects of closure on the crack growth process. Consequently, in some of the experiments, the crack growth was visually monitored, and also in these experiments more detailed crack length versus cycles plots were made. We observed that during the crack growth process, there were periods in which significant crack branching occurred, which tended to affect both the compliance calculated crack length and crack growth rate. Some typical examples of crack branching are obvious in micrographs shown in Figures 95

through 97. Also, in order to demonstrate the possible effects that the crack branching could have on the crack growth rates, some typical crack length versus cycles plots are shown in Figures 98 through 102. As shown in these figures, the crack growth rate was significantly affected in the periods when crack branching was observed. Therefore, for the purposes of determining crack growth rates, the regions of crack branching in the crack length versus cycles plots were not considered, i.e., the crack was allowed to grow well until the effects of crack branching were overcome. This method of analyses could be expected to yield the true crack growth behavior of the material, without the influence of crack branching. These observations along with the possible effects of closure will be discussed later in more detail.

Through these frequency experiments several different factors were simultaneously investigated. Experiments were conducted at three temperatures (room temperature, 425°C and 650°C), at two different K_{max} (15 and 25 MPa√m), and two R-ratios (0.1 and 0.8). Figures 103 through 108 present the plots of crack growth rate versus frequency for individual experimental conditions. Figure 109 shows a summary of these plots. These data can be analyzed in a number of ways to elucidate the effects of different parameters on crack growth rates. In general, these Figures show that at elevated temperatures, the fatigue crack growth rates are faster at lower frequencies. This could possibly mean that either environment, creep, or both affect the crack growth behavior. One way these effects could have been separated is to conduct similar experiments under the ultrahigh vacuum environment to eliminate the adverse effects of air environment. Unfortunately, in the last 6 months of this contract, several instrumentation problems in the ultrahigh vacuum MTS system prevented us from running these critical experiments. The effect of frequency on crack growth rates observed in this investigation is in general agreement with the previous research work on Ti-24Al-11Nb alloy by Balsone, et al (14). The effect of frequency on the room temperature fatigue crack growth rate is mixed. There are noticeable differences in the way frequency affected the crack growth rates because of different K_{max} and R-ratios. For example, at a constant K_{max} of 15 MPa√m and R-ratio of 0.1, the effect of temperature is shown in Figure 110. Crack growth rates at room temperature falls between the rates at 650°C and 425°C. This observation is very consistent with the earlier observation on the crack growth rate over the entire ΔK range. Figure 72 shows that in the 15 MPa√m stress intensity range the crack growth rates fall between the rate at 425°C and 650°C. Also, the room temperature data show no specific trend with respect to frequency, while both the elevated temperature tests show similar orders of magnitude changes in the

crack growth rates. This could be due to lack of time-dependent (creep and/or environment assisted damage) processes assisting the crack growth process at room temperature. Figures 111 and 112 show the role of R-ratio on the effect of frequency on crack growth rates at 650°C for K_{max} values of 15 MPa√m and 25 MPa√m respectively. At K_{max} of 15 MPa√m the effect of increasing the R-ratio from 0.1 to 0.8 appear to show a more significant effect on the crack growth rate. A similar R-ratio effect could not be determined at K_{max} of 25 MPa√m since the crack growth rates were very high, which resulted in fewer data points to compare. For example, as shown in Figure 111, at K_{max} values of 15 MPa√m and R-ratio of 0.8, an order of magnitude change in frequency, say, from 0.1 to 1 Hz, appears to affect the crack growth rate by a factor of 3, while a similar change in frequency for K_{max} values of 15 MPa√m and R-ratio of 0.1 does not result in noticeable change in crack growth rates. Figures 113 and 114 show the effect of K_{max} at constant R-ratio values. Again at the lower K_{max} the crack growth rate seems to be affected by the frequency more significantly than at the higher K_{max} . In general, it appears that conditions that result in slow crack growth rates (low K_{max} and high R-ratio) result in relatively significant frequency effects on crack growth rate. This could be because, slower the inherent crack growth mechanism, the more the material is prone to time dependent effects (such as environmental attack and creep). Further research using frequencies over several orders of magnitude and several different R-ratios need to be conducted in order to fully understand this.

The observation that at a given K_{max} , R-ratio, and frequency, the crack growth rates were slower with increasing crack length, was further examined by looking at two possible factors, viz., crack branching and crack-length dependent closure. Both these factors could lead to a decrease in the actual stress intensity factors at the crack tip compared to the calculated values and hence slower crack growth rates.. It is very difficult to determine numerical correction factors to the stress intensity because of the effects of crack branching. However, as shown in the crack length versus cycles plots (Figures 98 - 102), it is obvious that the event of crack branching does lead to a considerable slowing down of the crack growth rate. Figures 115 through 118 show plots of $K_{closure}$ versus crack length for few of the specimens tested for frequency effects. Although there is considerable scatter in the data presented in these Figures, a trend of increasing closure with increasing crack length appears to exist. We do not know the reasons for such a trend, and a more detailed study may be required to understand this behavior.

CONCLUSIONS

A study of optimizing heat treatment for a balanced combination of mechanical properties of Ti-25%Al-10%Nb-3%V-1%Mo was conducted. This optimized heat treatment was used for further study of the effects of several factors such as temperature, environment, frequency, R-ratio, and orientation on the fatigue crack growth behavior. The following are the main findings of these studies:

1. The β -transus temperature of this alloy slightly above 1125°C, as compared to the 1099°C, reported by Ward and Balsone (13).
2. The optimum heat treatment consisted of solution treatment at 1115°C ($\alpha+\beta$ field) in vacuum for 1 hour followed by cooling to room temperature in argon, followed by aging at 760°C in vacuum for 8 hours followed by cooling to room temperature in argon. This treatment resulted in fine transformed microstructure with volume fraction of 25% of primary α_2 -phase. This heat treatment resulted in superior fatigue crack growth resistance while still maintaining good tensile and creep properties.
3. Both in air and in ultrahigh vacuum environments fatigue crack growth rates were generally higher at temperatures above 425°C. At room temperature, the crack growth rate was higher than the elevated temperature above a ΔK value of about 15 MPa \sqrt{m} , while at lower ΔK values it was slower. Therefore, the crack growth rates appear to be a minimum at intermediate temperatures between room temperature and 425°C, especially at higher stress intensity ranges.
4. At elevated temperatures, crack growth rates in air environment are about an order of magnitude faster than in ultrahigh vacuum environment.
5. Fatigue crack growth rates were not affected by the orientation of the sample with reference to the final rolling direction. The crack growth rates were not very different when tested in two orientations, longitudinal and transverse to the rolling direction.
6. Orientation however seems to have an effect on the toughness of the material. Although fracture toughness tests were not conducted in this program, it appears from the stress intensities used in the crack growth tests, that the alloy is almost twice as tough in the final rolling direction.

(transverse orientation with the crack plane perpendicular to the final rolling direction) compared to the direction normal to the rolling direction (longitudinal orientation with the crack plane parallel to the final rolling direction). This implies that there is possible anisotropy in the material because of texture.

7. Crack closure effects were found to be a minimum at lower stress intensity ranges. $K_{closure}$ is higher at higher K_{max} . This effect appears to be more due to crack length associated closure (from crack branching, tortuous crack paths, etc.) than because of increase in ΔK . This conclusion was reached based on observed differences in both crack growth rates and in $K_{closure}$ values made at constant ΔK (or K_{max}) at different crack lengths.

8. The low temperature fracture mechanisms are crystallographic cleavage fracture. At high temperature, in air, the fracture surface showed evidence of conventional fatigue striations and also evidence of extensive oxidation. In vacuum, the fracture mode was a mixed mode fracture of crystallographic cleavage with some evidence of tearing of α_2 -plates. This could be due to thin films of β -phase in between α_2 -plates.

9. Fatigue frequency plays an important role in the crack growth rates at elevated temperatures. In general, slower crack growth is obvious at higher frequencies. The frequency effect seem to be more pronounced when the conditions are generally favorable for slow crack growth, such as low K_{max} and high R-ratio. This could mean that environment plays a significant role in the way frequency affects crack growth rate.

10. There seems to be a crack growth rate dependence on the crack length at a constant K_{max} , R-ratio and frequency. This dependence could be due to either crack branching, crack length dependent closure, or both.

REFERENCES

1. H.A. Lipsitt, "Titanium Aluminides - An Overview," Materials Research Society Symposium Proceedings, Vol.39, 1985.
2. "Research to Conduct an Exploratory Experimental and Analytical Investigation of Alloys," Technical Report No. AFML-TR-78-18. Wright - Patterson Air Force Base, March, 1978.
3. H.A. Lipsitt, D. Shechtman, and R.E. Shafrick, "The Deformation and Fracture of Ti₃Al at Elevated Temperatures," Met. TransA, Vol.11A, August 1980, p. 1369.
4. I.A. Zelenkov and E.N. Osokin, "Oxidation Resistance of the Compound Ti₃Al and its Alloys at Temperatures of 700 and 800°C," Soviet Powder Metallurgy, Metals and Ceramics, October 14(10), 1975, p 839.
5. M.G. Mendiratta, and H.A. Lipsitt, "Steady-state Creep Behavior of Ti₃Al - Base Intermetallics," Journal of Materials Science, 1980, p. 2985.
6. S.M.L. Sastry, and H.A. Lipsitt, "Ordering Transformations and Mechanical Properties of Ti₃Al-Nb Alloys," Met. TransA, Vol.8A, 1977, p.1543.
7. S.V. Ram, "Mechanical Behavior of Titanium Aluminide Under Engine Operating Conditions" - SBIR Phase II - Interim Report for period July 1, 1988 - December 31, 1988 - U.S. Air Force Contract No. F33615-88-C-5408
8. S.V. Ram, "Mechanical Behavior of Titanium Aluminide Under Engine Operating Conditions" - SBIR Phase II-Interim Report for period January 1, 1989 - June 30, 1989 - U.S. Air Force Contract No. F33615-88-C-5408
9. N. Jayaraman, "Mechanical Behavior of Titanium Aluminide Under Engine Operating Conditions" - SBIR Phase II - Interim Report for period July 1, 1989 - December 31, 1989 - U.S. Air Force Contract No. F33615-88-C-5408
10. J.M. Larsen, "An Automated Photmicroscopic System for Monitoring the Growth of Small Fatigue Cracks" - ASTM-STP, Seventeenth National Symposium on Fracture Mechanics, August 1984.
11. S.J. Balsone, "The Effect of Elevated Temperature Exposure on the Tensile and Creep Properties of Ti-24Al-11Nb," TMS Proceedings, 1989.
12. C.H. Ward, and S.J. Balsone, "The Effect of Salient Microstructural Constituents on the Tensile and Creep Deformation of Ti-25Al-10Nb-3V-1Mo."
13. D.G. Rosenthal, Unpublished Research, Textron/Lycoming, 1987.
14. S.J. Balsone, D.C. Maxwell, M. Khobaib and T. Nicholas, "Frequency, Temperature and Environmental Effects on Fatigue Crack Growth of Ti₃Al" - to appear in Fatigue 90.

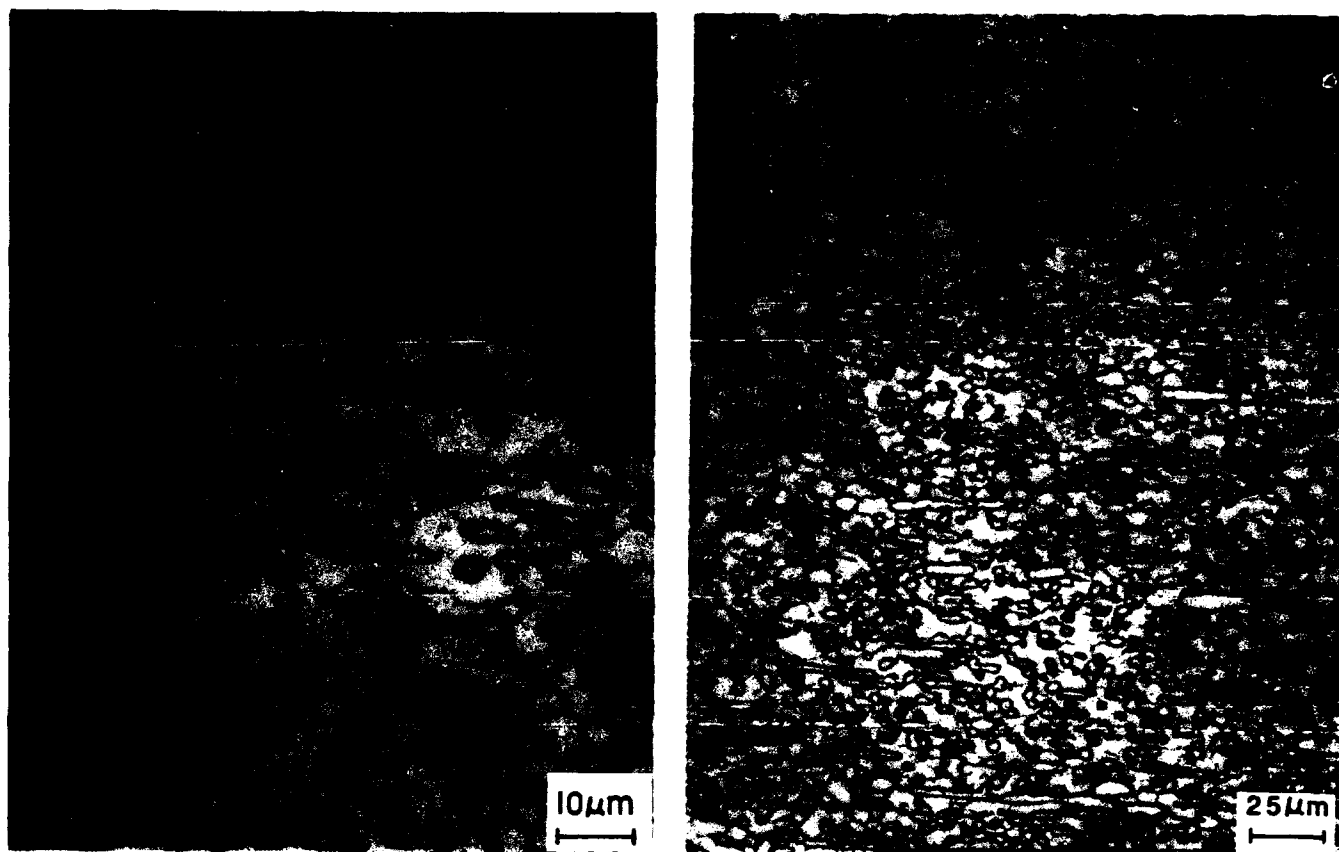


Figure 1. The as rolled microstructure.



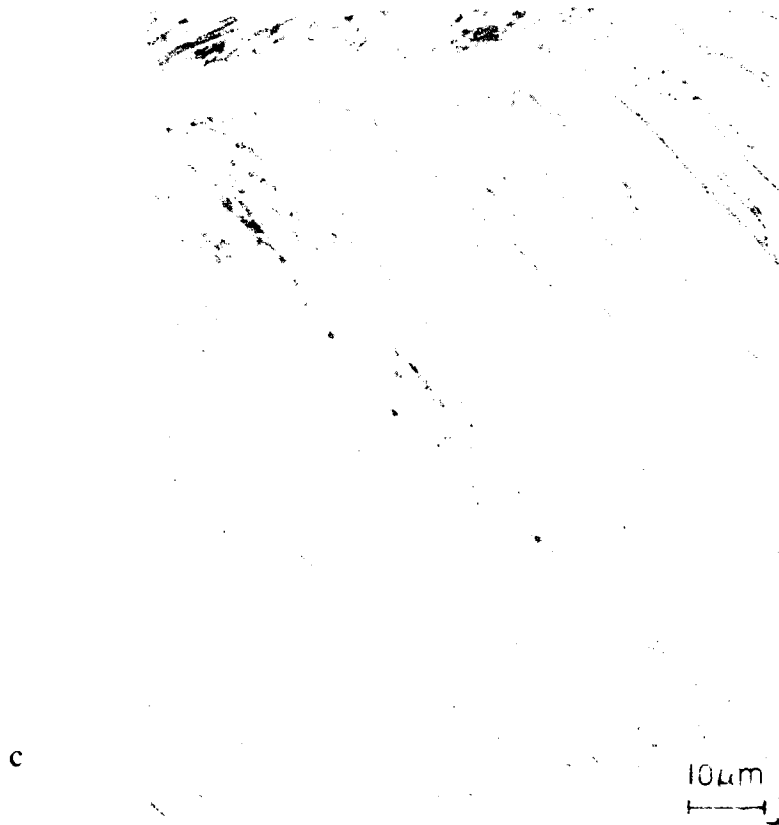
Figure 2. Heat treatment #1 - Solution at 1125°C(1 hr); Slow cool to 816°C; Furnace cool to RT.



a



b



c

Figure 3. Heat treatment #2 - Solution at 1175°C(1 hr); Slow cool to 816°C; Furnace cool to RT.

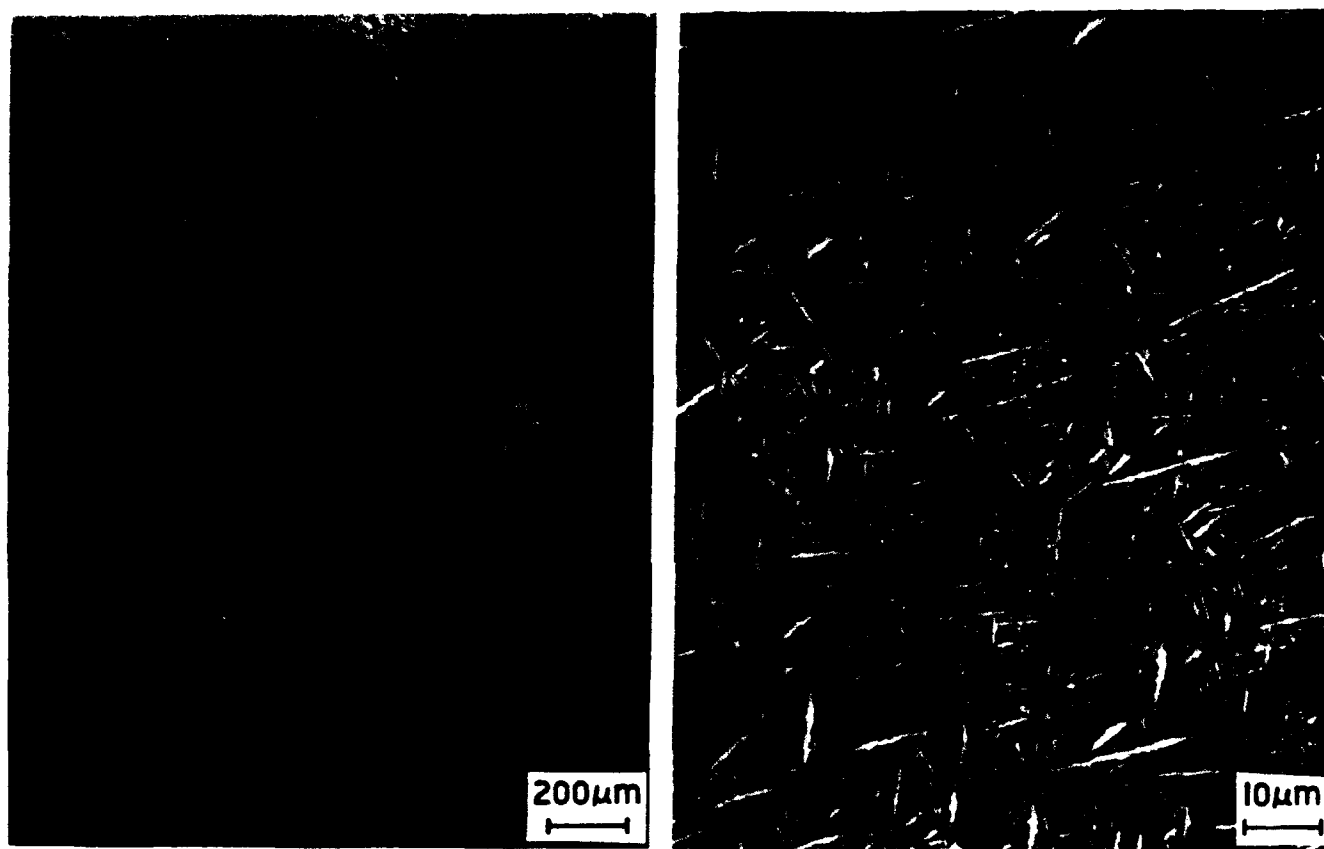


Figure 4. Heat treatment #3 - Solution at 1175°C(1 hr); Quench to 760°C and age for 8 hours; Furnace cool to RT.

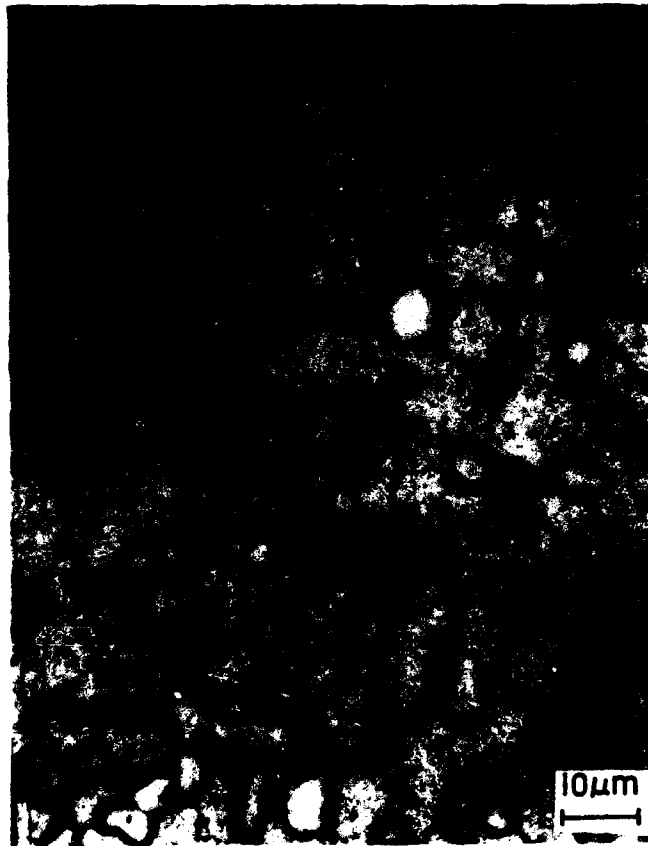


Figure 5. Heat treatment #4 - Solution at 1100°C(1 hr); Air cool to RT; Age at 760°C for 8 hours and cool to RT.

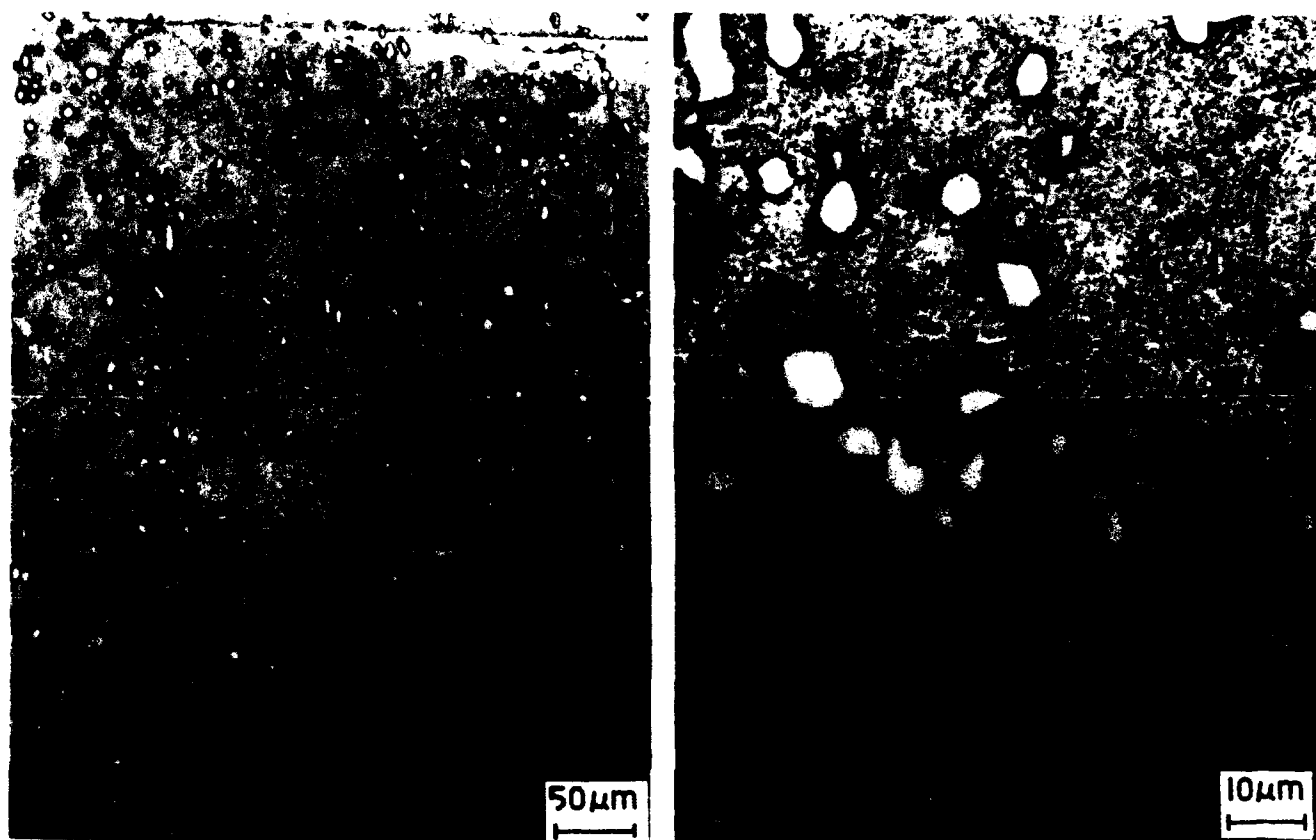


Figure 6. Heat treatment #5 - Solution at 1125°C(1 hr); Cool in argon to RT; Age at 760°C for 8 hours and cool to RT.

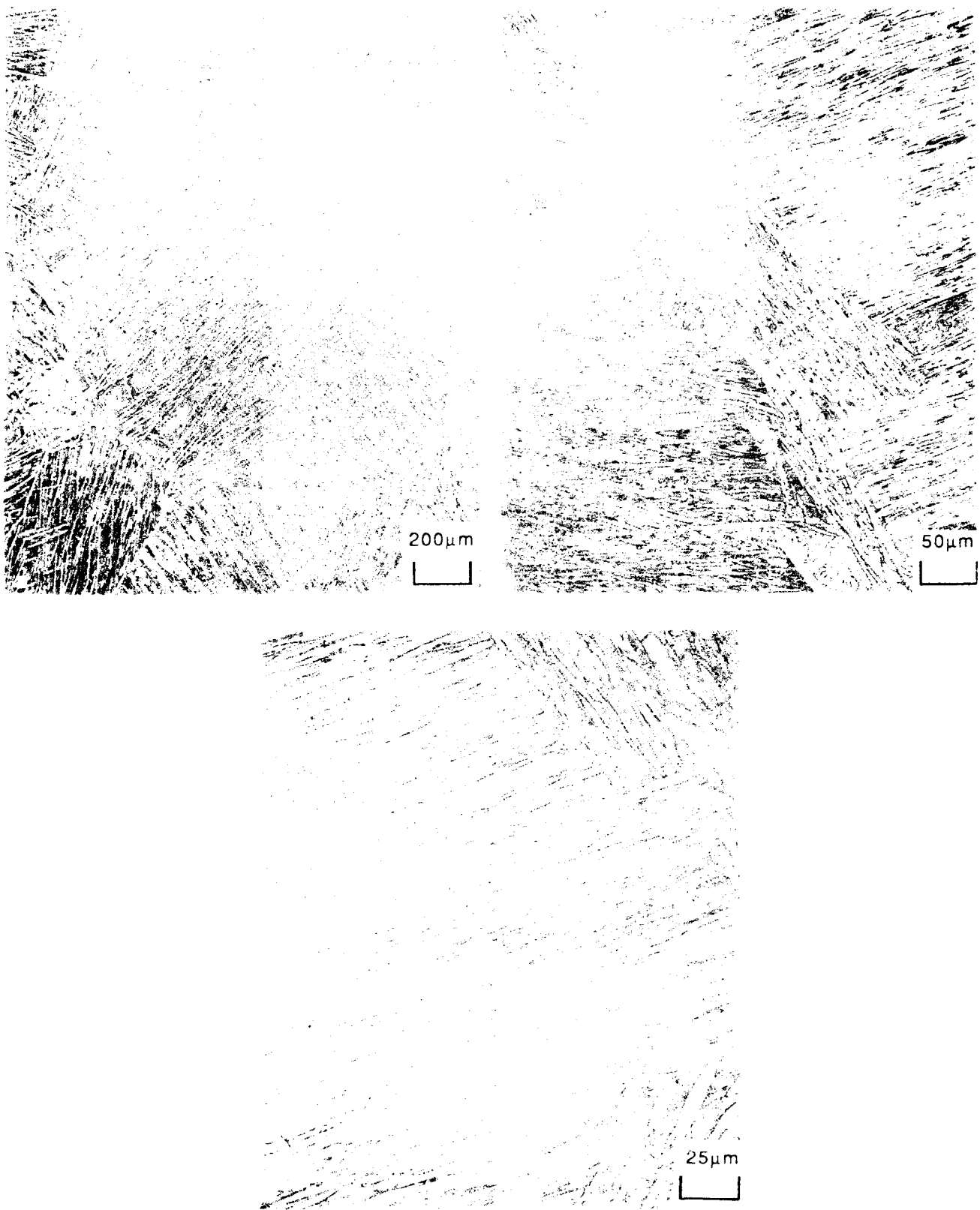


Figure 7. Heat treatment A - Solution at 1175°C(1 hr); Slow cool to 816°C; Furnace cool to RT.

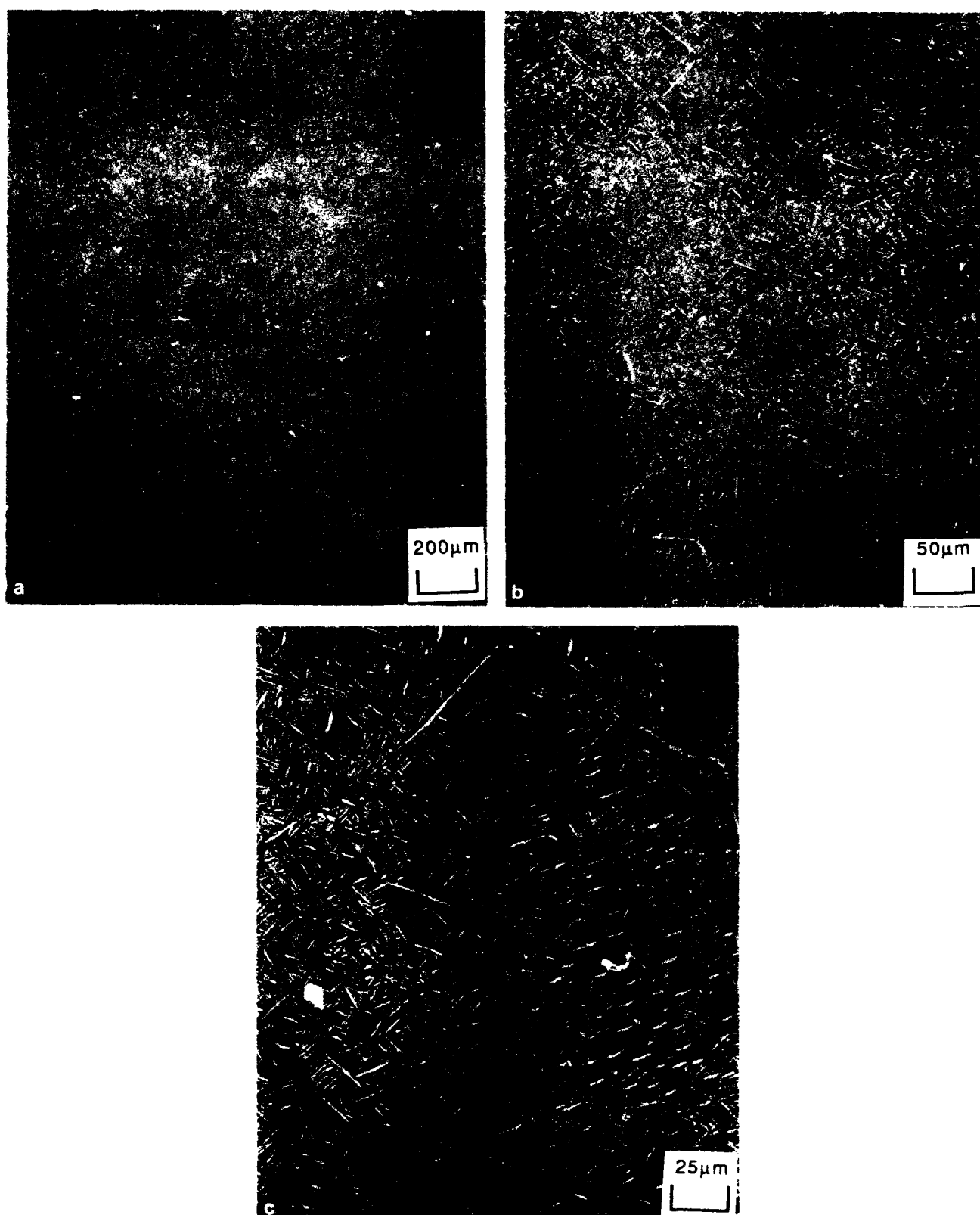


Figure 8. Heat treatment B - Solution at 1175°C(1 hr); Cool in argon to RT; age at 760°C for 8 hours; Cool in argon to RT.



Figure 9. Heat treatment C - Solution at 1115°C(1 hr); Cool in argon to RT; age at 760°C for 8 hours; Cool in argon to RT.

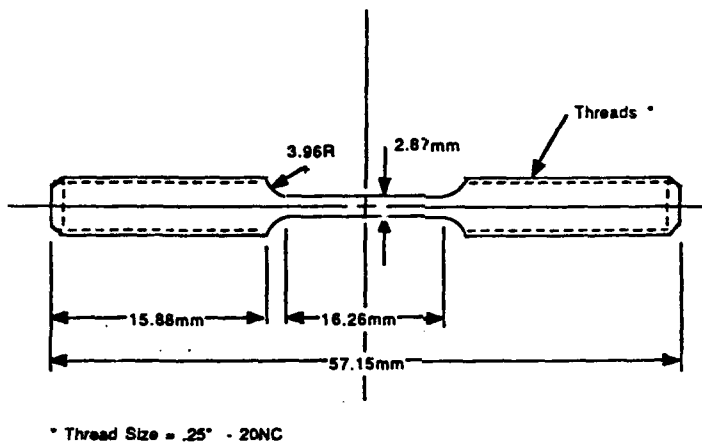


Figure 10. Tensile specimen

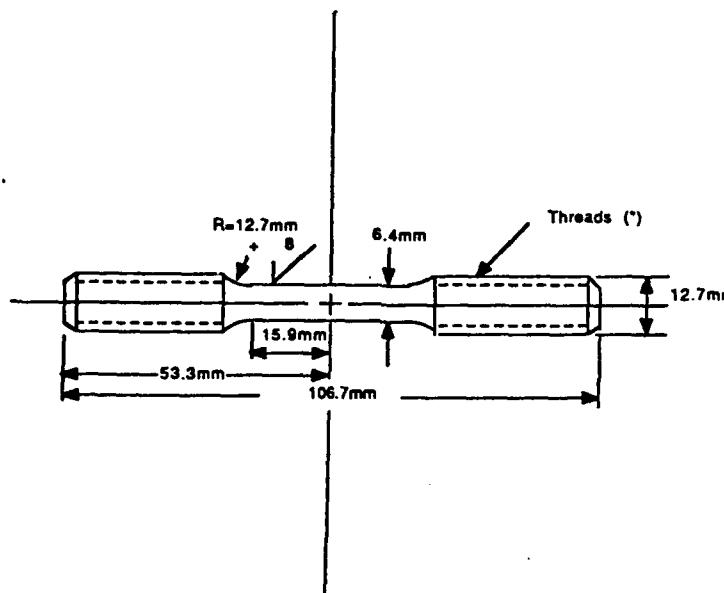


Figure 11. Tensile creep specimen

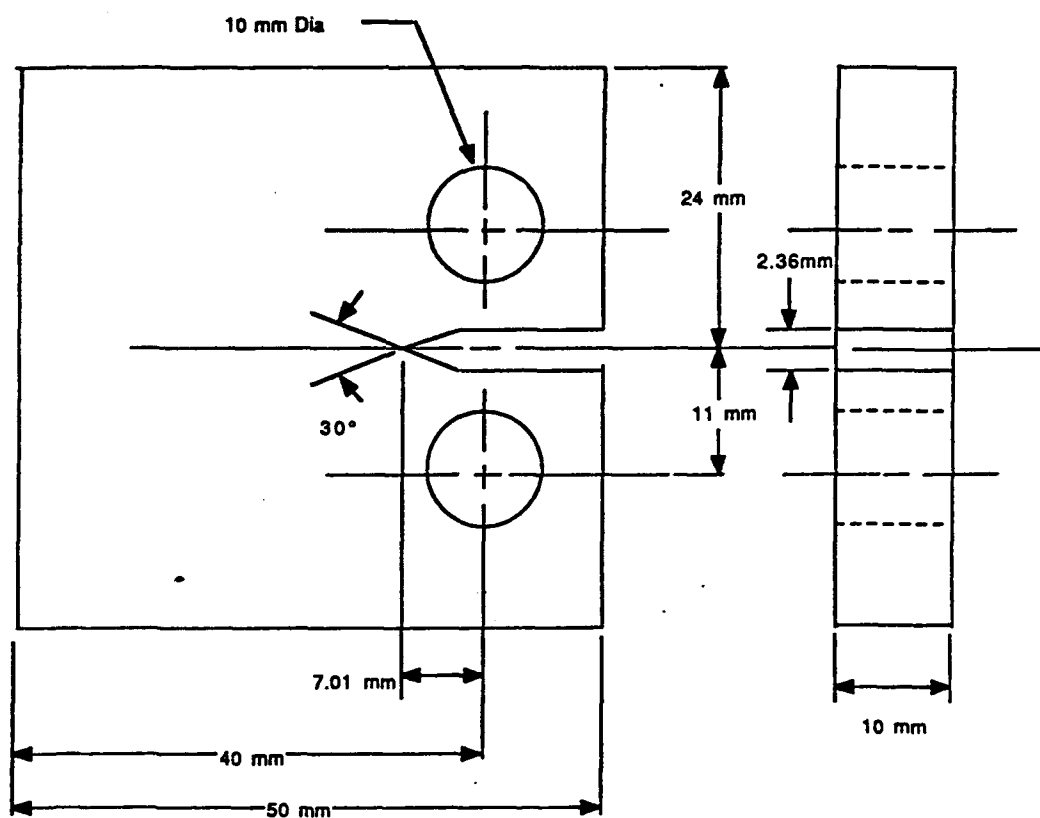


Figure 12. Metric compact tension specimen

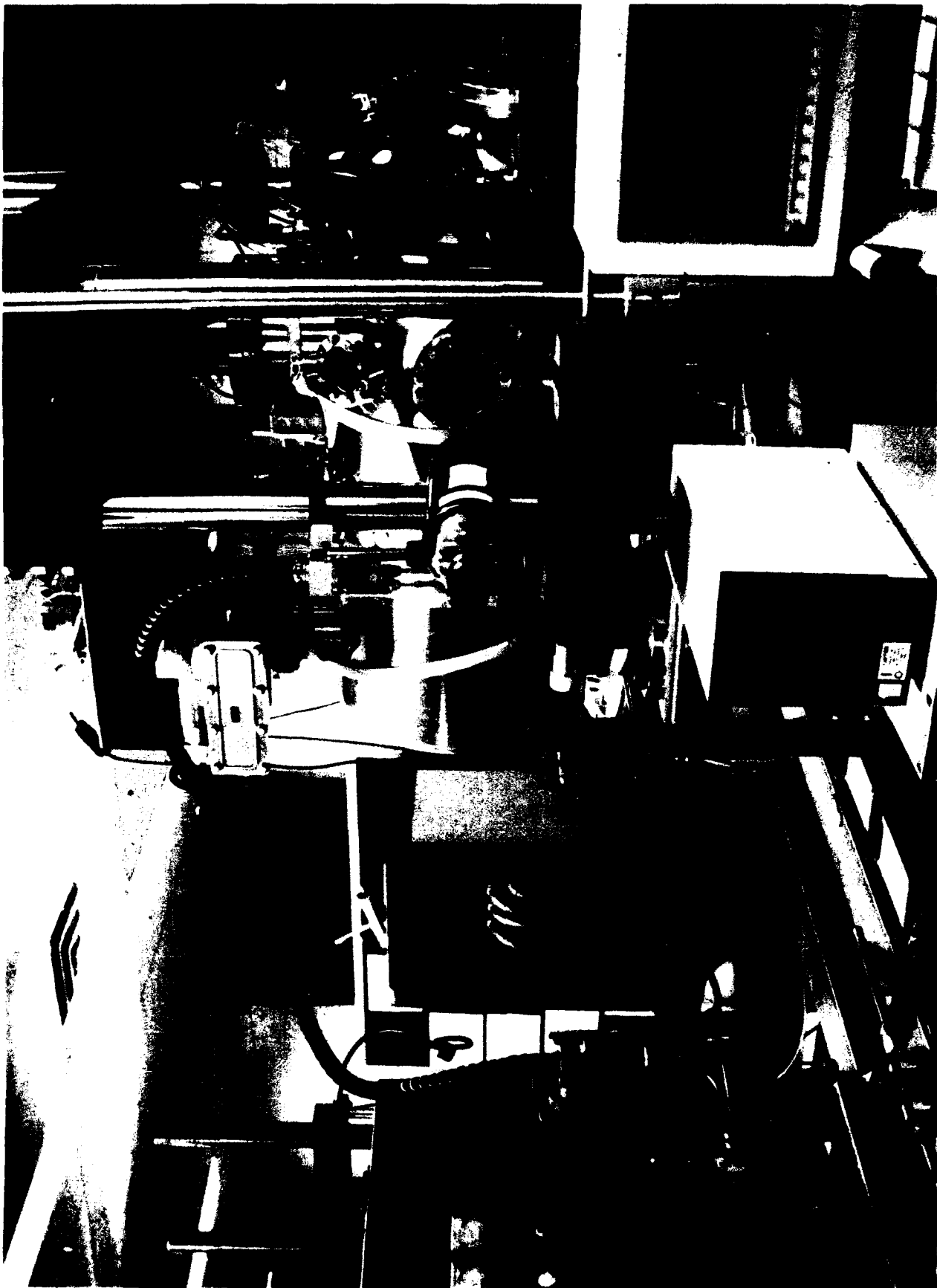


Figure 13. Ultra-high vacuum mechanical test facility.

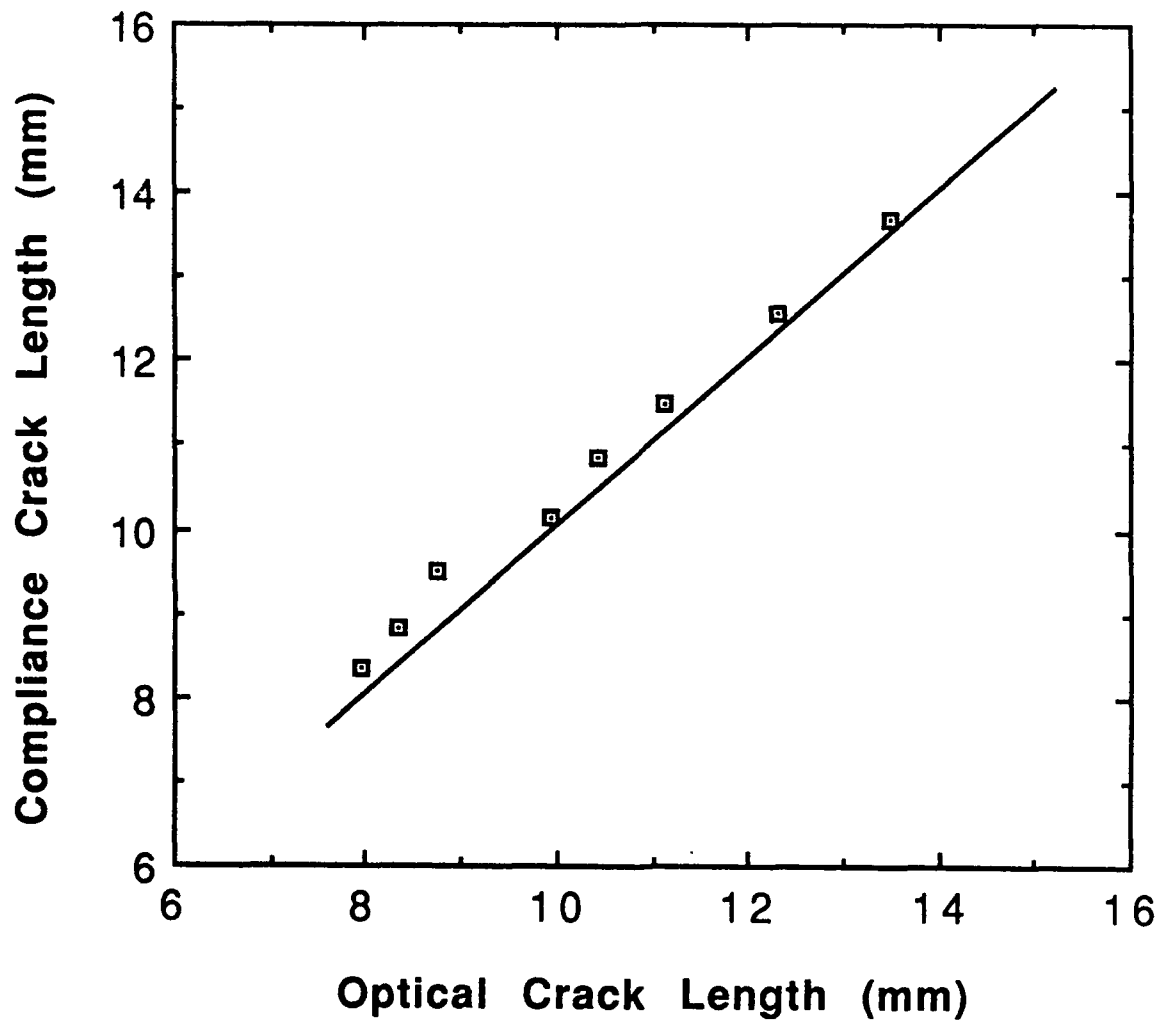


Figure 14. Compliance-measured crack length versus Optically-measured crack length.

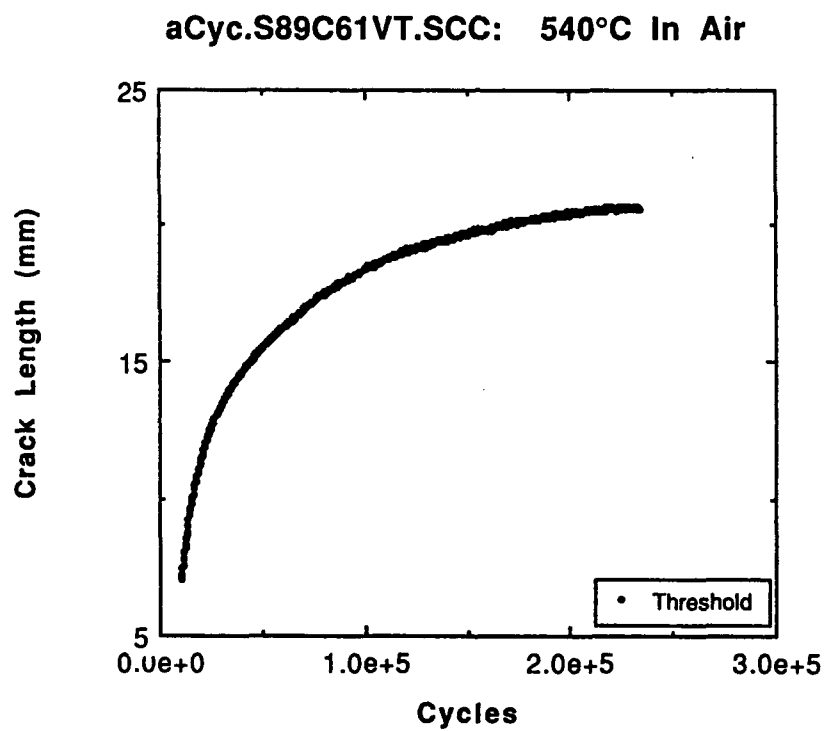


Figure 15. Typical example of a plot of crack length versus cycles for a decreasing-stress-intensity-threshold test.

aCyc.S89C61VC.SCC: 540°C In Air

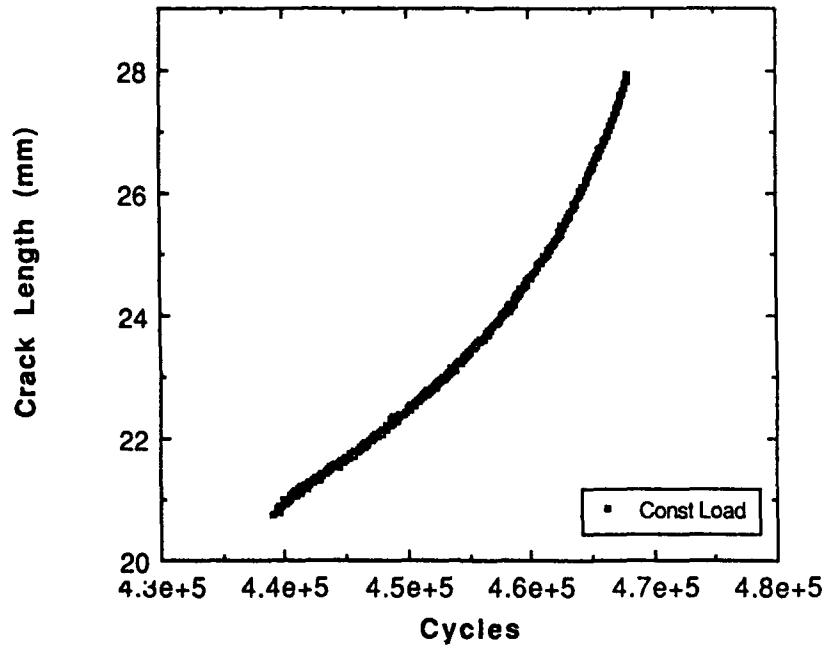
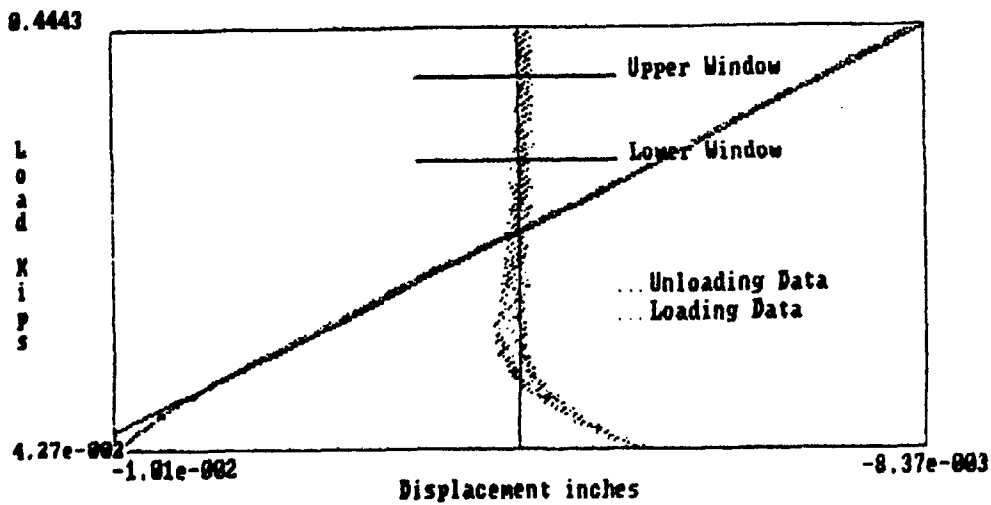


Figure 16. Typical example of a plot of crack length versus cycles for a constant-load-increasing-stress-intensity test.



 S89C16C.CMF 57

Figure 17. Typical load-displacement plot for a specimen exhibiting closure.

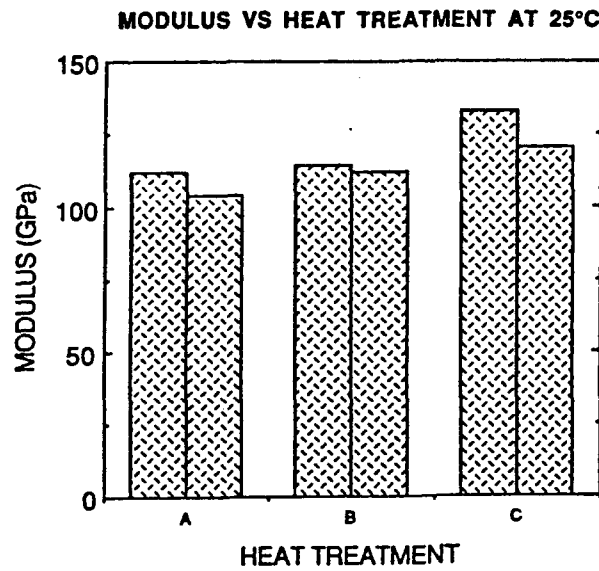


Figure 18. Comparison of the elastic modulus at 25°C for the three heat treatments

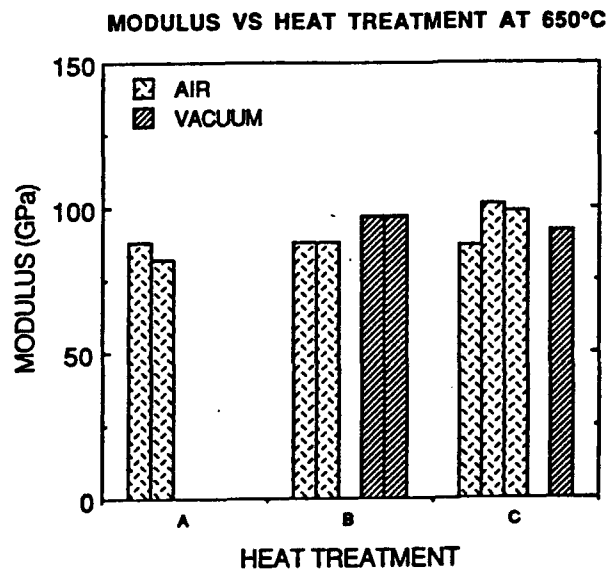


Figure 19. Comparison of the elastic modulus at 650°C for the three heat treatments

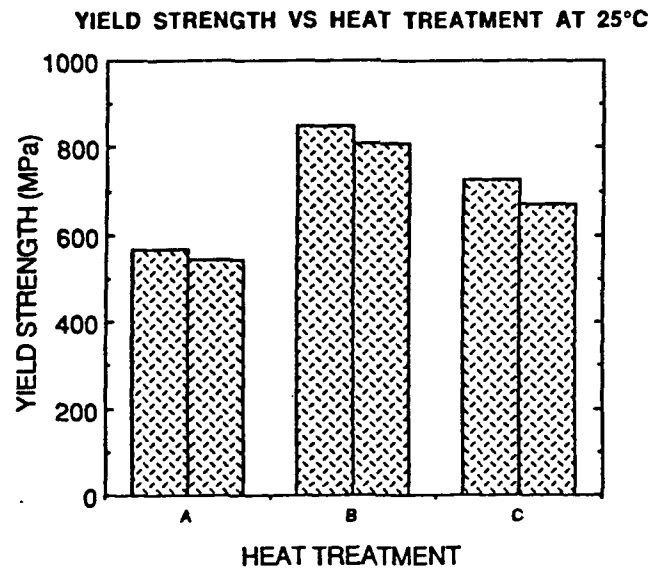


Figure 20. Comparison of the yield strength at 25°C for the three heat treatments

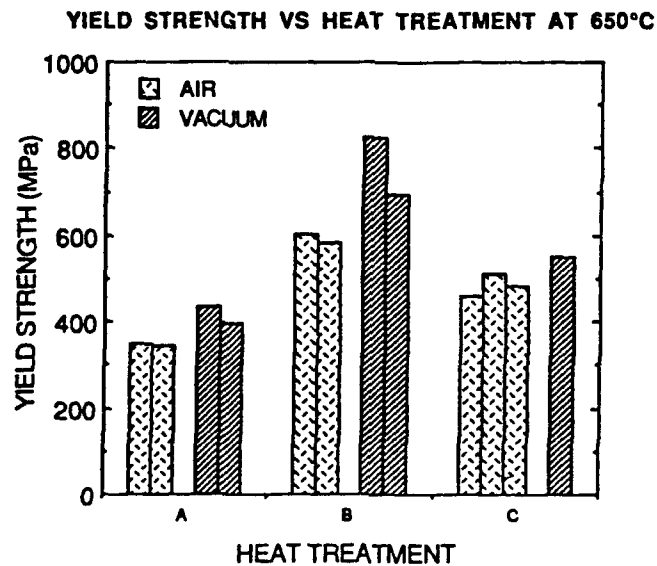


Figure 21. Comparison of the yield strength at 650°C for the three heat treatments

ULTIMATE TENSILE STRENGTH VS HEAT TREATMENT AT 25°C

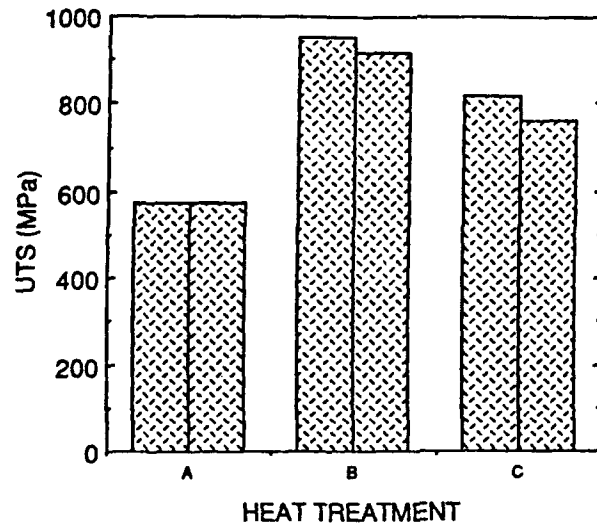


Figure 22. Comparison of the UTS at 25°C for the three heat treatments

ULTIMATE TENSILE STRENGTH VS HEAT TREATMENT AT 650°C

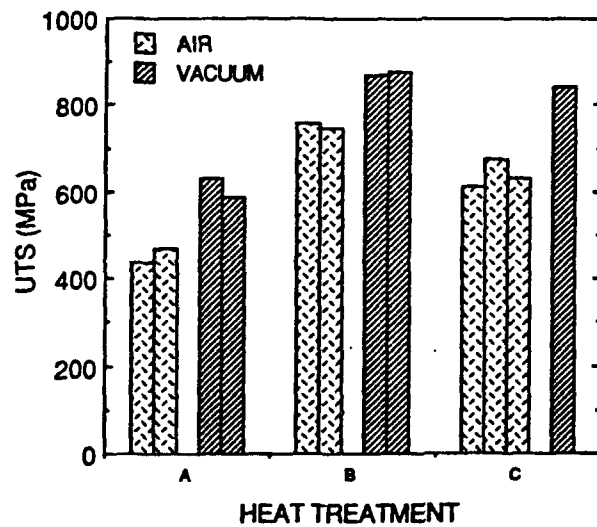


Figure 23. Comparison of the UTS at 650°C for the three heat treatments

DUCTILITY (% ELONGATION) VS HEAT TREATMENT AT 25°C

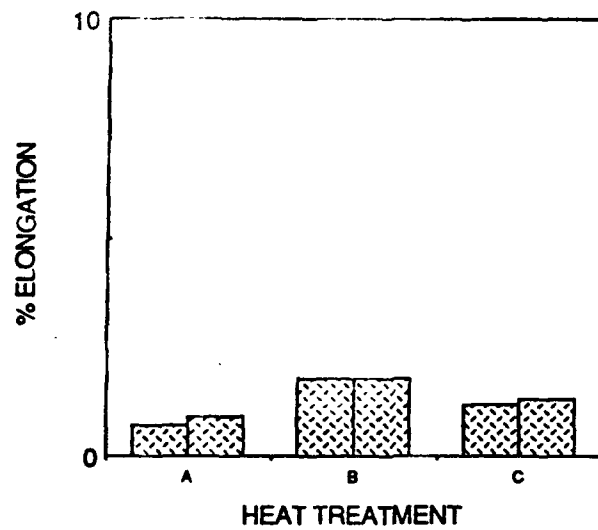


Figure 24. Comparison of the % elongation at 25°C for the three heat treatments

DUCTILITY (% ELONGATION) VS HEAT TREATMENT AT 650°C

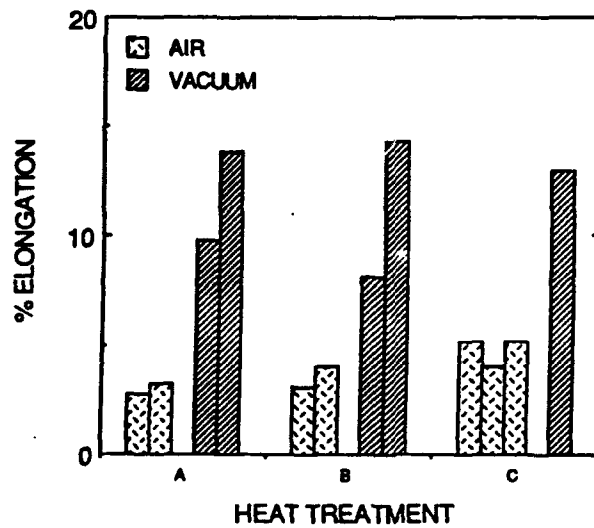


Figure 25. Comparison of the %elongation at 650°C for the three heat treatments.

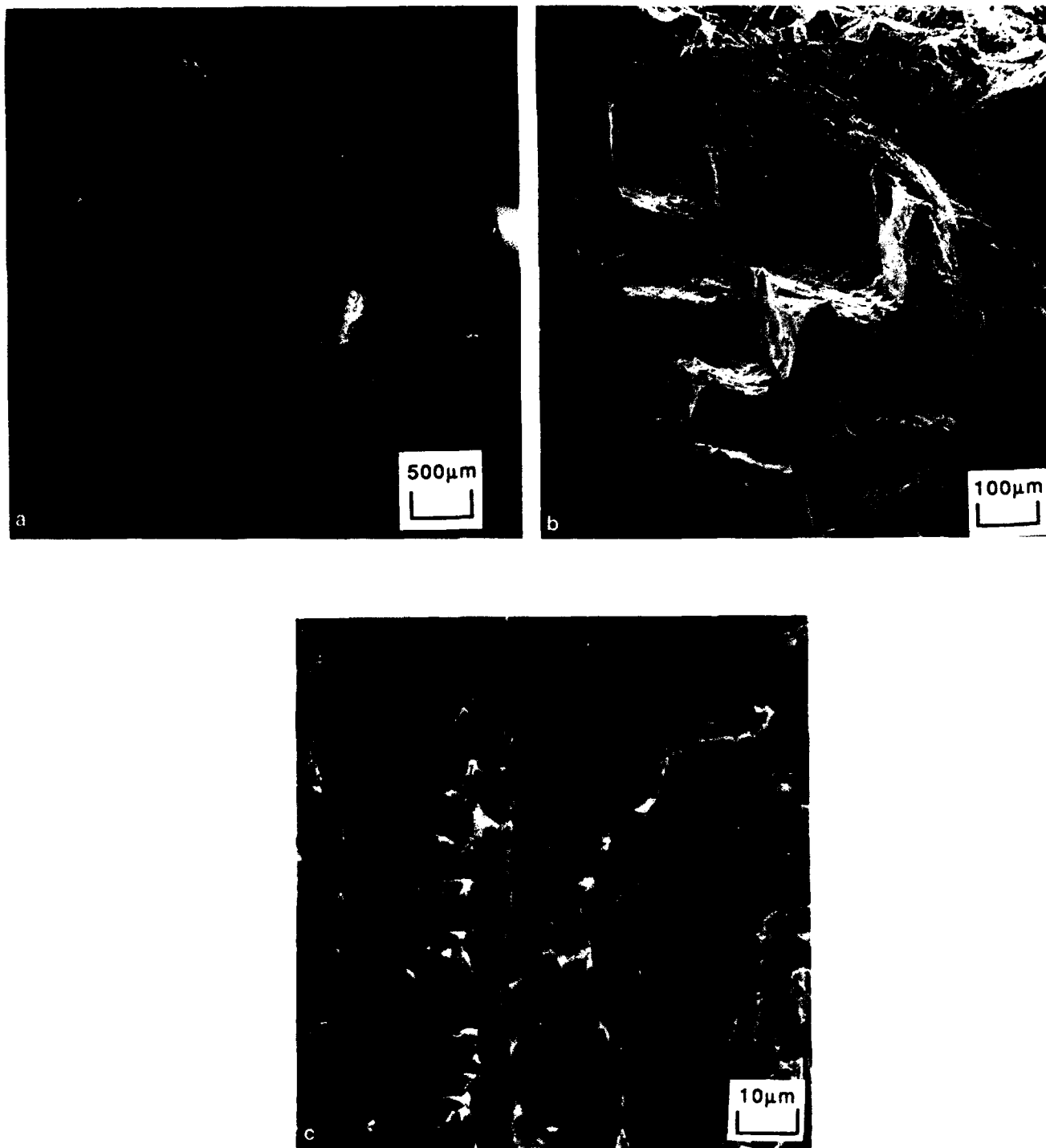


Figure 26. Tensile samples tested at RT in air - Heat treatment A.

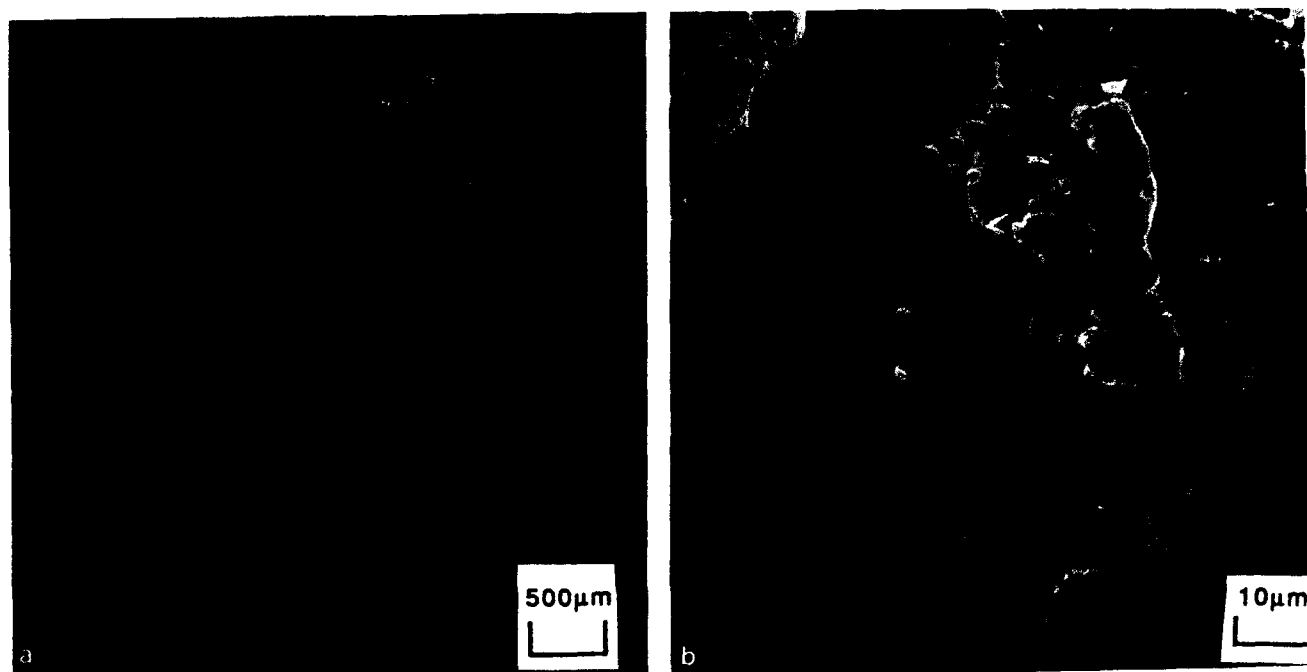


Figure 27. Tensile samples tested at RT in air - Heat treatment B.

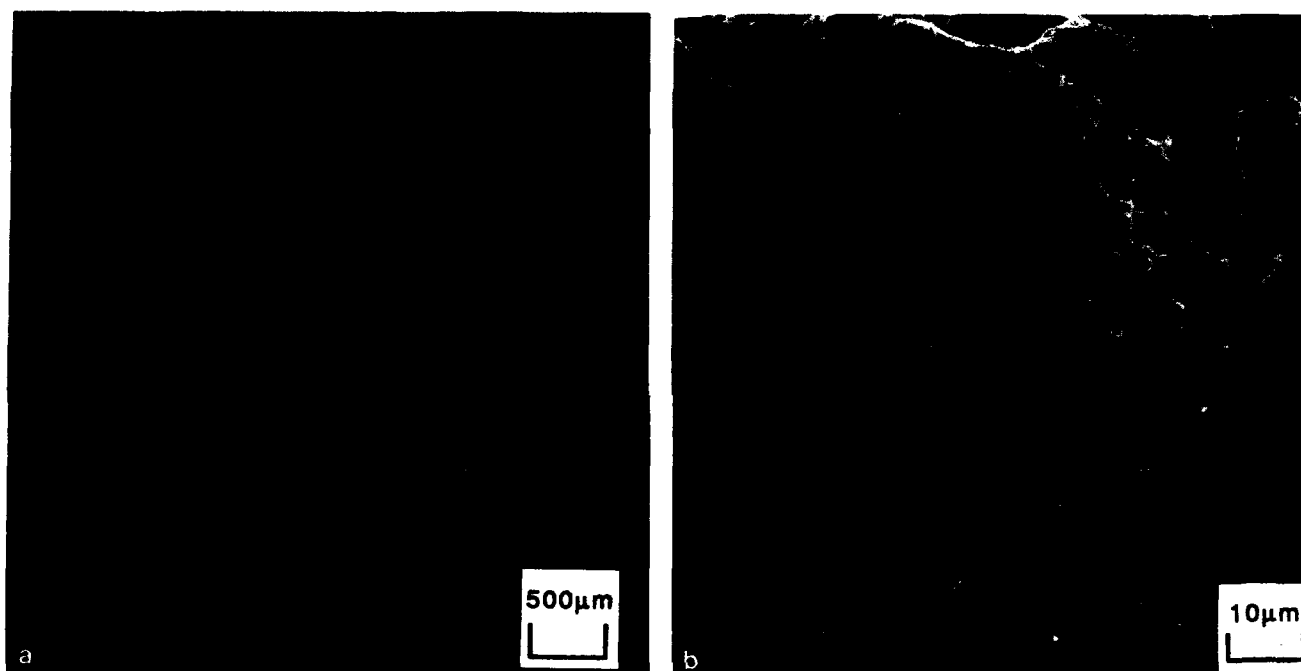


Figure 28. Tensile samples tested at RT in air - Heat treatment C.

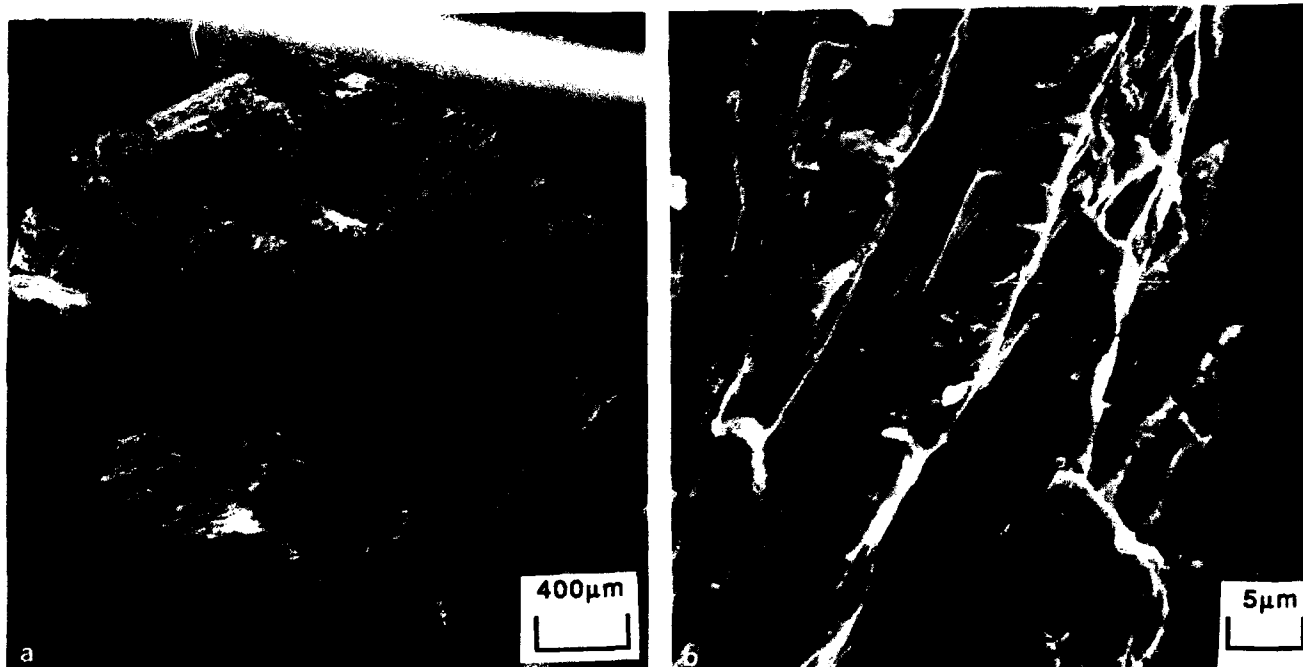


Figure 29. Tensile samples tested at 650°C in air - Heat treatment A.

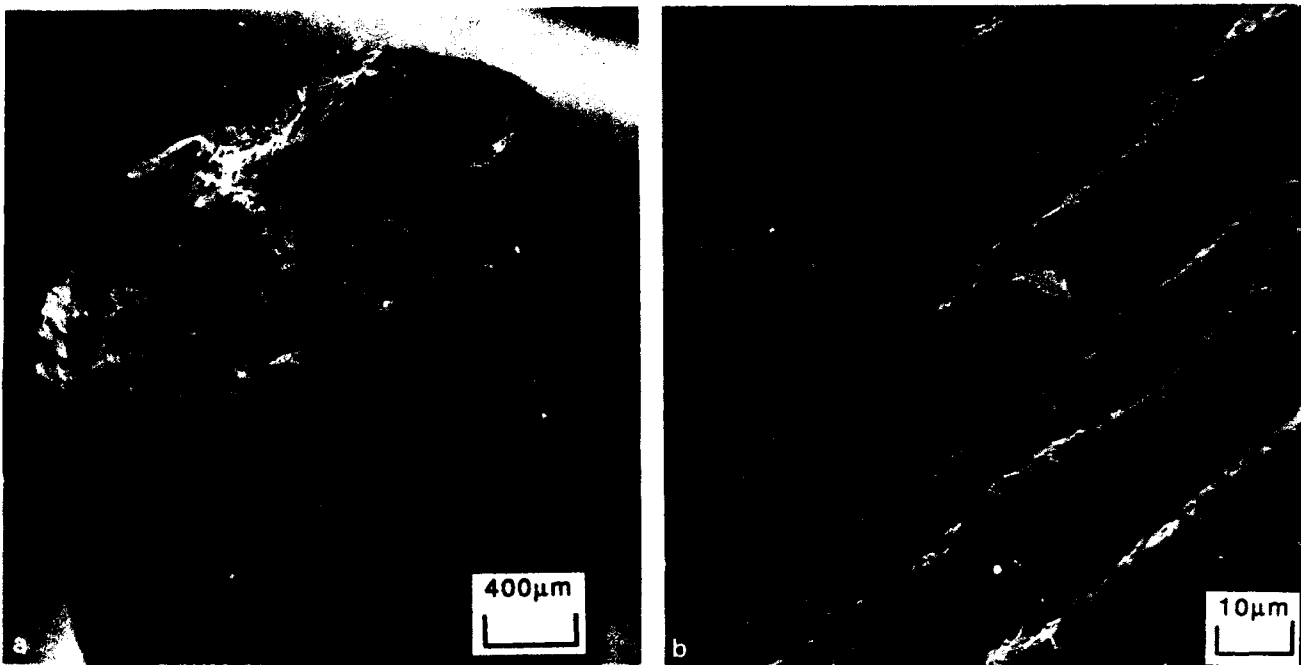


Figure 30. Tensile samples tested at 650°C in vacuum - Heat treatment A.

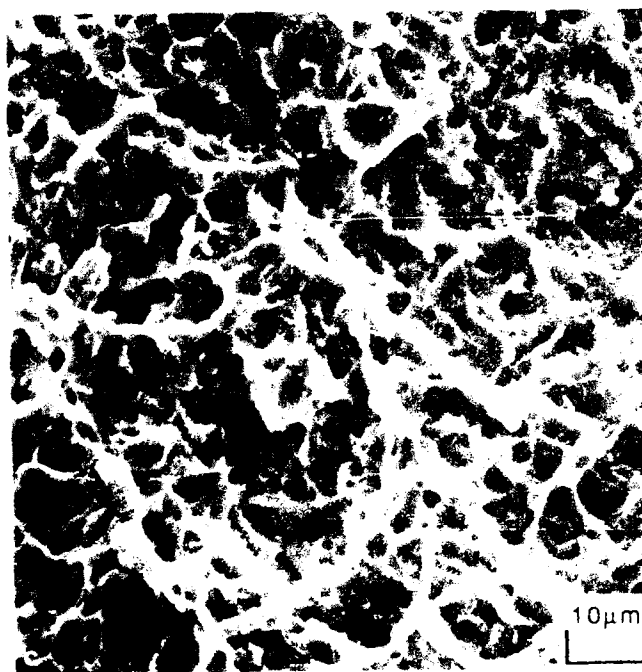
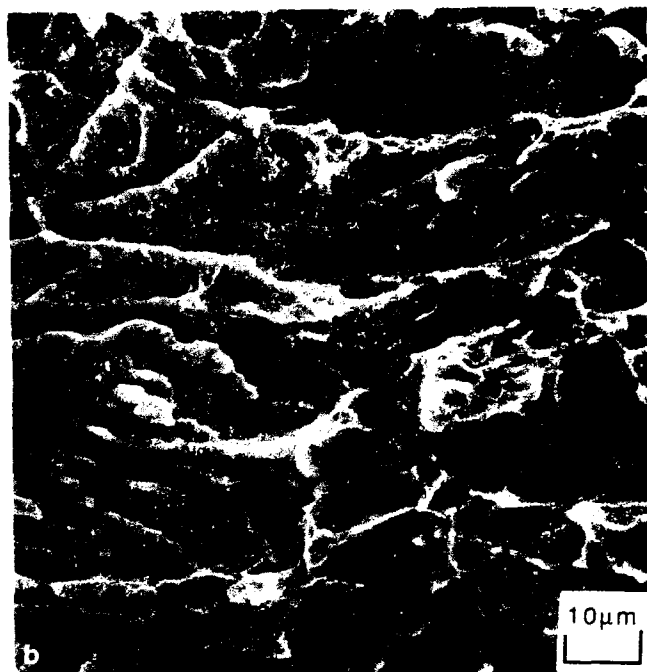
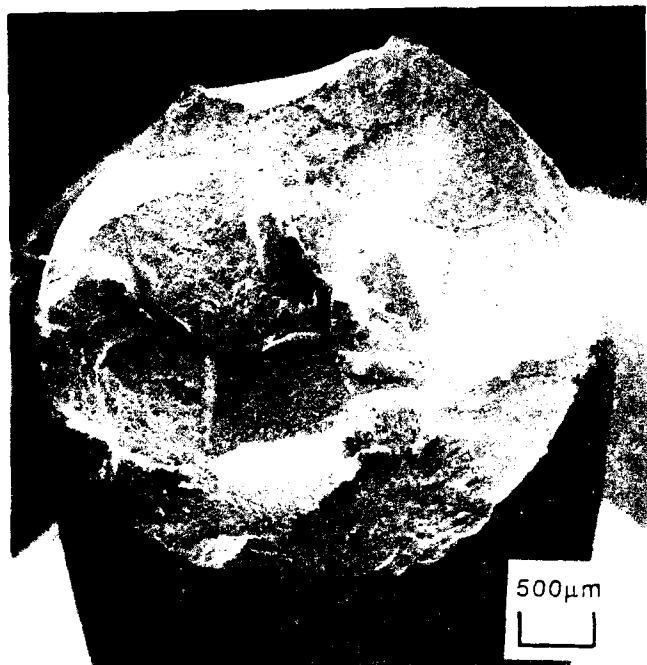


Figure 31. Tensile samples tested at 650°C in air - Heat treatment B.

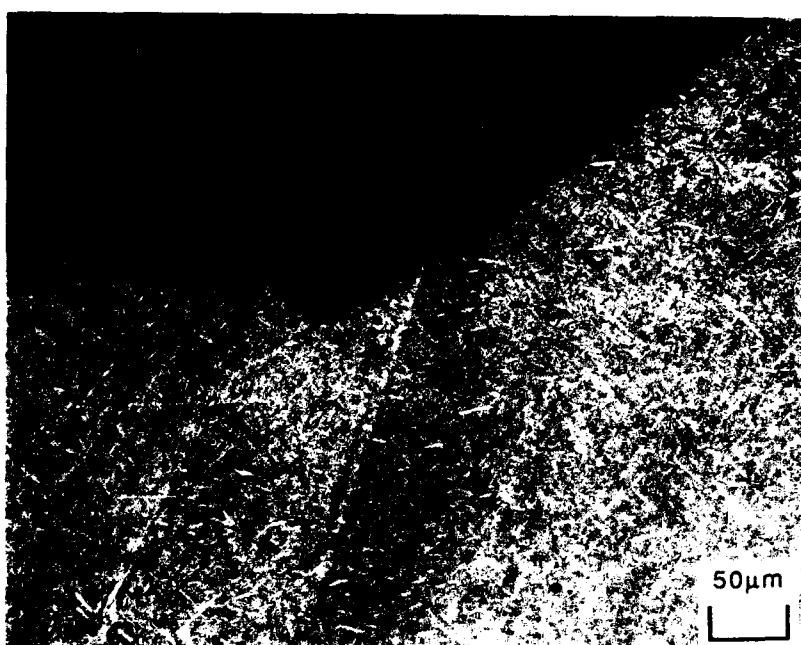


Figure 32. Cross-sectional view of tensile sample tested at 650°C in air - Heat treatment B.

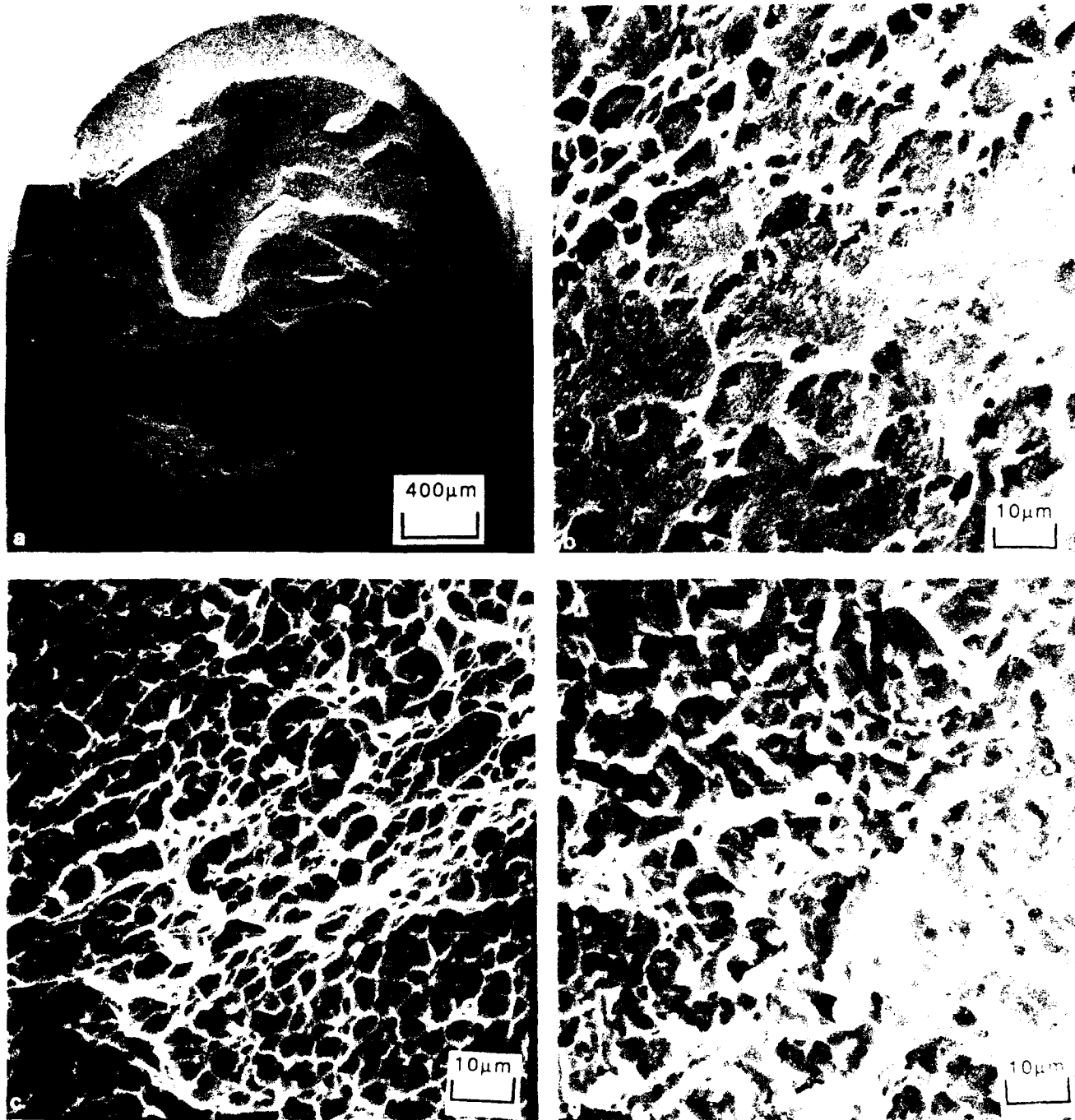


Figure 33. Tensile samples tested at 650°C in vacuum - Heat treatment B.

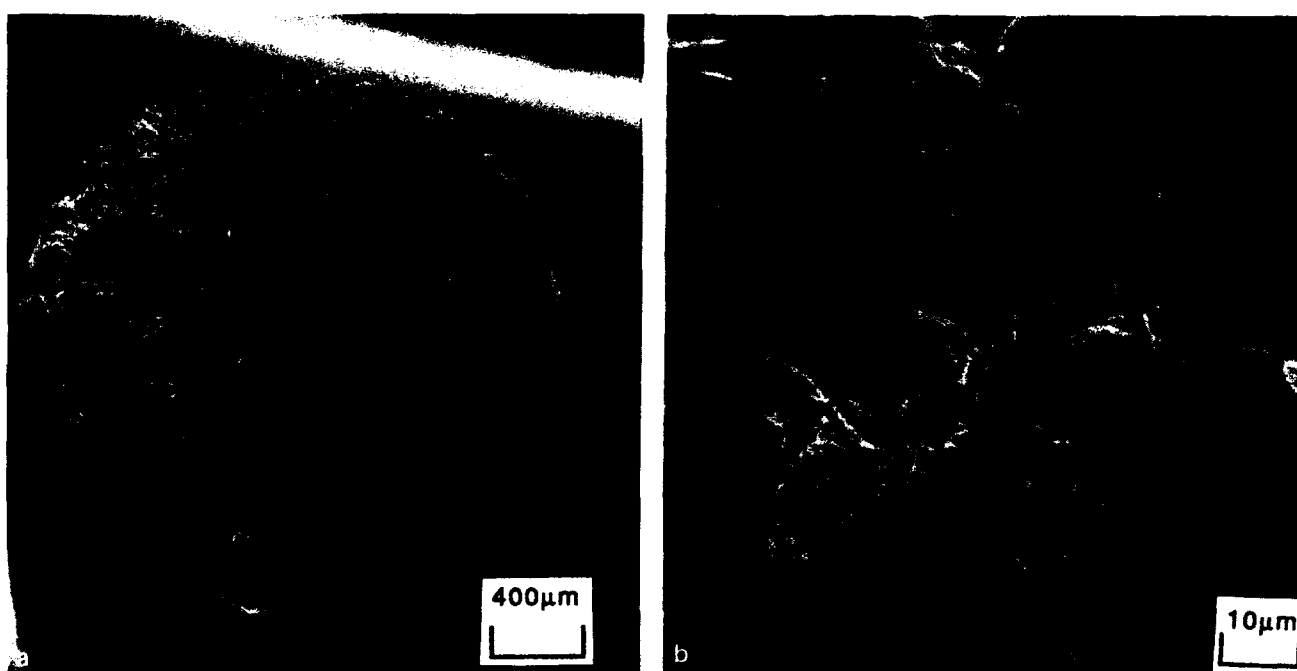


Figure 34. Tensile samples tested at 650°C in air - Heat treatment C.

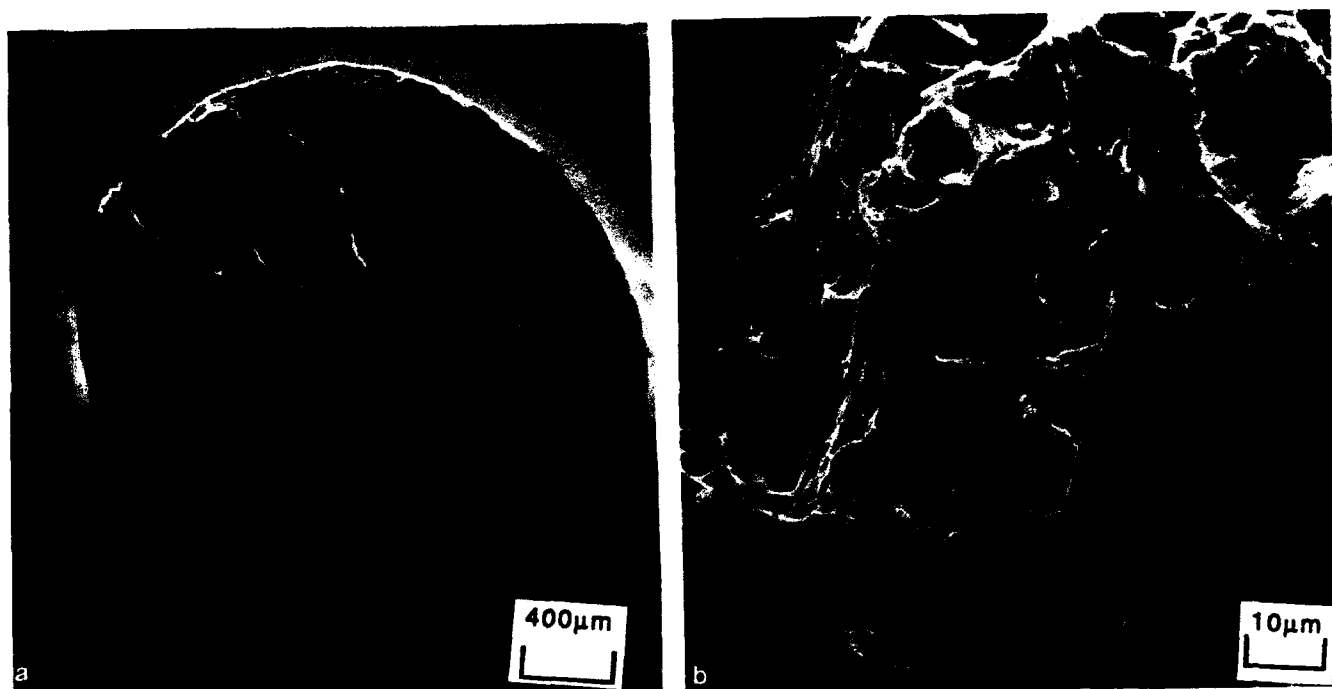


Figure 35. Tensile samples tested at 650°C in vacuum - Heat treatment C.

Creep Rupture Test Data For Ti3Al At 650°C

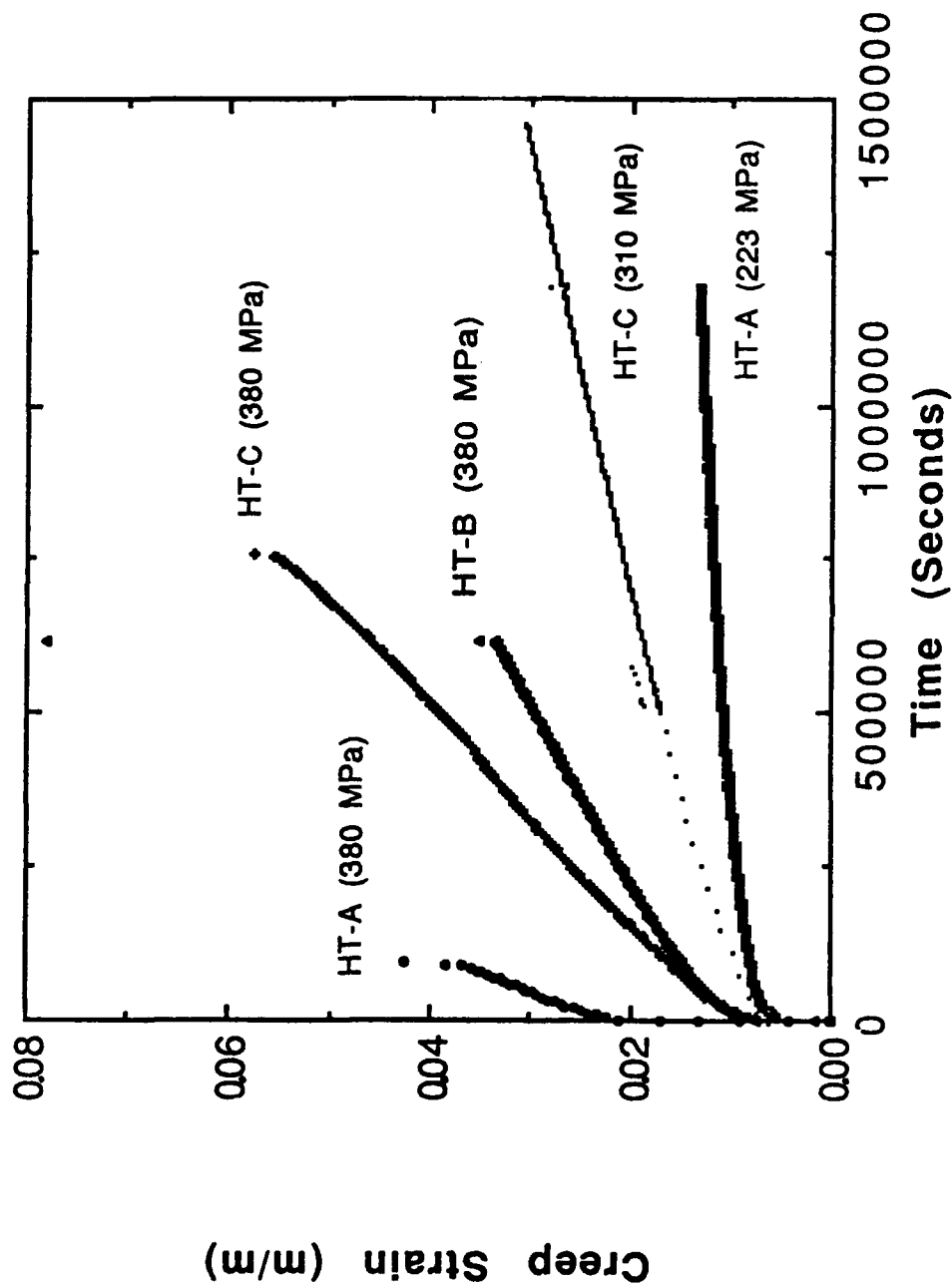


Figure 36. Creep strain versus time plots for specimens tested from the three heat treatments.

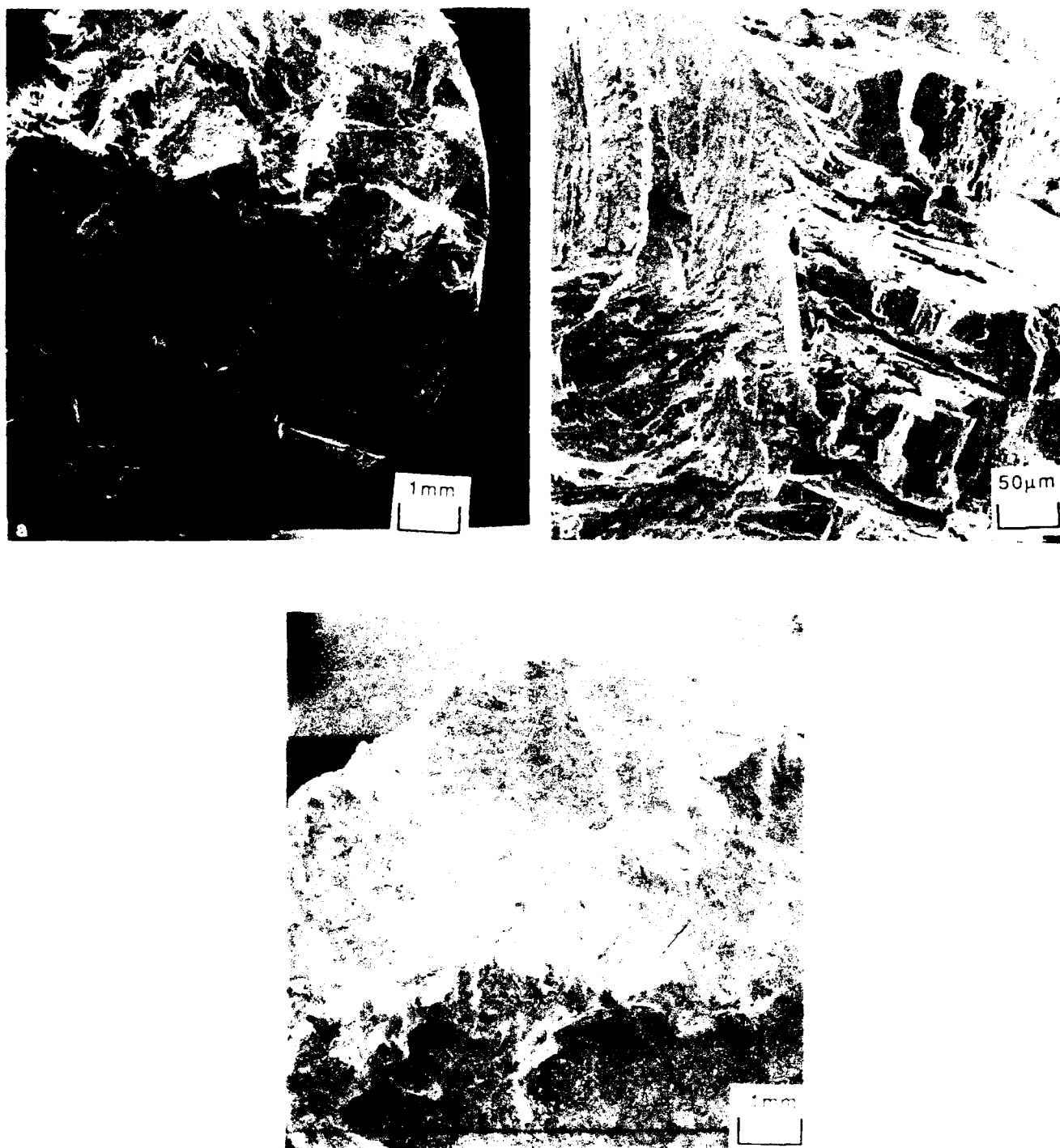


Figure 37. Creep rupture specimens tested at 650°C in air - Heat treatment A.

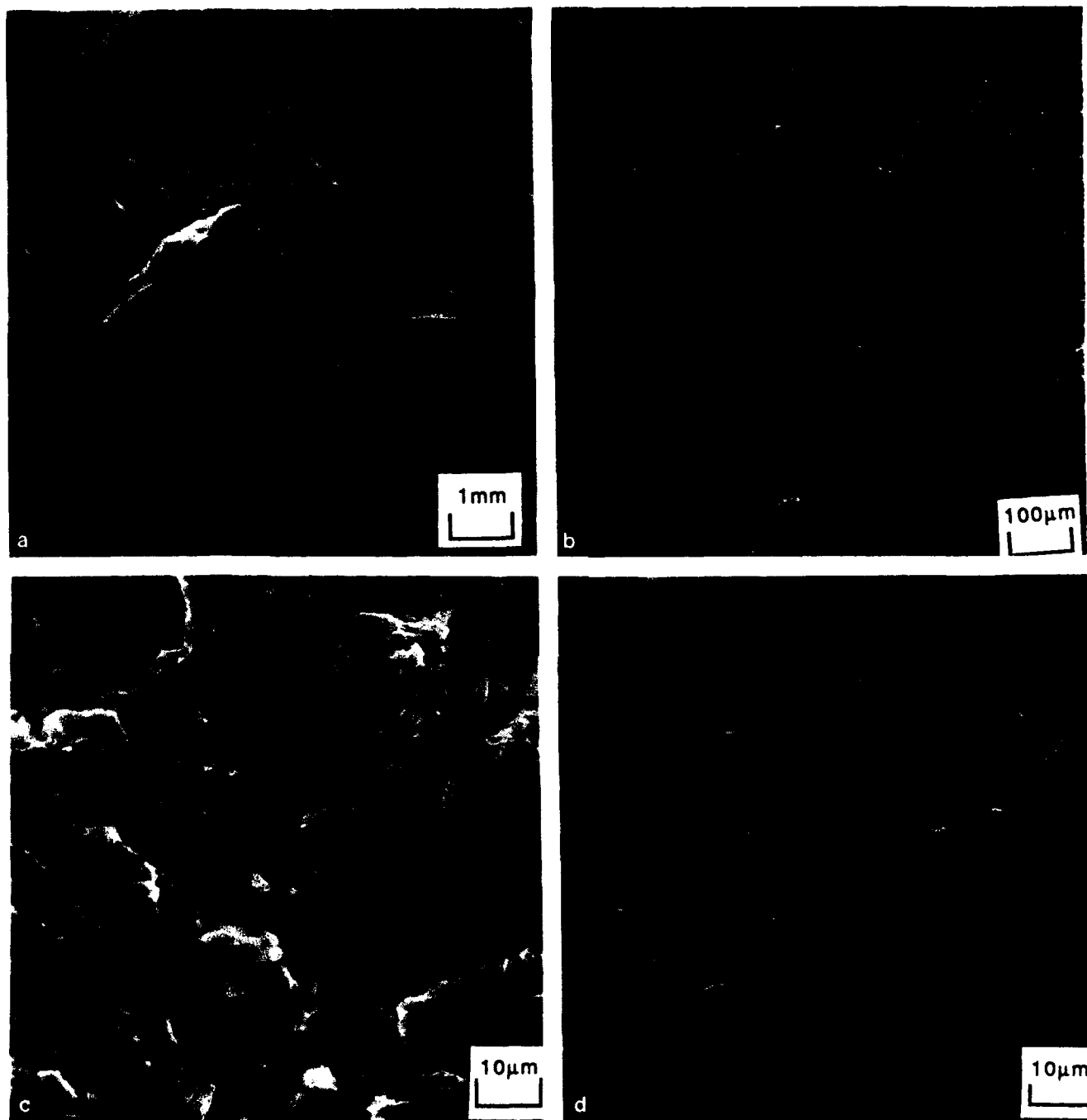


Figure 38. Creep rupture specimens tested at 650°C in air - Heat treatment B.

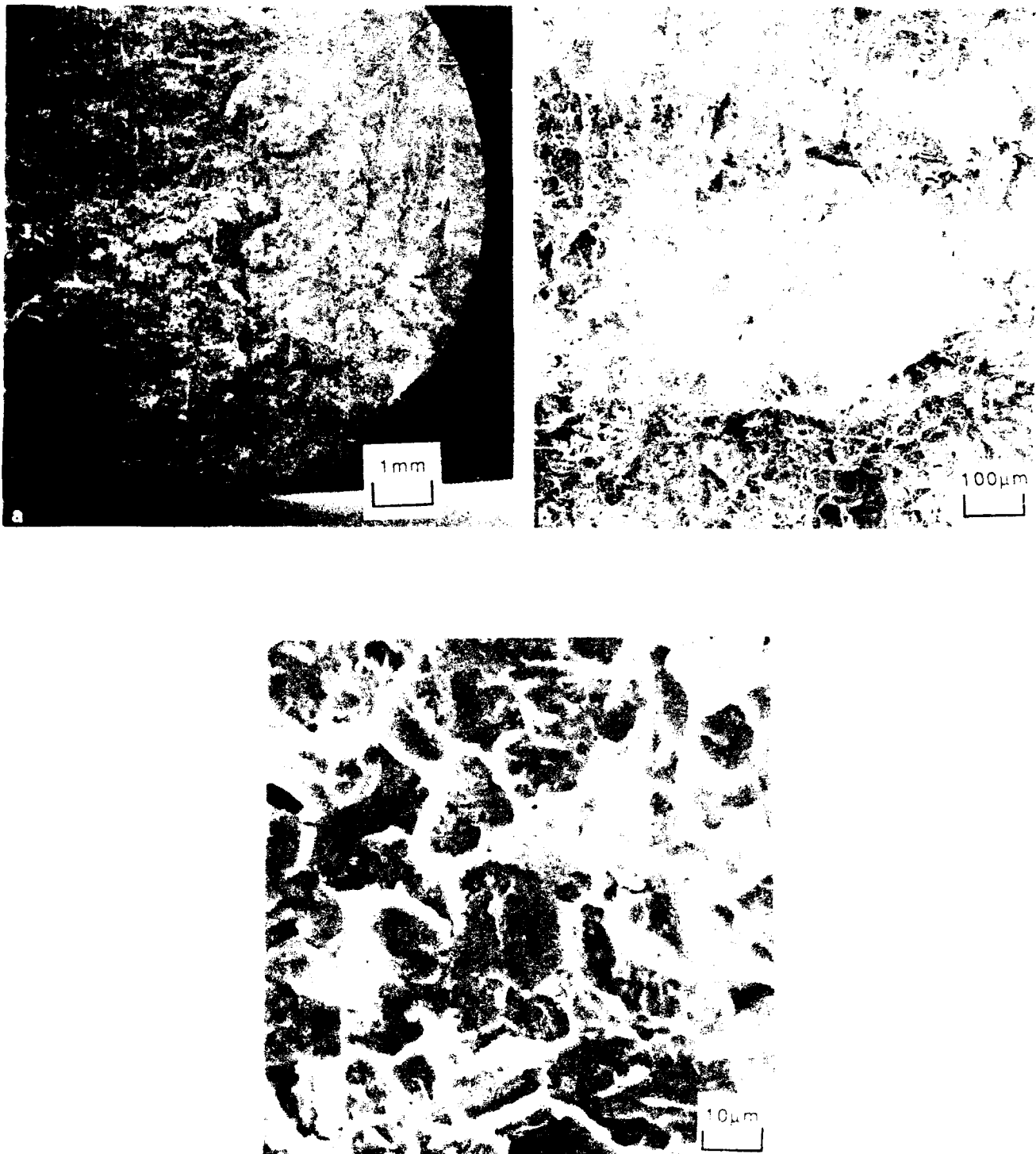


Figure 39. Creep rupture specimens tested at 650°C in air - Heat treatment C.

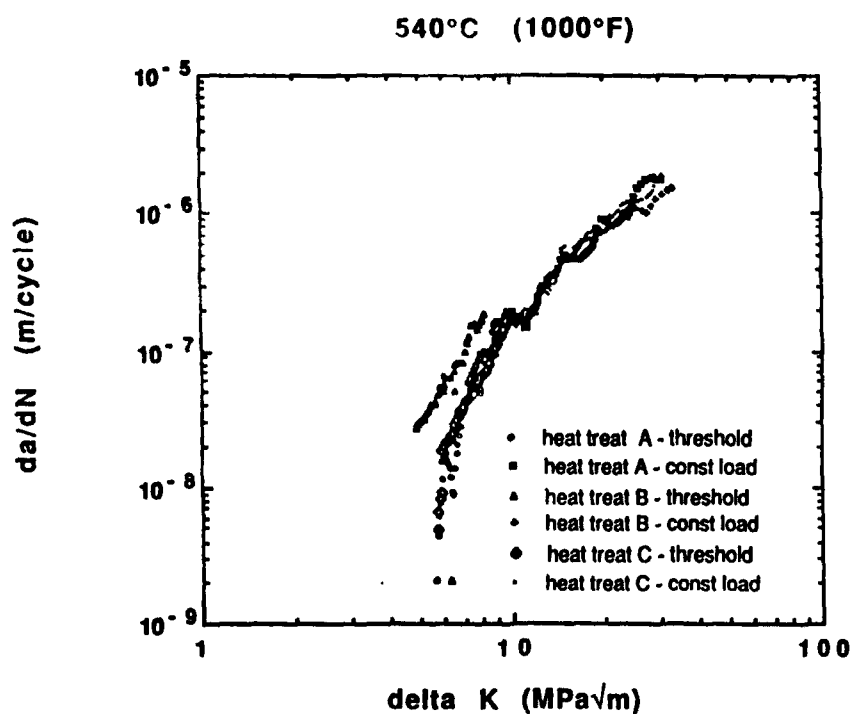


Figure 40. da/dN vs ΔK for the three heat treatments at test temperature of 540°C

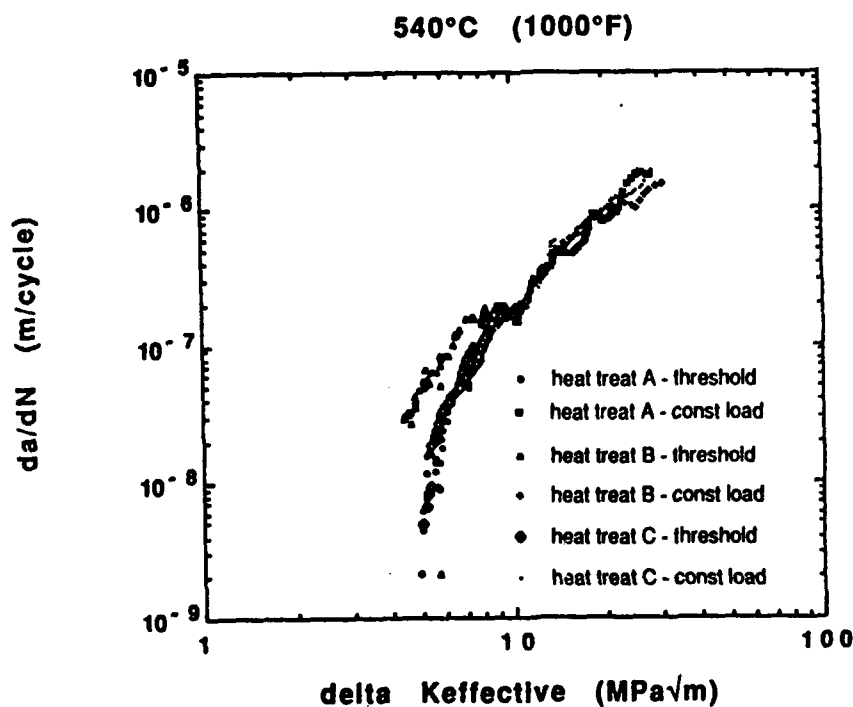


Figure 41. da/dN vs $\Delta K_{\text{effective}}$ for the three heat treatments at test temperature of 540°C

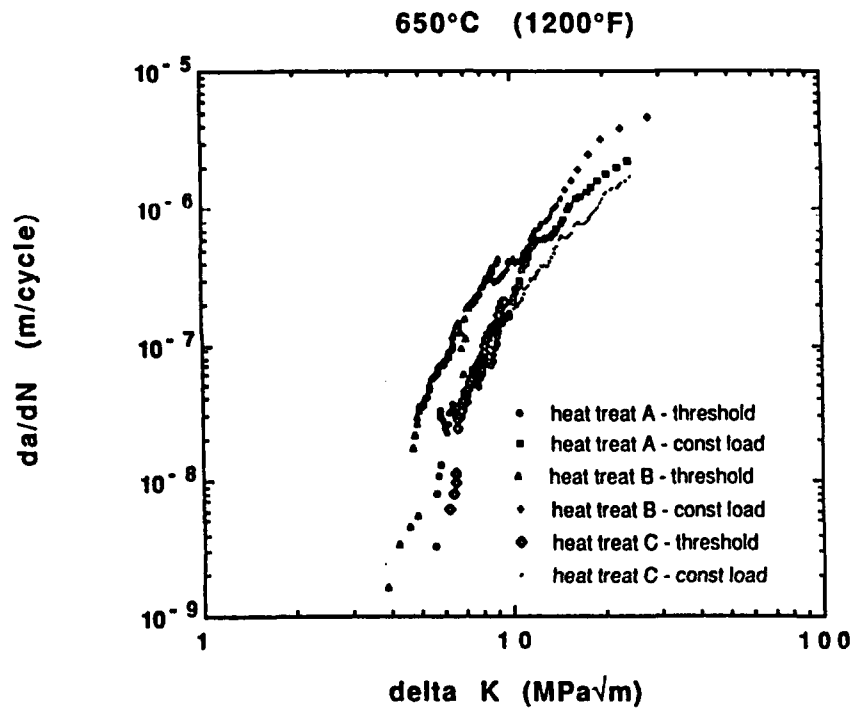


Figure 42. da/dN vs ΔK for the three heat treatments at test temperature of 650°C

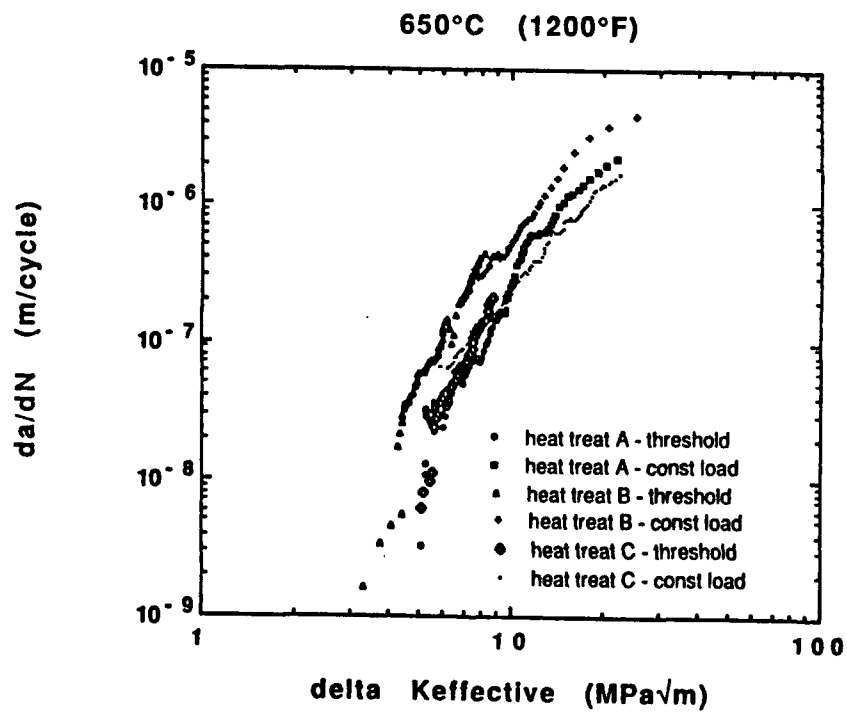


Figure 43. da/dN vs $\Delta K_{\text{effective}}$ for the three heat treatments at test temperature of 650°C

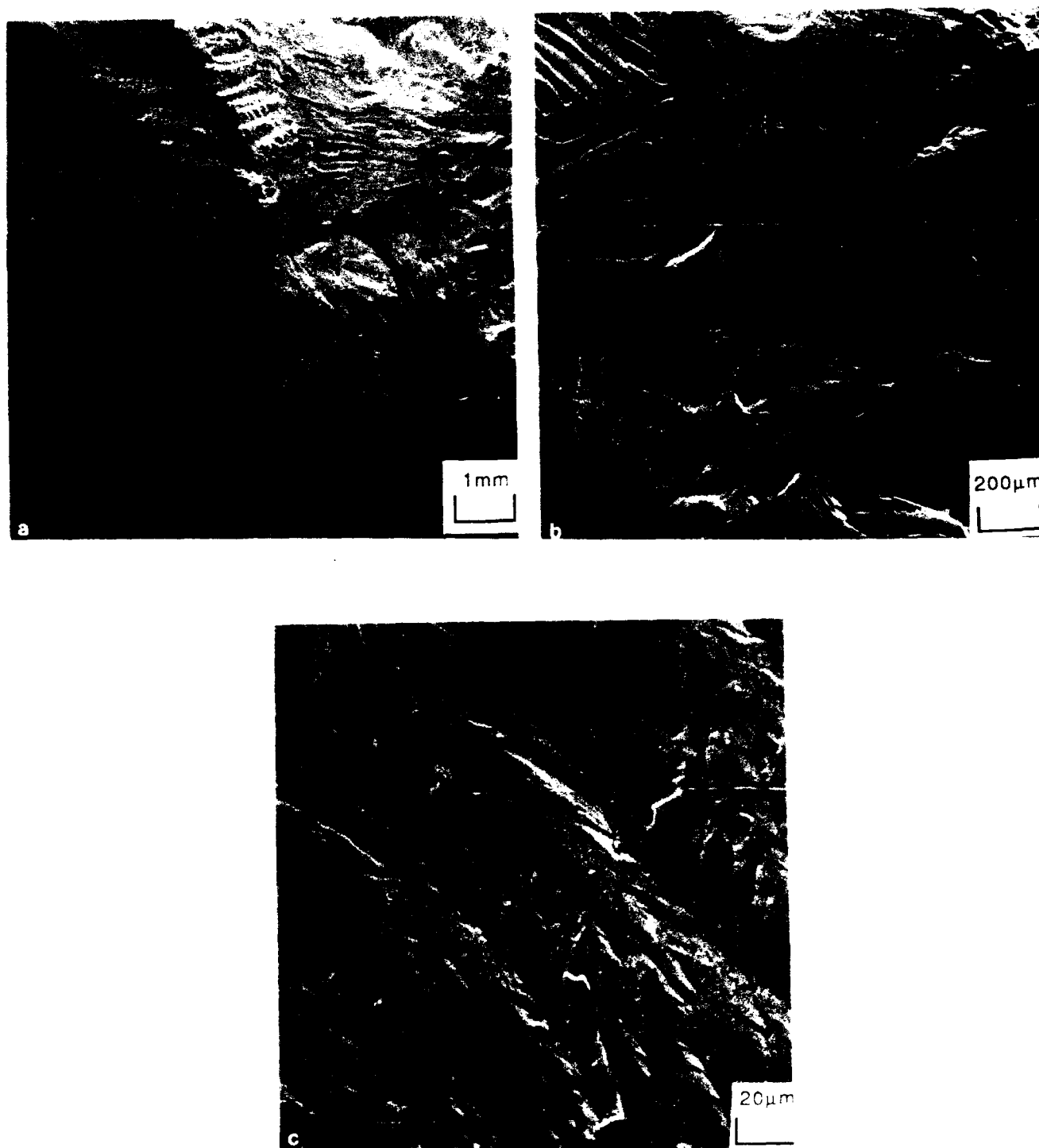


Figure 44. Fatigue crack growth specimens tested at 650°C in air - Heat treatment A.

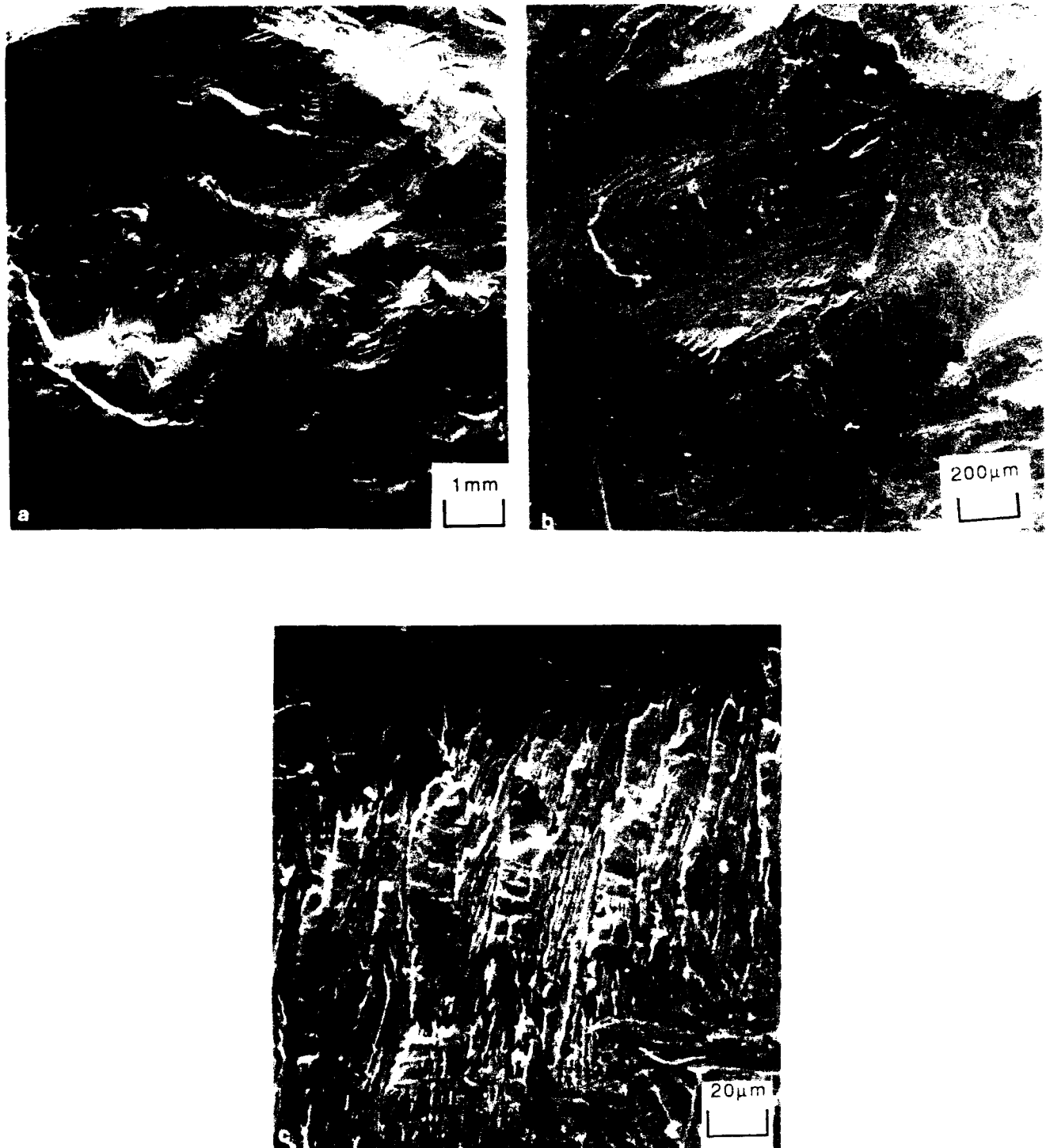


Figure 45. Fatigue crack growth specimens tested at 540°C in air - Heat treatment A.

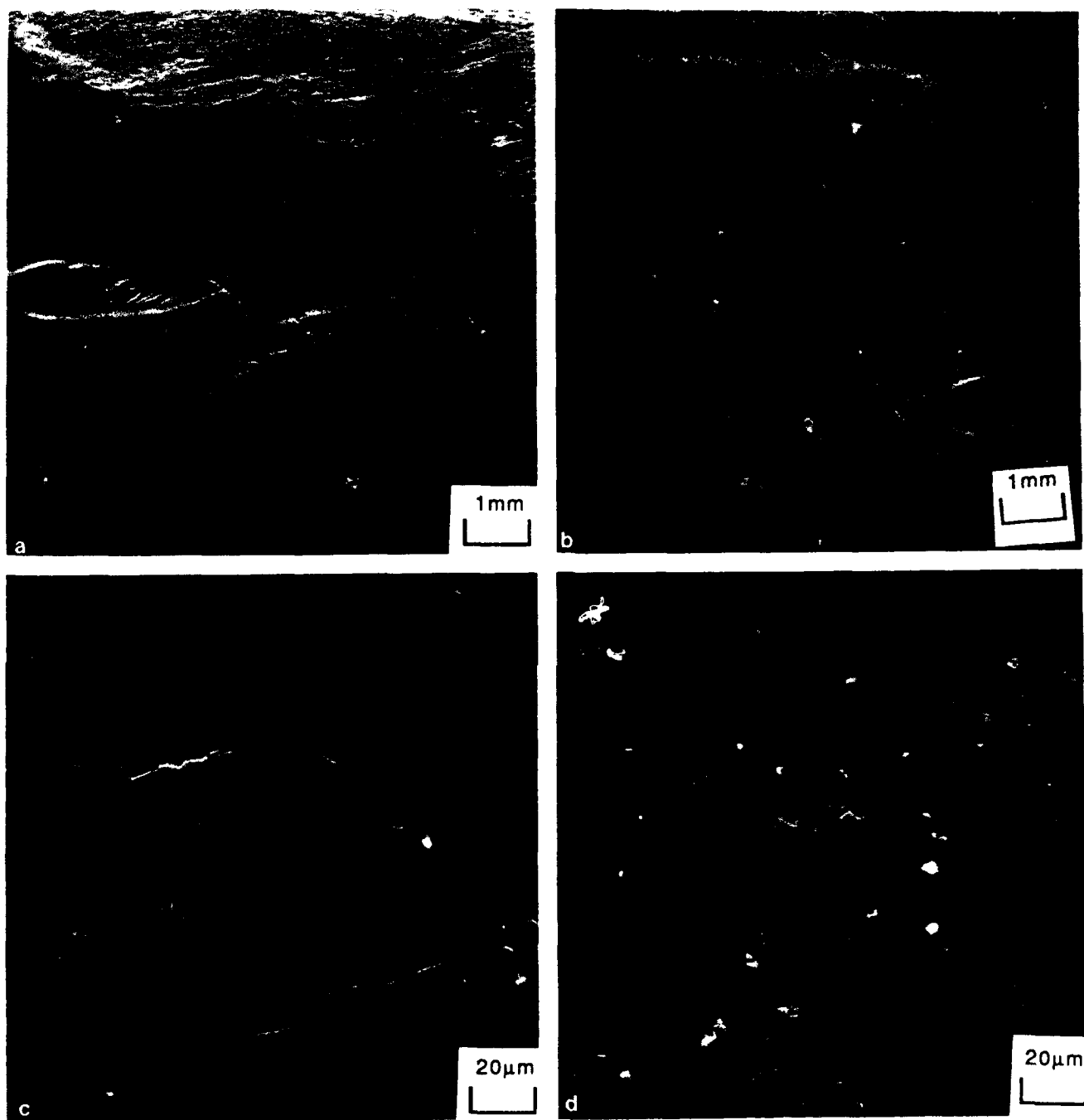


Figure 46. Fatigue crack growth specimens tested at 650°C in air - Heat treatment + B.

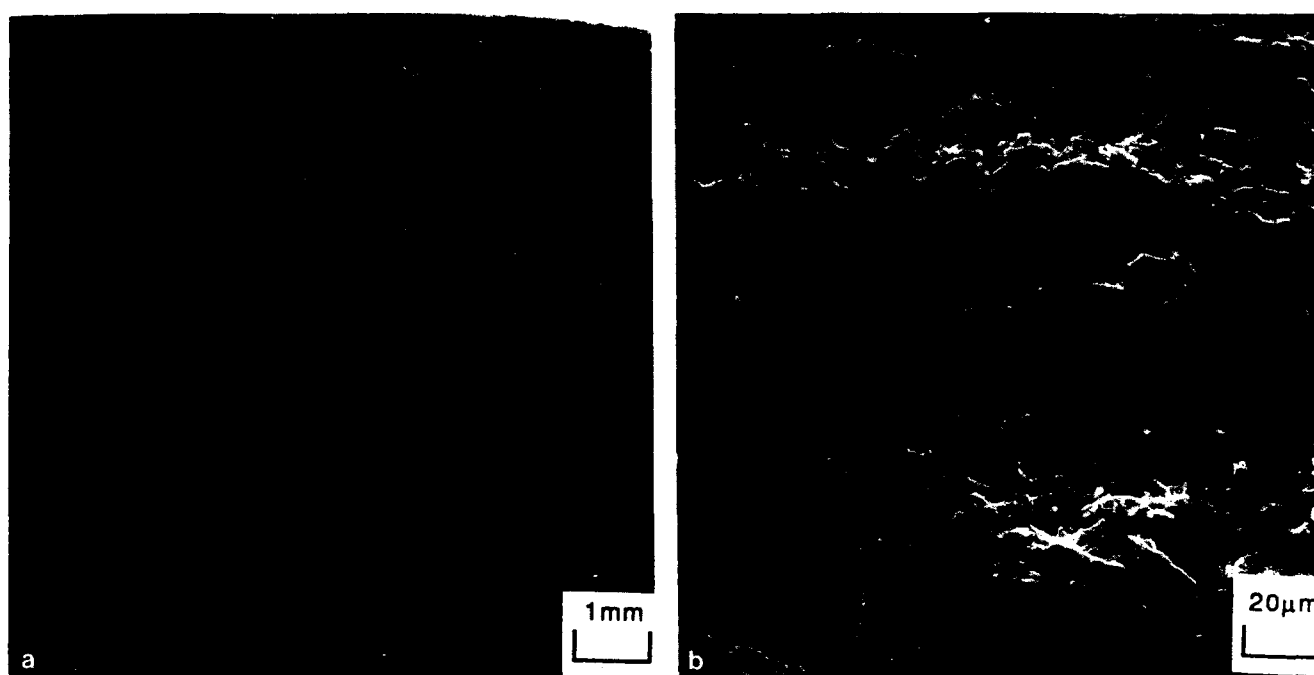


Figure 47. Fatigue crack growth specimens tested at 540°C in air - Heat treatment B.

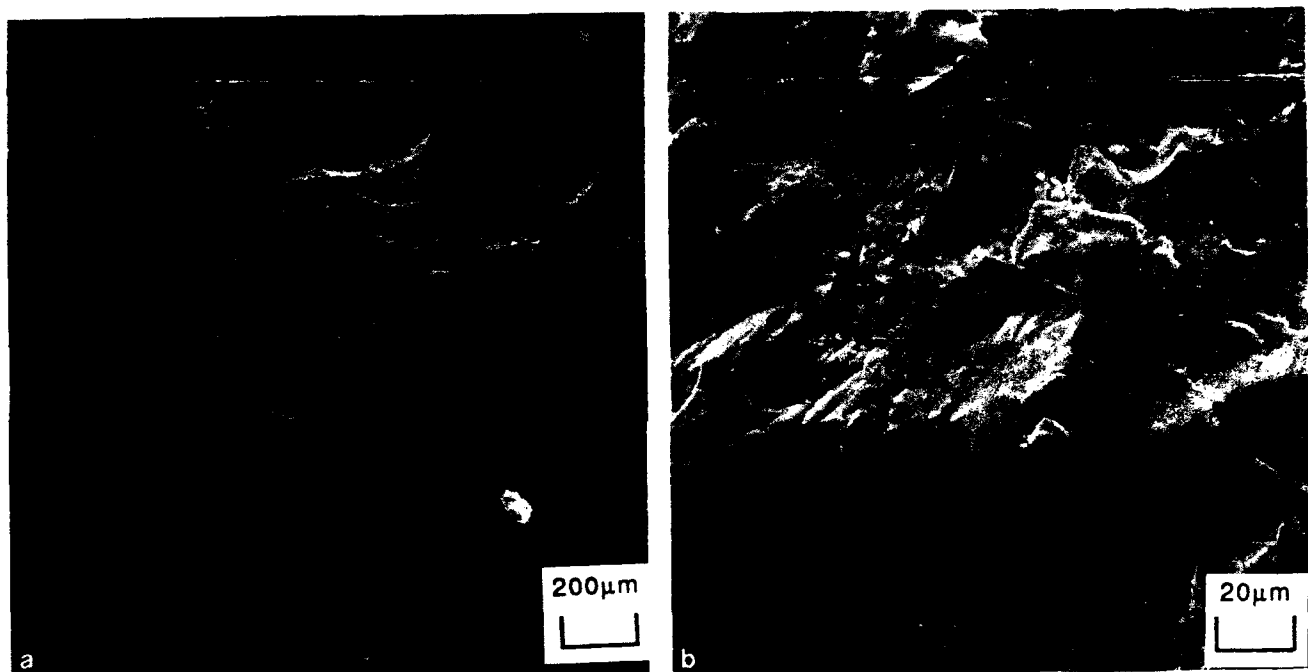


Figure 48. Fatigue crack growth specimens tested at 650°C in air - Heat treatment C.

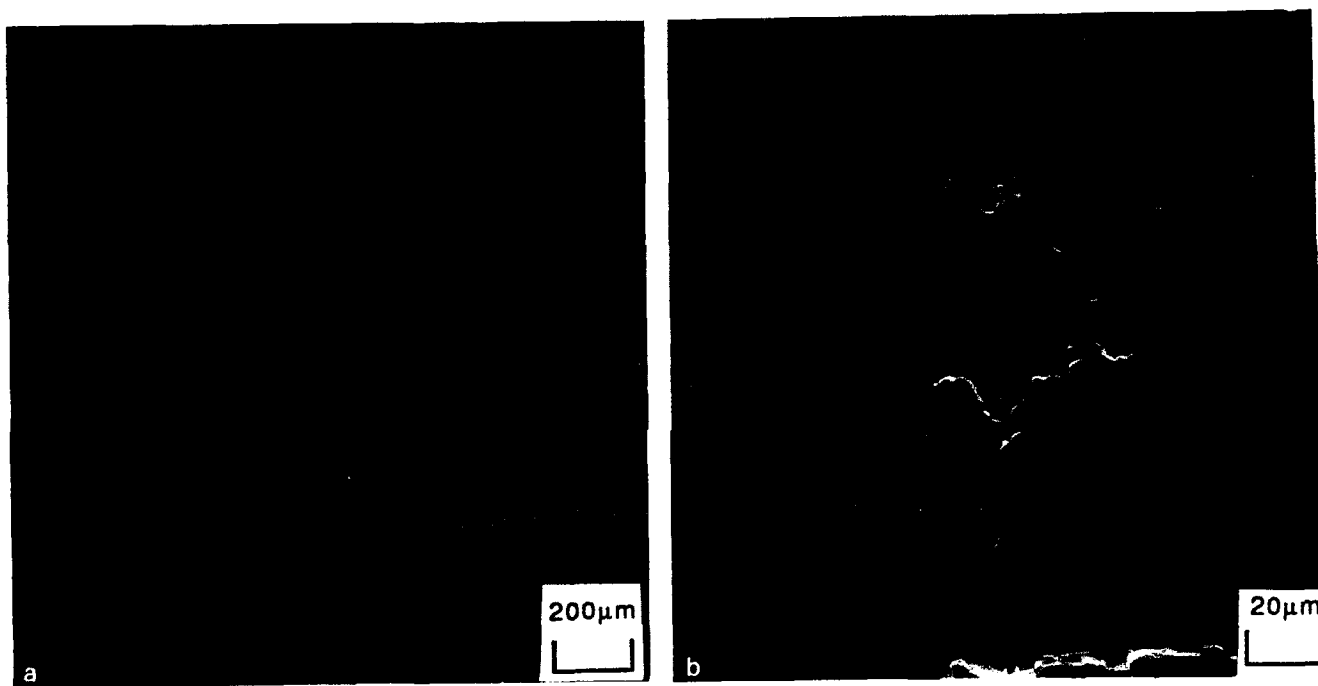


Figure 49. Fatigue crack growth specimens tested at 540°C in air - Heat treatment C.

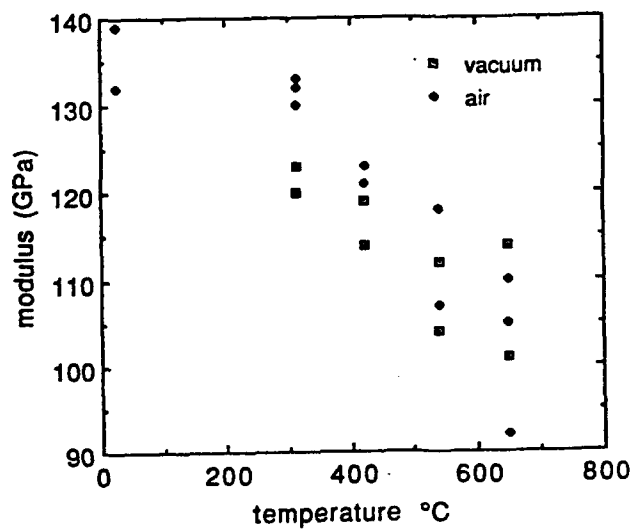


Figure 50. Elastic modulus versus test temperature in air and ultra-high vacuum environment for heat treatment C.

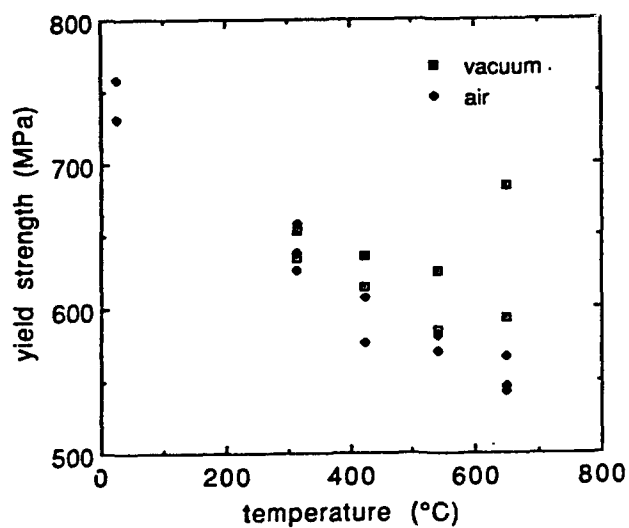


Figure 51. Yield strength versus test temperature in air and ultra-high vacuum environment for heat treatment C.

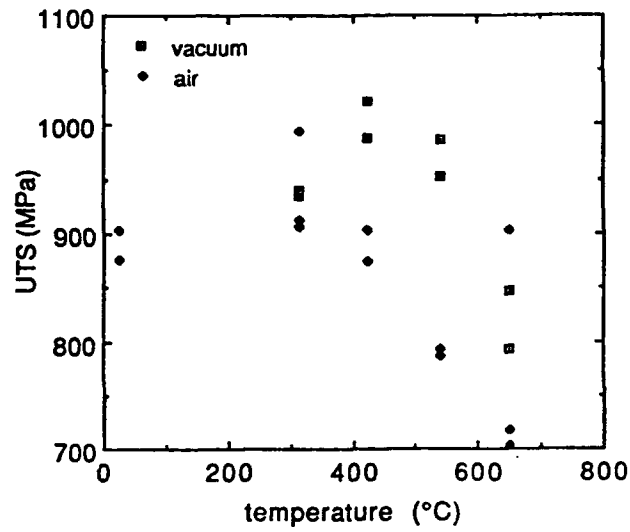


Figure 52. UTS versus test temperature in air and ultra-high vacuum environment for heat treatment C.

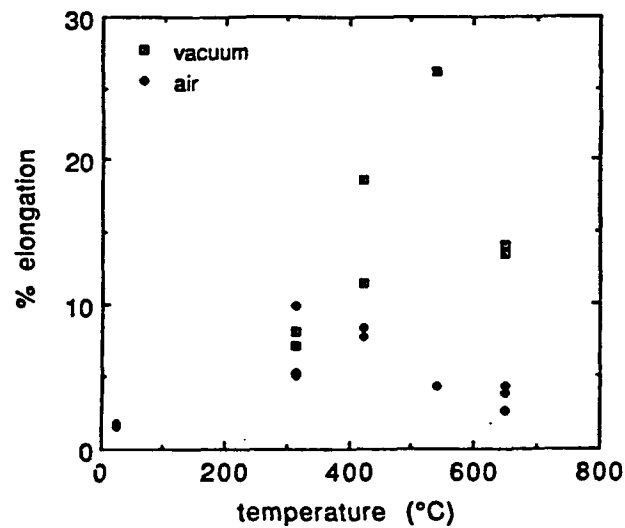


Figure 53. %elongation versus test temperature in air and ultra-high vacuum environment for heat treatment C.

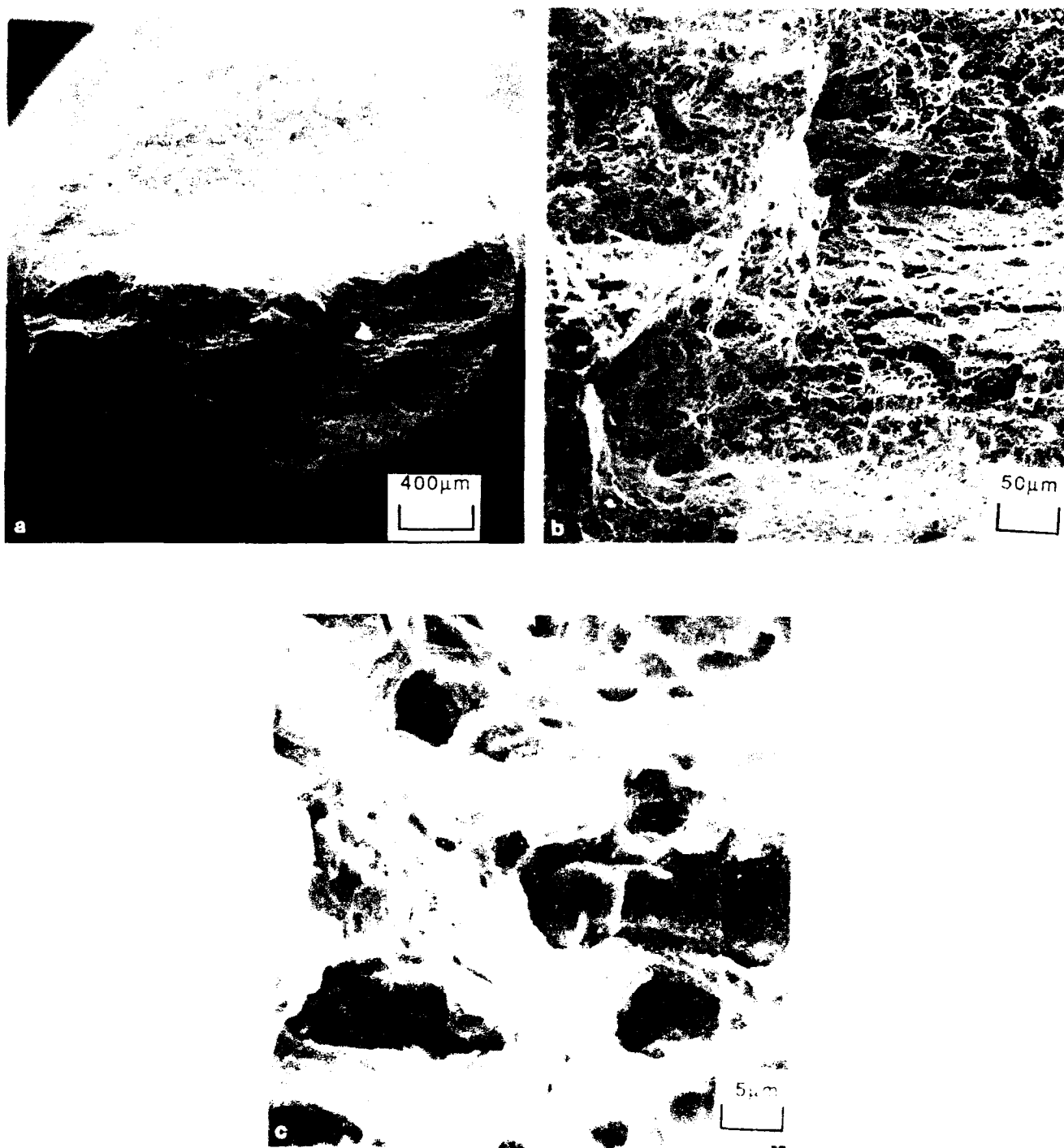


Figure 54. Tensile samples tested at 650°C in vacuum - Heat treatment C.

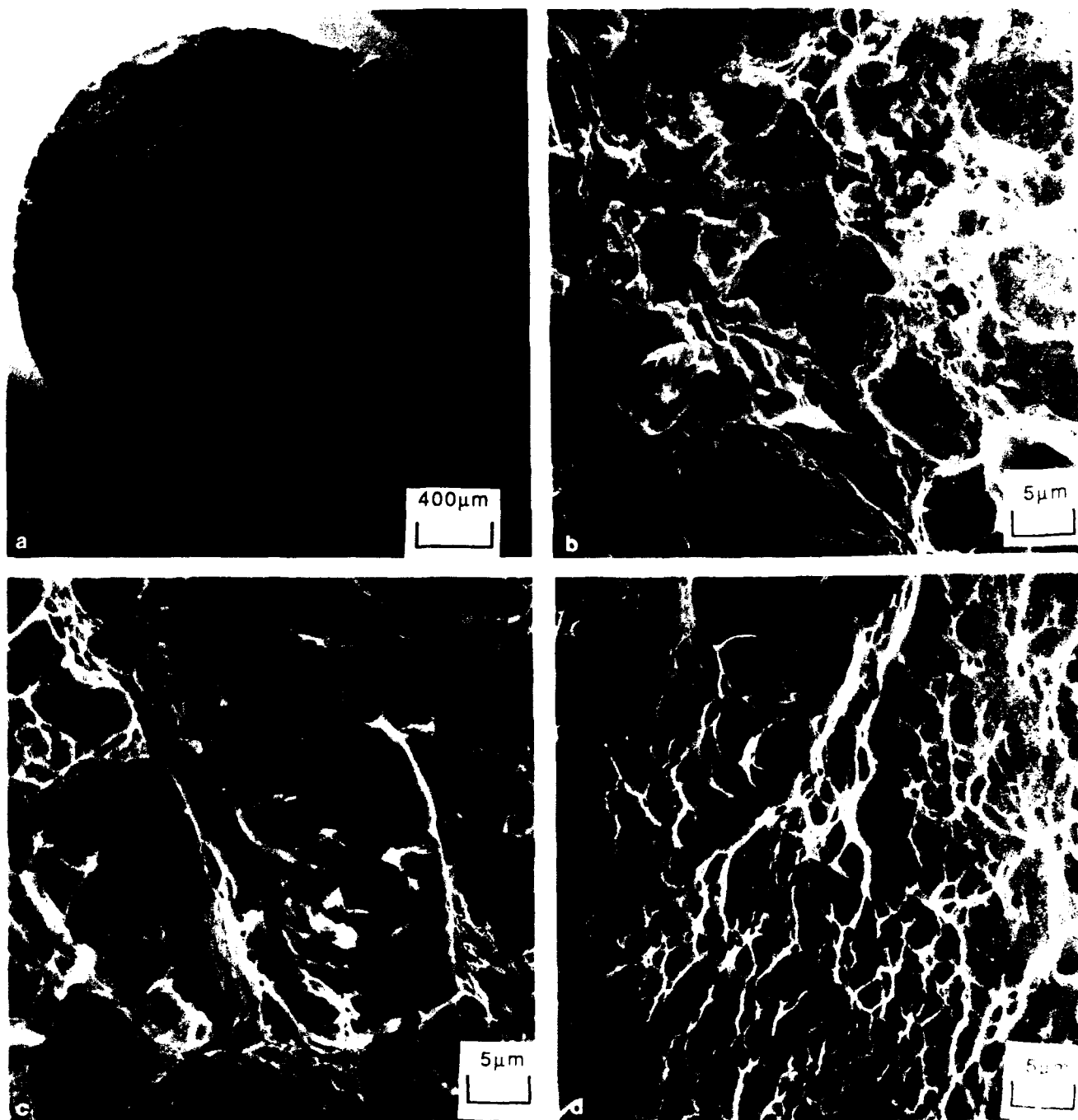


Figure 55. Tensile samples tested at 540°C in vacuum - Heat treatment C.

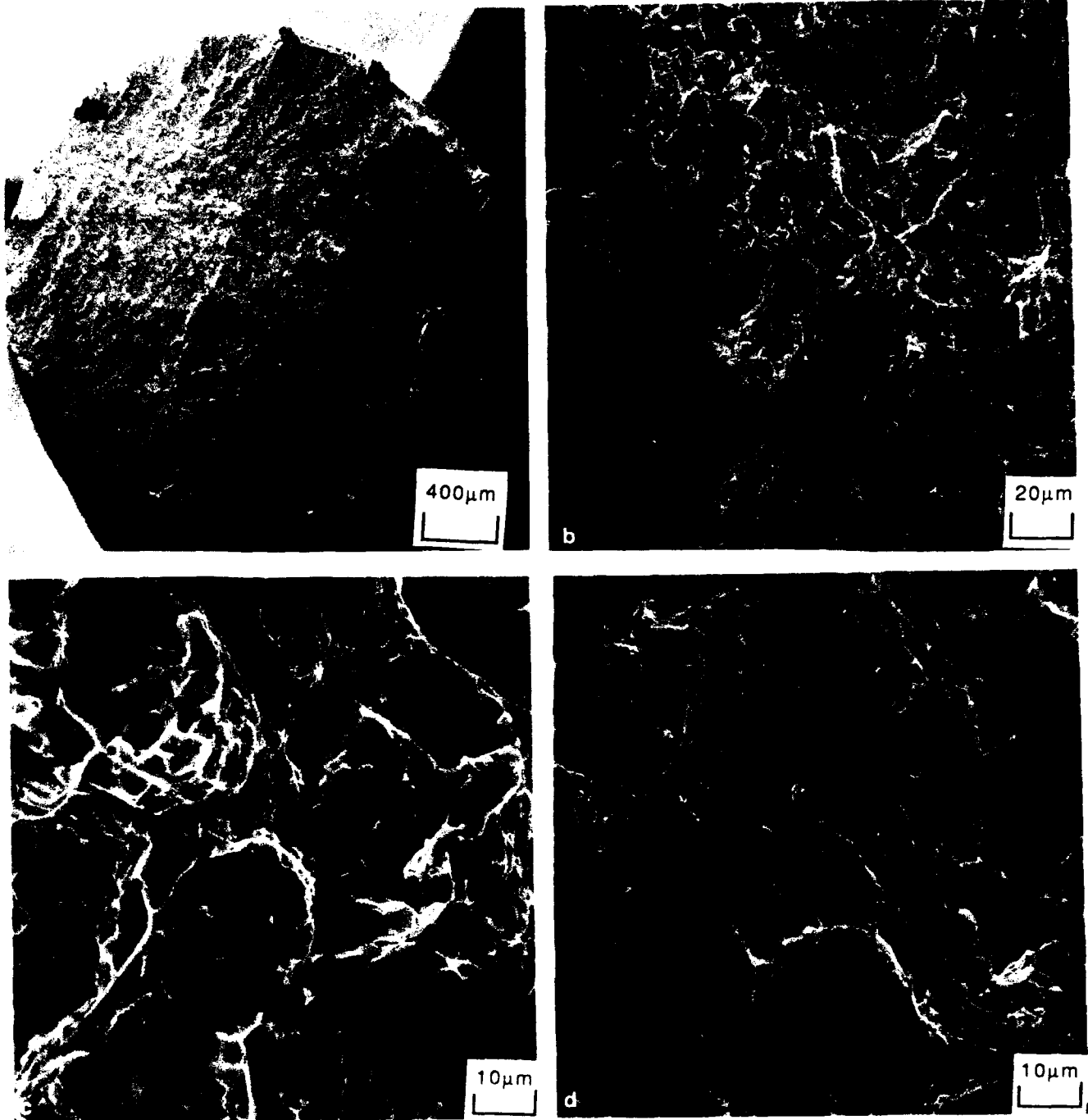


Figure 56. Tensile samples tested at 425°C in vacuum - Heat treatment C.

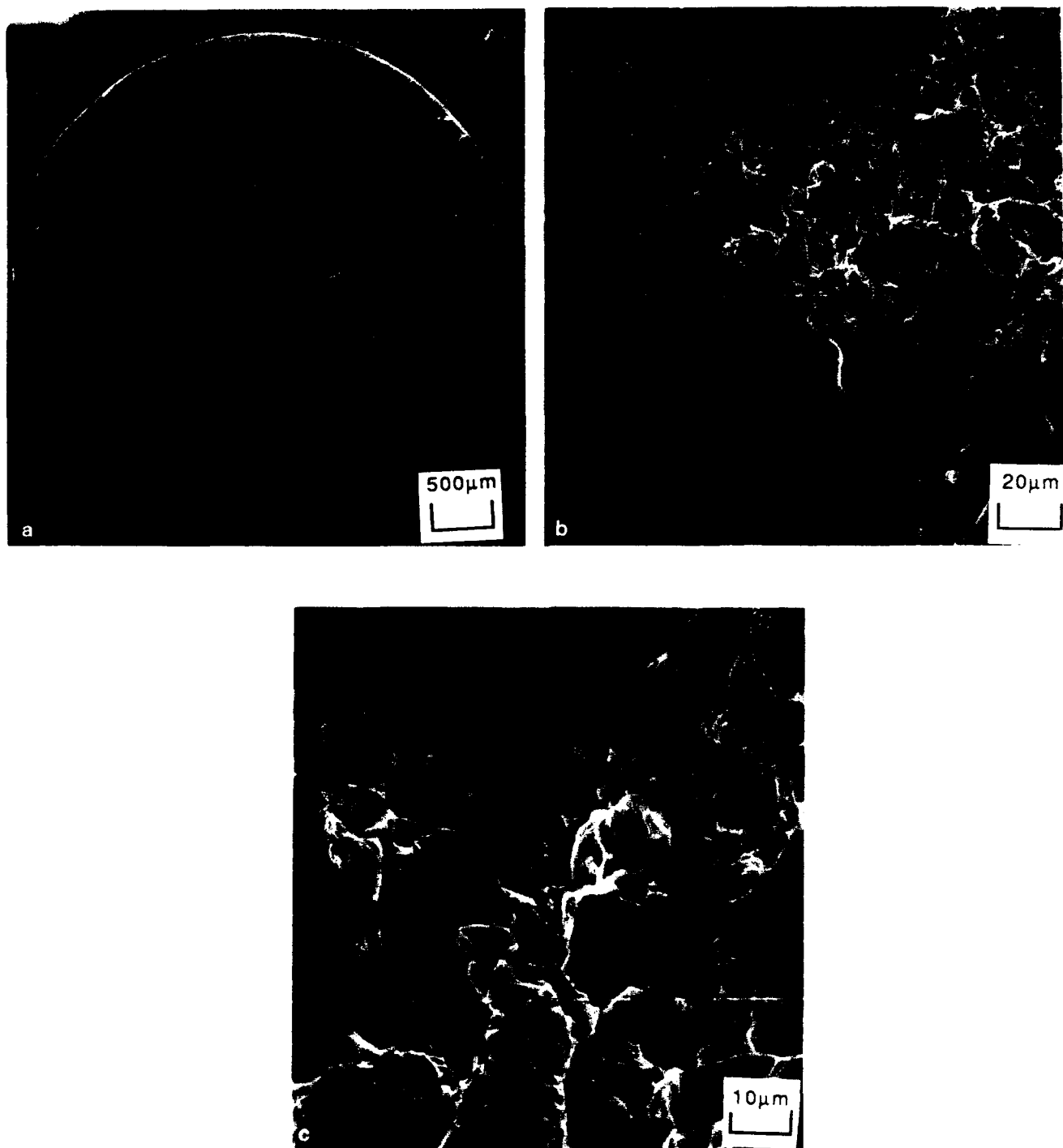


Figure 57. Tensile samples tested at 315°C in vacuum - Heat treatment C.

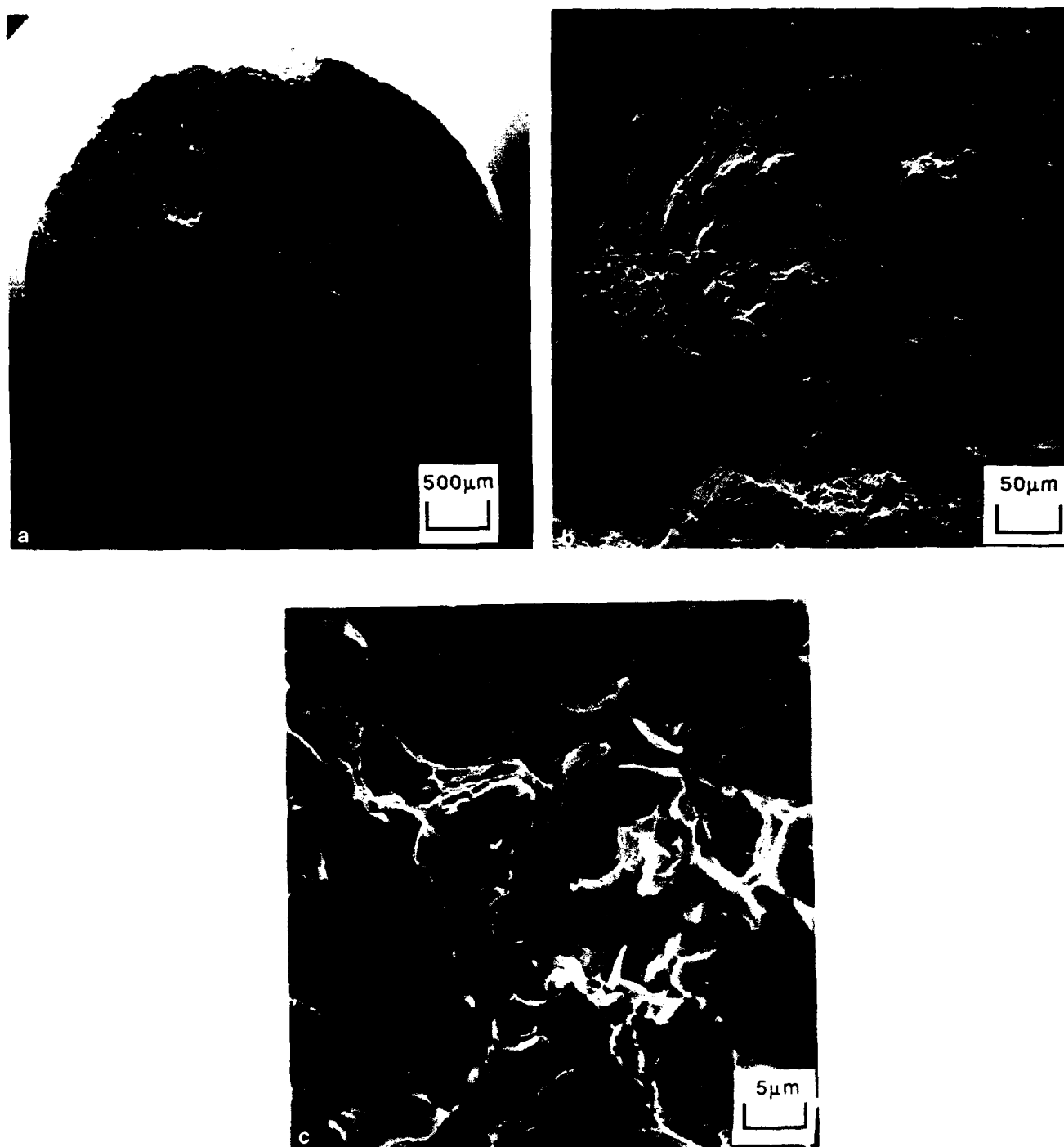


Figure 58. Tensile samples tested at 650°C in air - Heat treatment C.

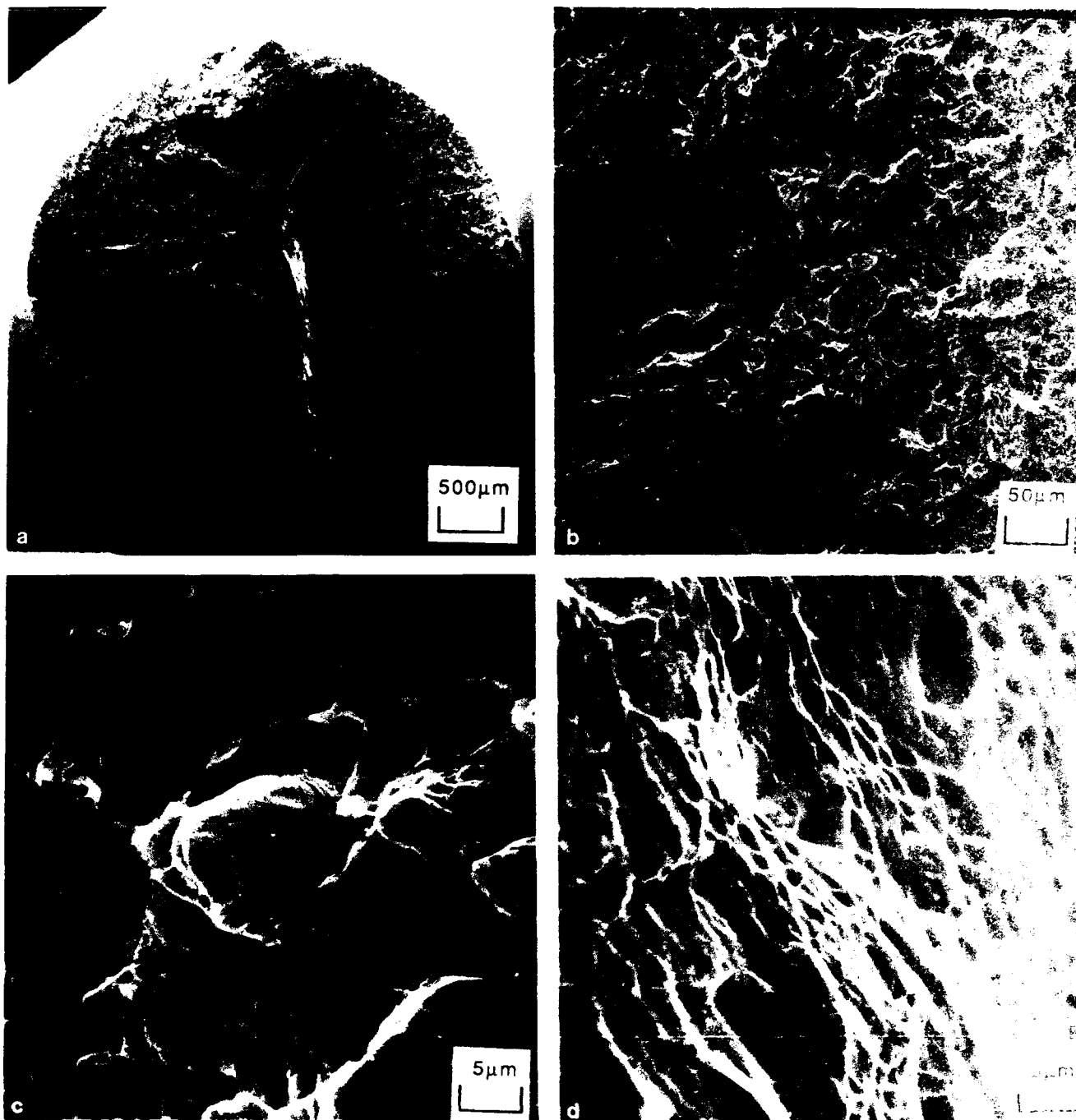


Figure 59. Tensile samples tested at 540°C in air - Heat treatment C.

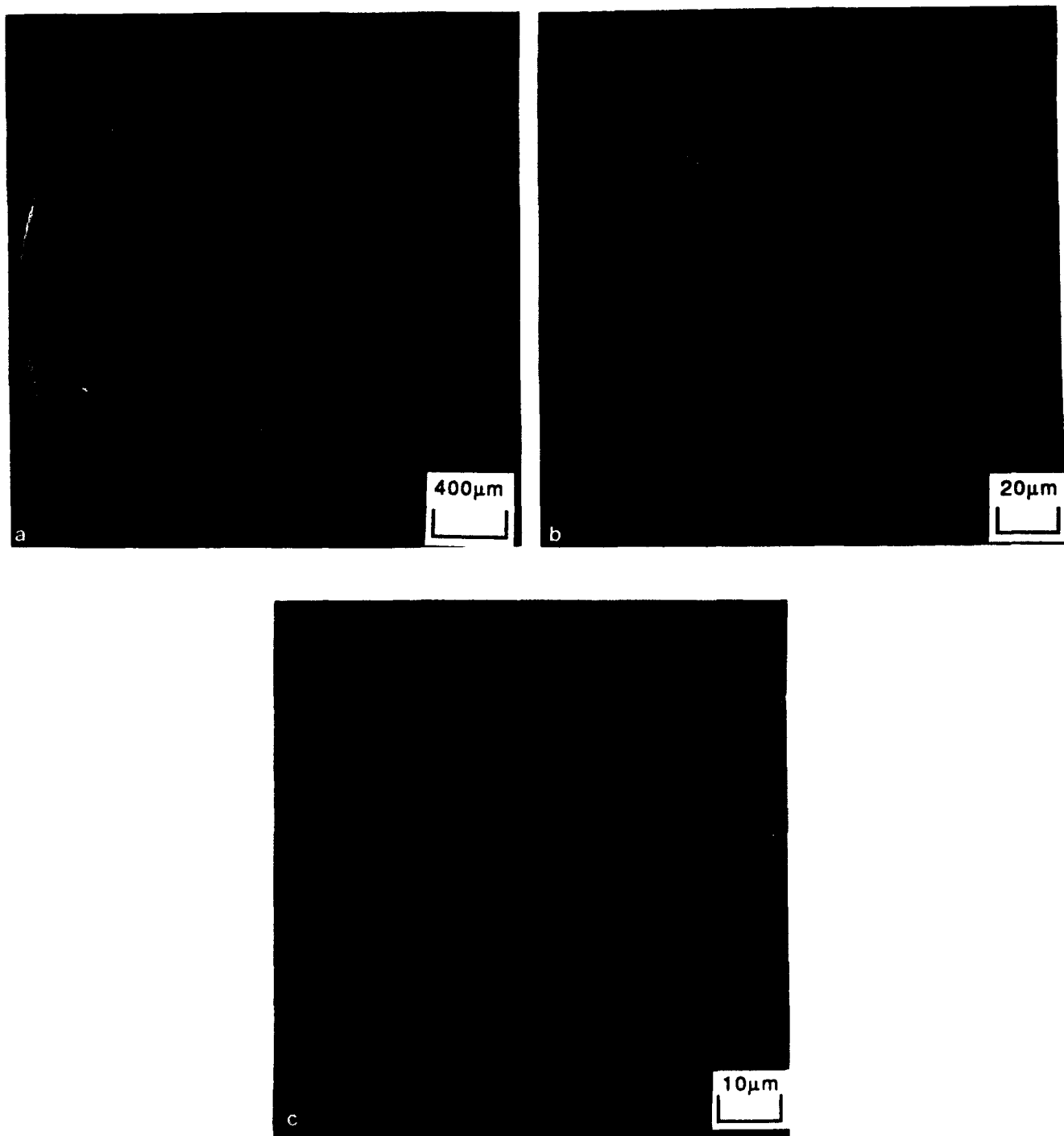


Figure 60. Tensile samples tested at 425°C in air - Heat treatment C.

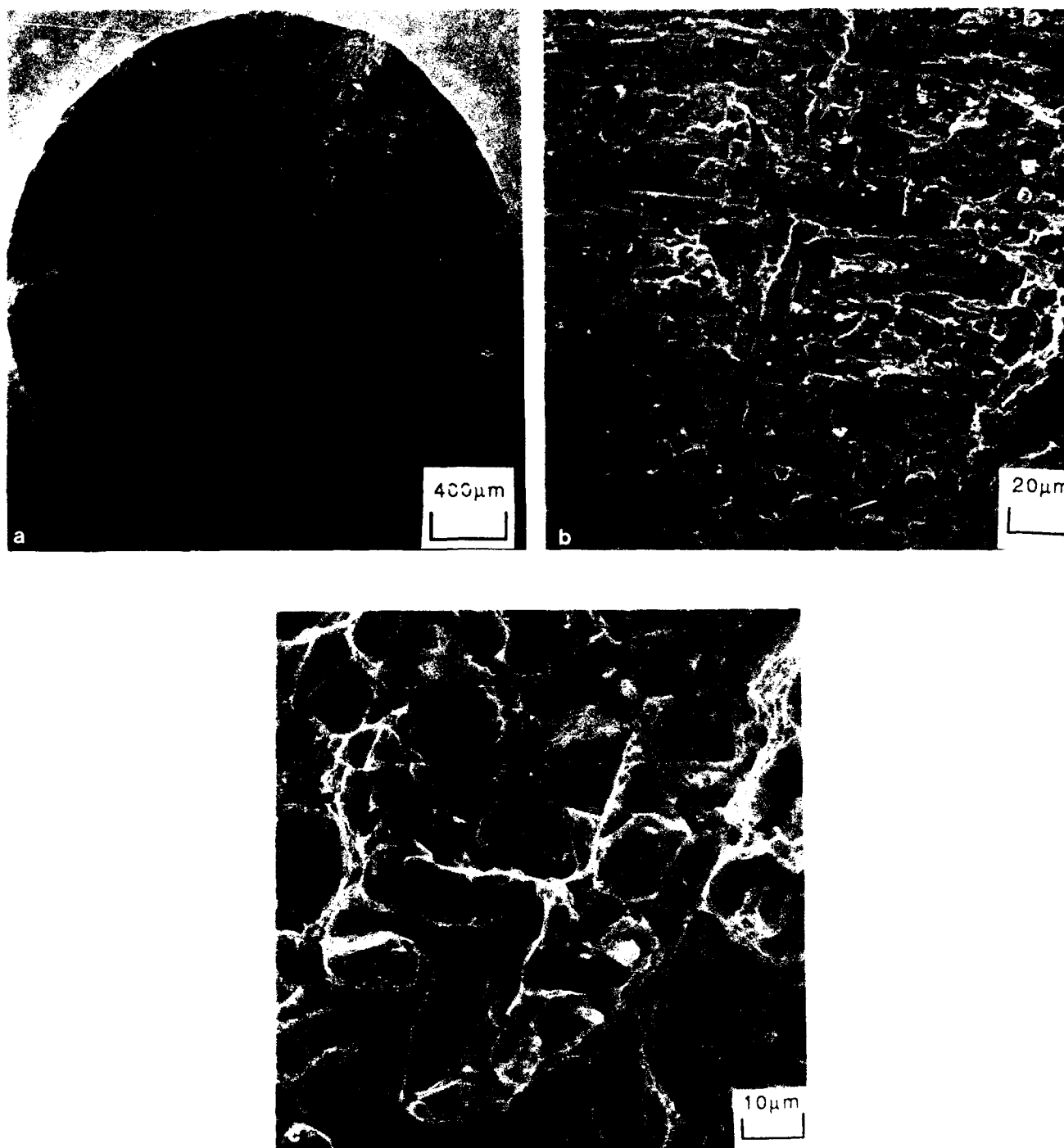


Figure 61. Tensile samples tested at 315°C in air - Heat treatment C.

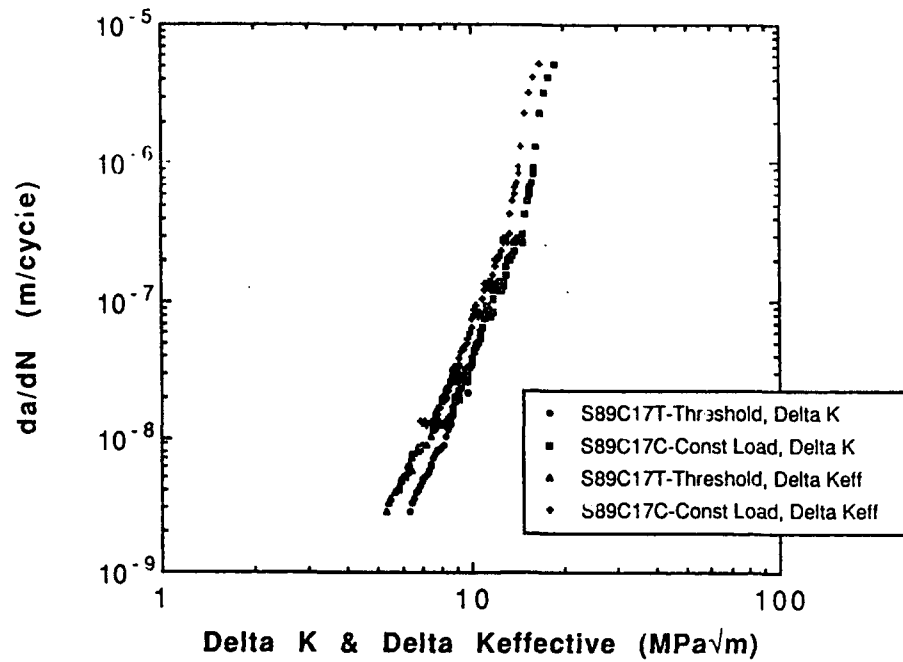


Figure 62. da/dN versus ΔK and da/dN versus $\Delta K_{\text{effective}}$ at test temperature of 25°C.

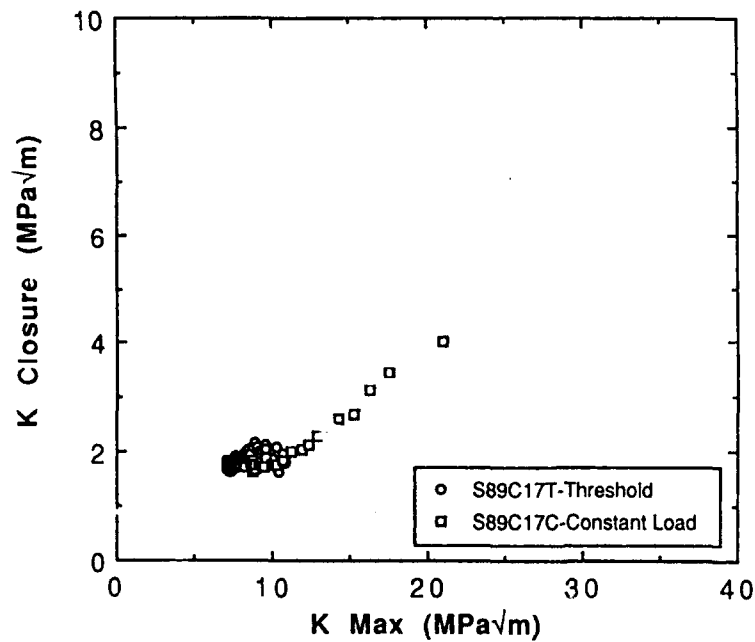


Figure 63. K_{closure} versus K_{max} at test temperature of 25°C in air.

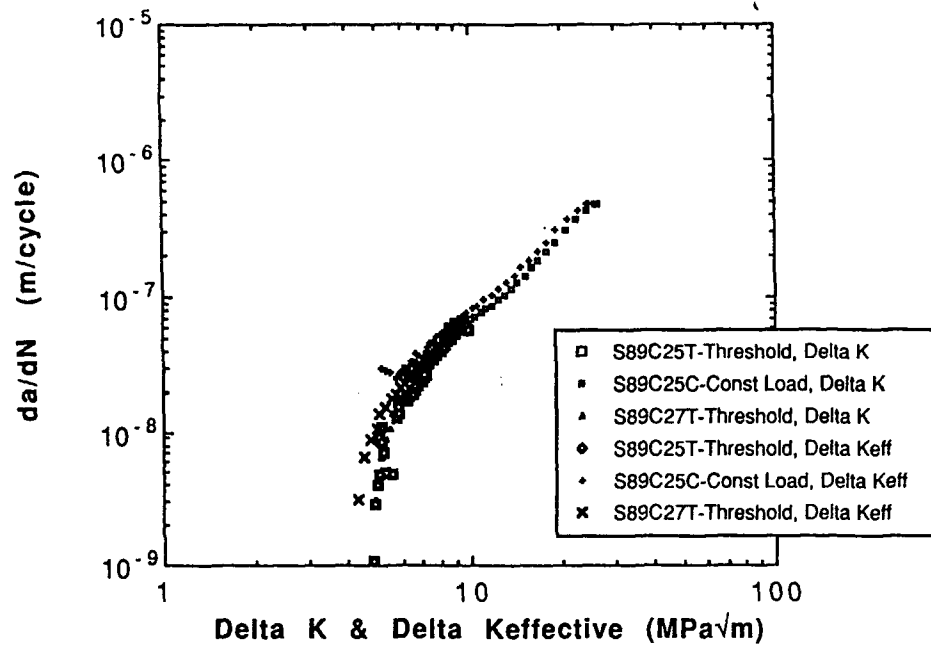


Figure 64. da/dN versus ΔK and da/dN versus $\Delta K_{\text{effective}}$ at test temperature of 425°C in air.

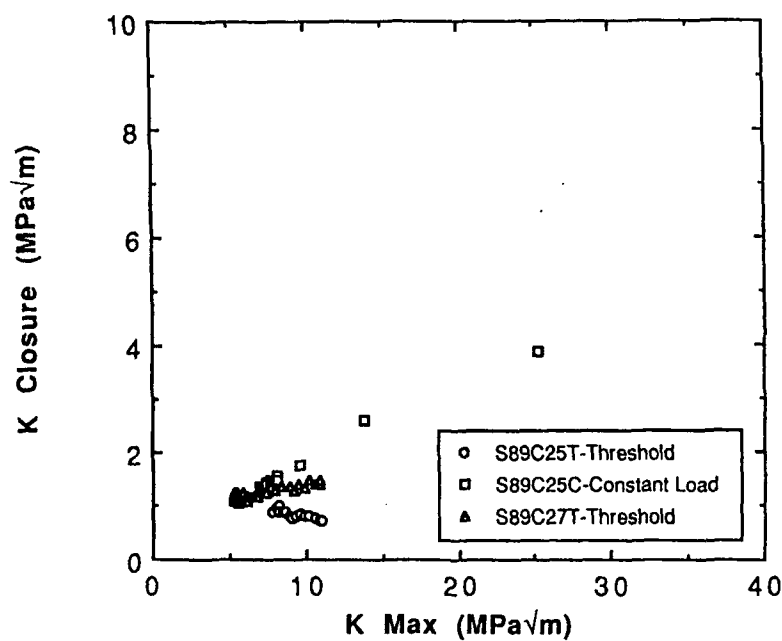


Figure 65. K_{closure} versus K_{max} at test temperature of 425°C in air.

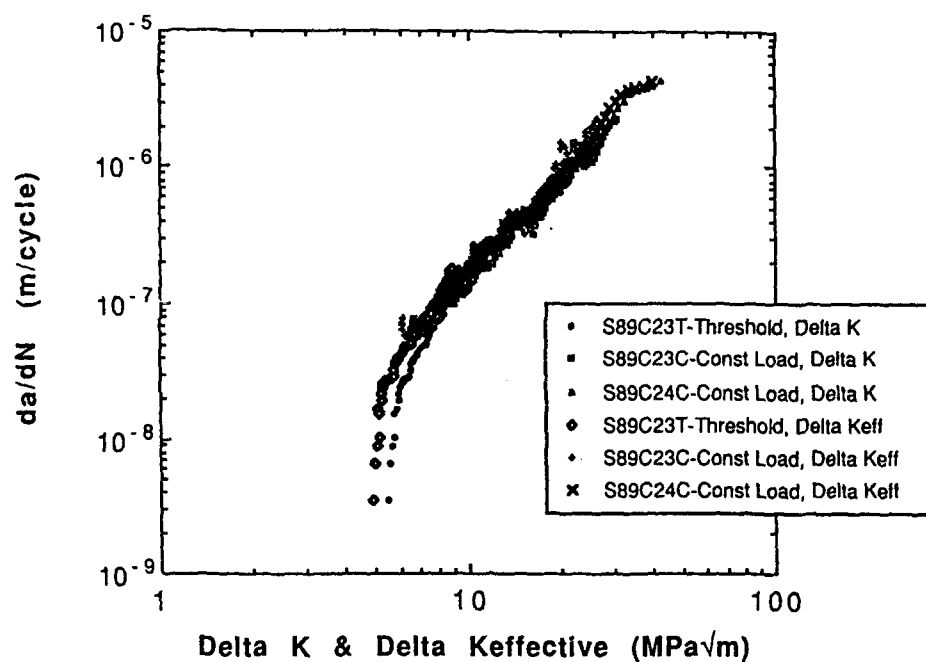


Figure 66. da/dN versus ΔK and da/dN versus $\Delta K_{\text{effective}}$ at test temperature of 540°C in air.

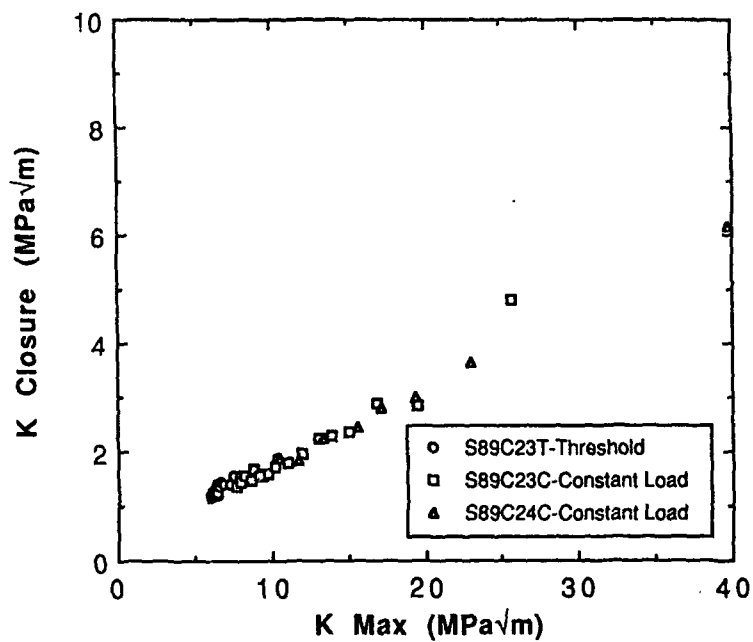


Figure 67. K_{closure} versus K_{max} at test temperature of 540°C in air.

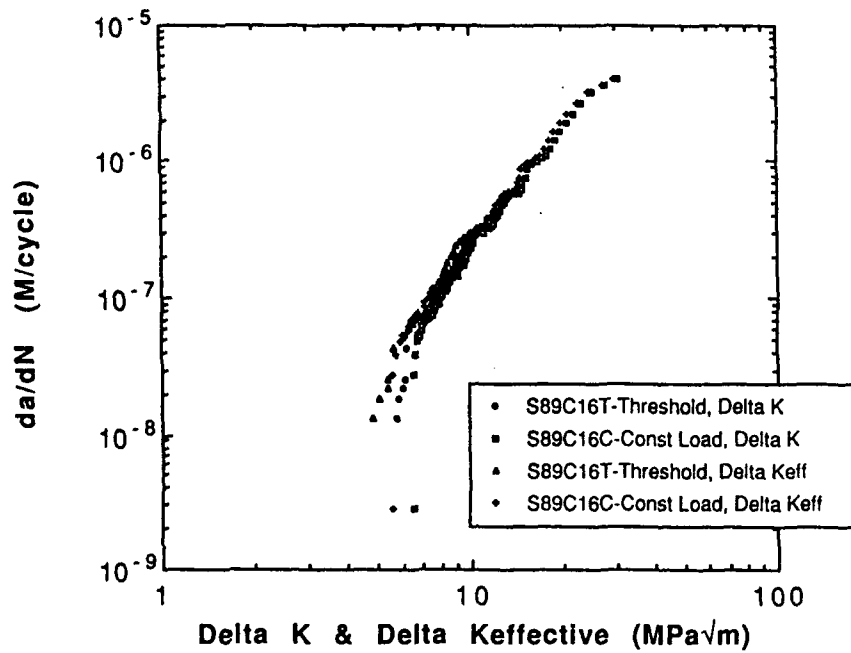


Figure 68. da/dN versus ΔK and da/dN versus $\Delta K_{\text{effective}}$ at test temperature of 650°C in air.

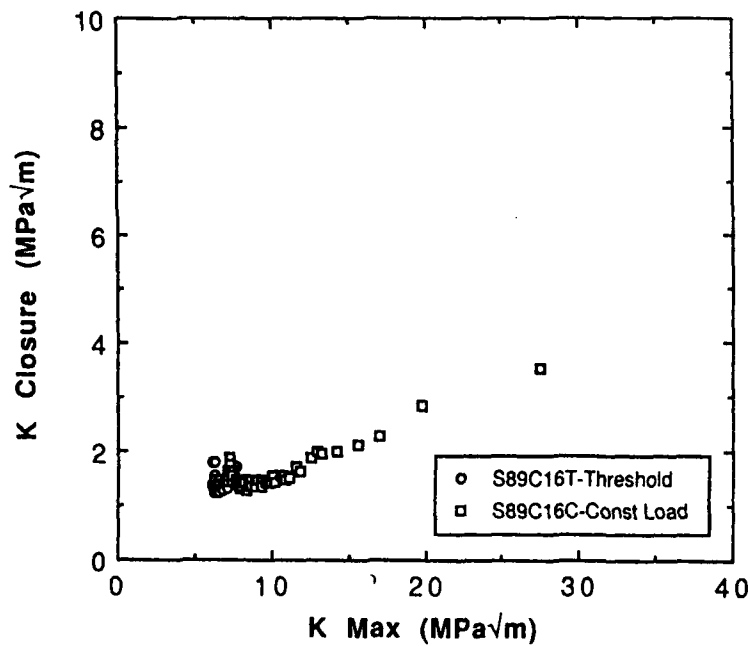


Figure 69. K_{closure} versus K_{max} at test temperature of 650°C in air.

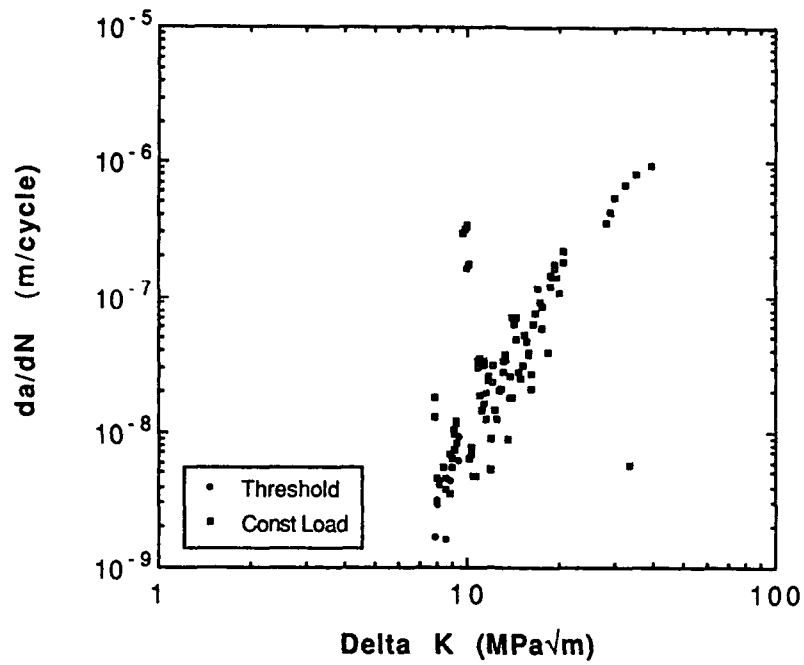


Figure 70. da/dN versus ΔK at test temperature of 540°C in ultra-high vacuum.

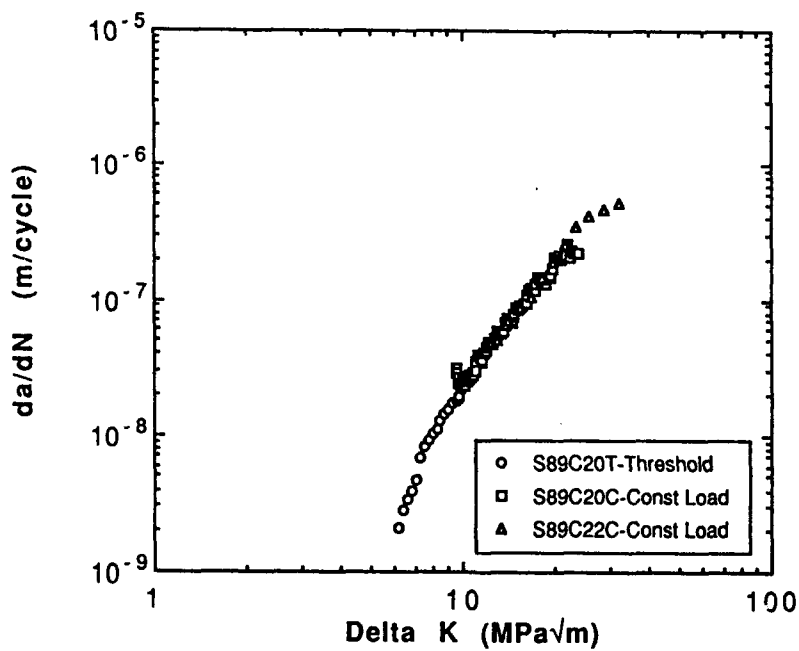


Figure 71. da/dN versus ΔK at test temperature of 650°C in ultra-high vacuum.

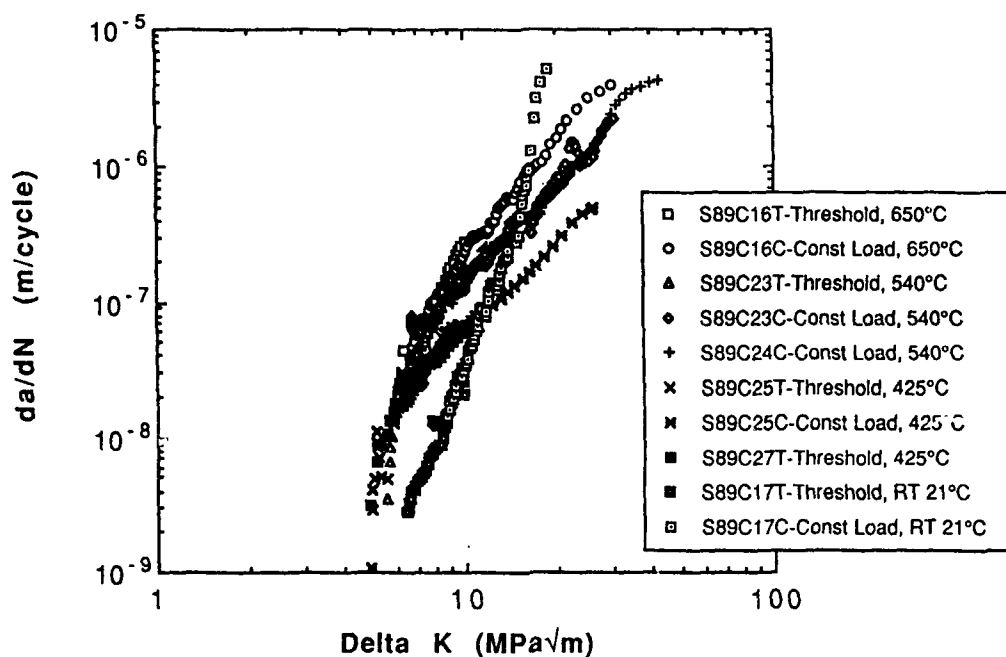


Figure 72. Summary of plots of da/dN versus ΔK for all the tests run in air.

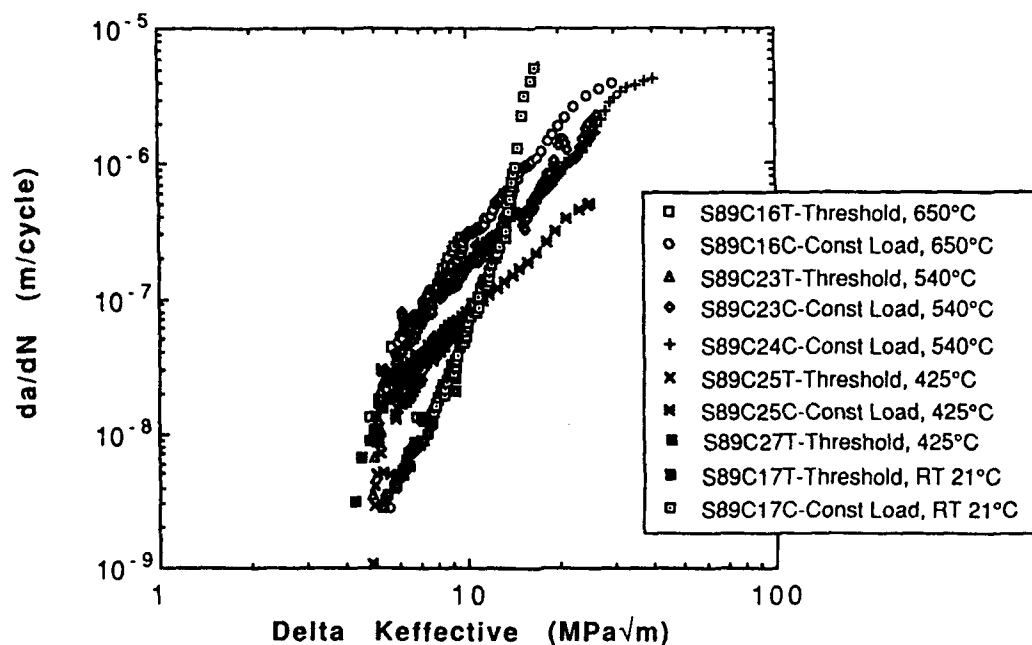


Figure 73. Summary of plots of da/dN versus $\Delta K_{\text{effective}}$ for all the tests run in air.

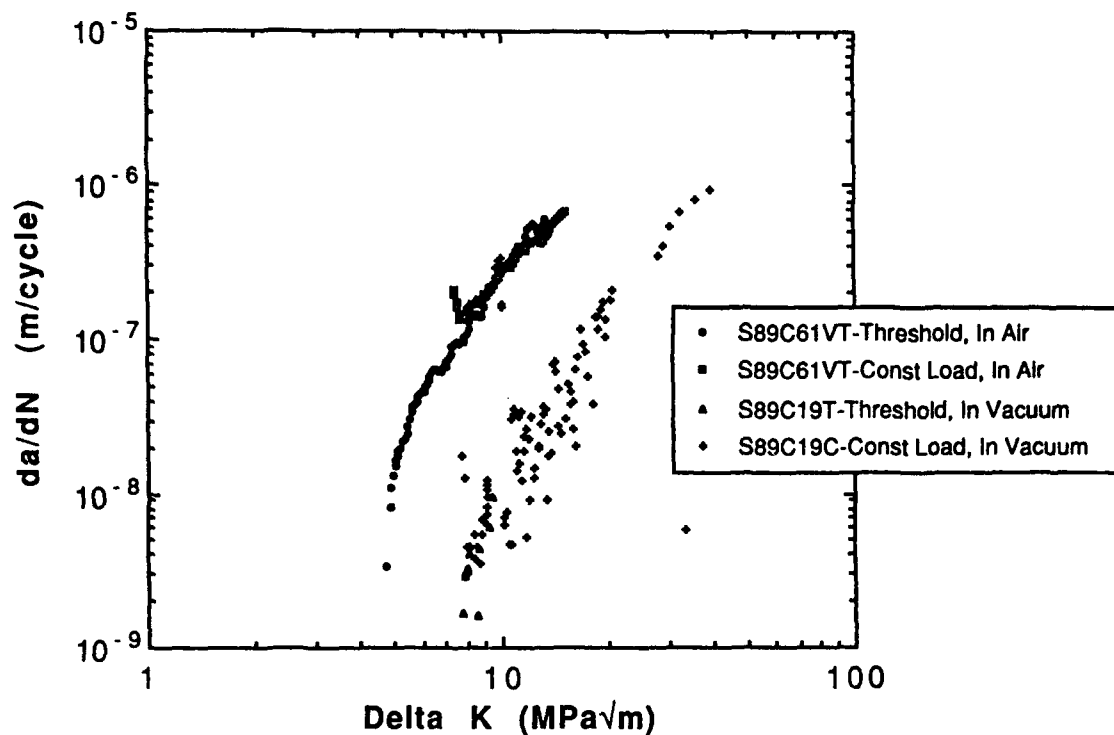


Figure 74. Comparison of crack growth rates at 540°C between air and ultrahigh vacuum environments.

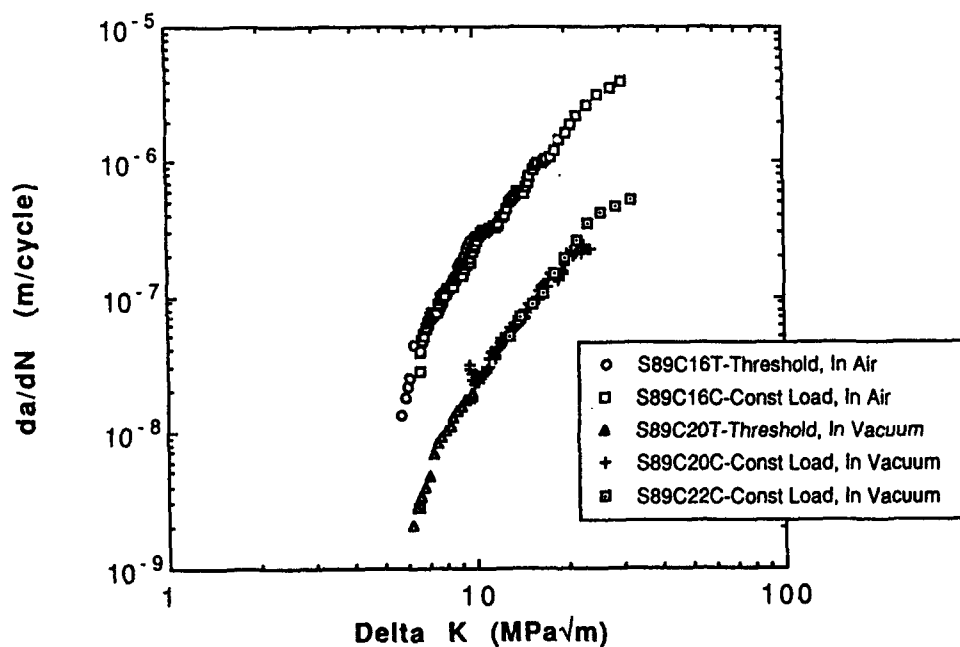


Figure 75. Comparison of crack growth rates at 650°C between air and ultrahigh vacuum environments.

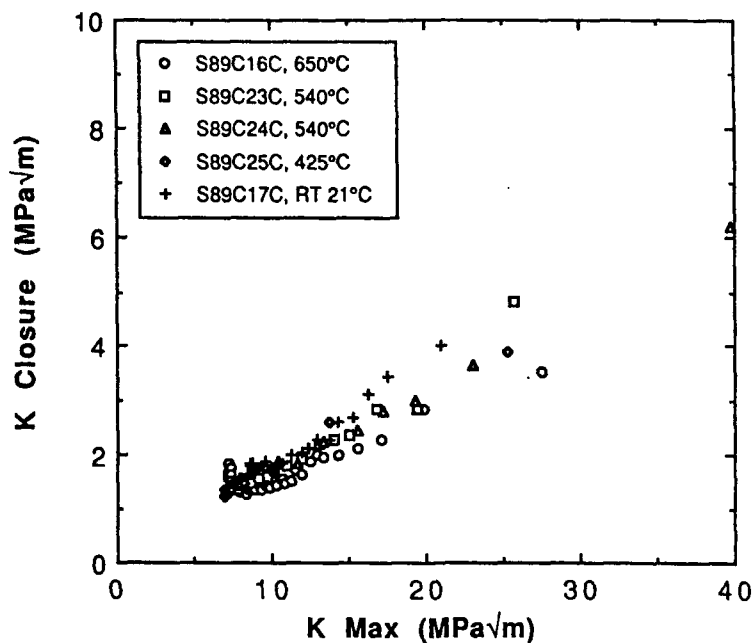


Figure 76. Summary of plots of K_{closure} versus K_{max} showing the effect of test temperature in air - Constant load test condition.

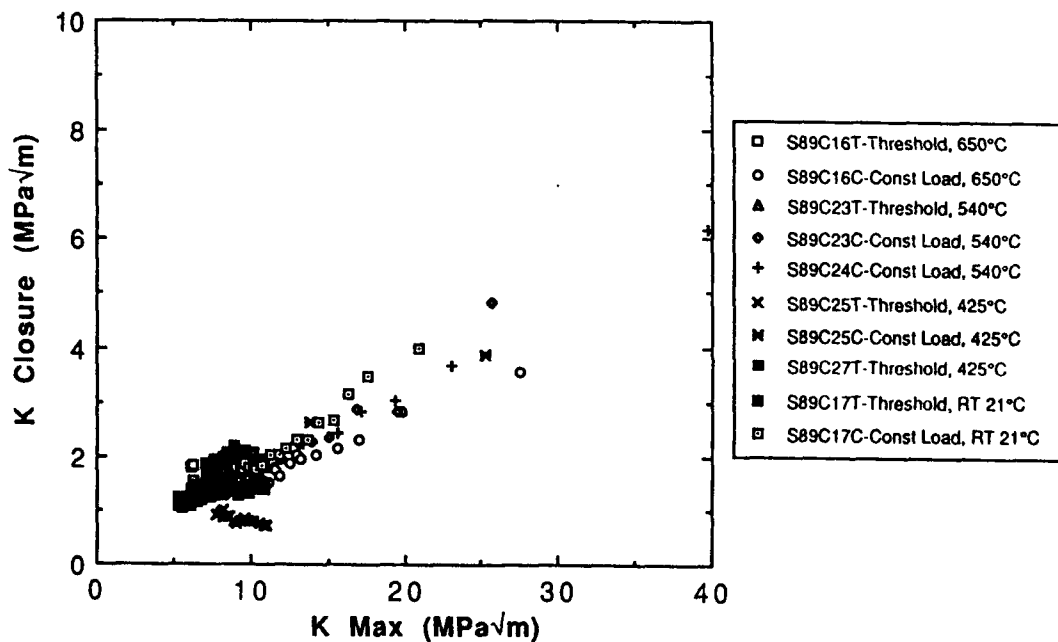


Figure 77. Summary of plots of K_{closure} versus K_{max} showing the effect of test temperature in air - Constant load and threshold test condition.

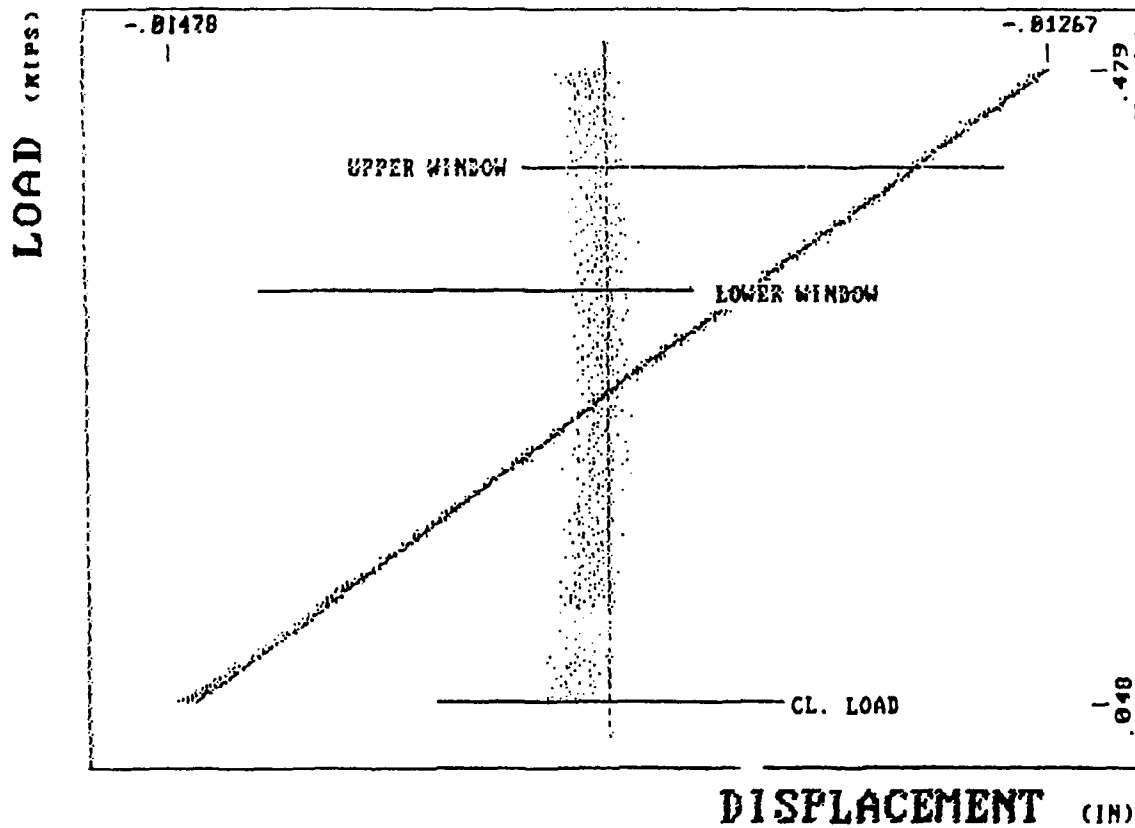


Figure 78. Load-displacement of a typical fatigue crack growth test conducted in ultra-high vacuum showing the lack of closure effects.

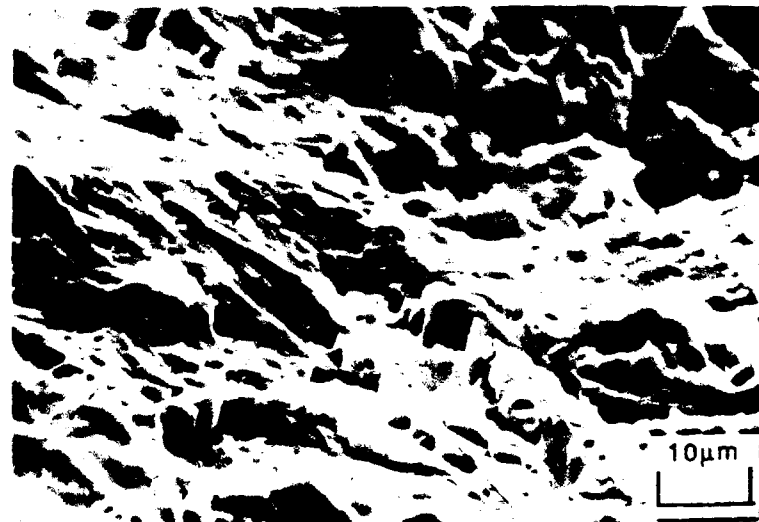
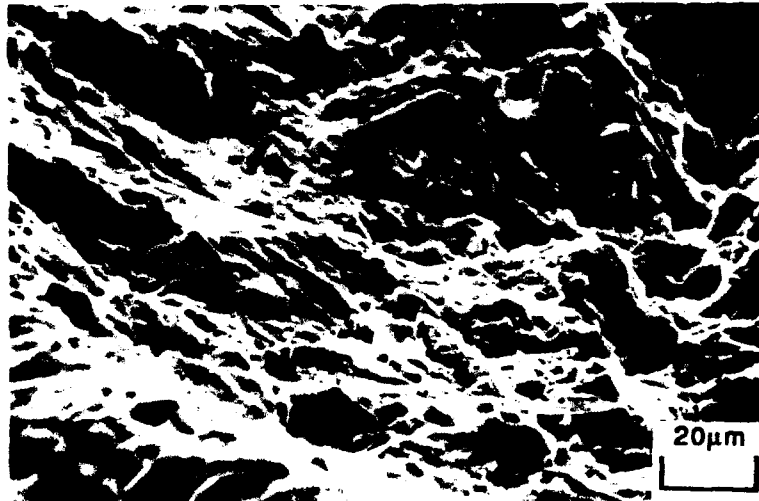
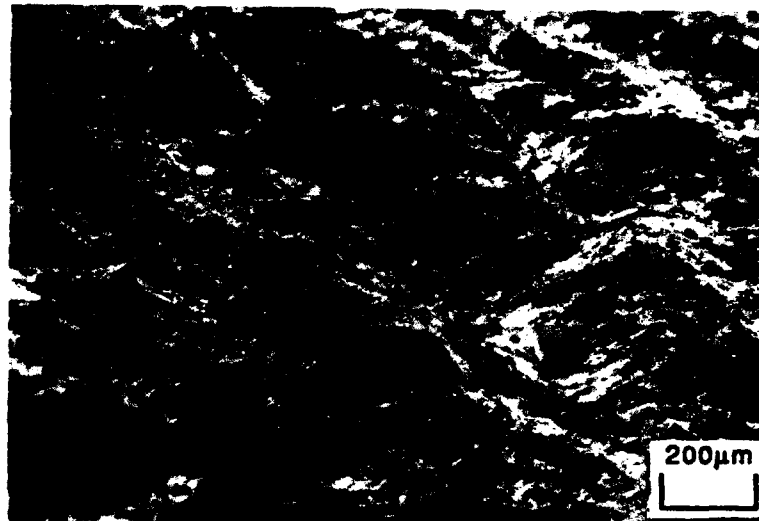


Figure 79. SEM fractographs of fatigue crack growth specimen at 25°C in air.

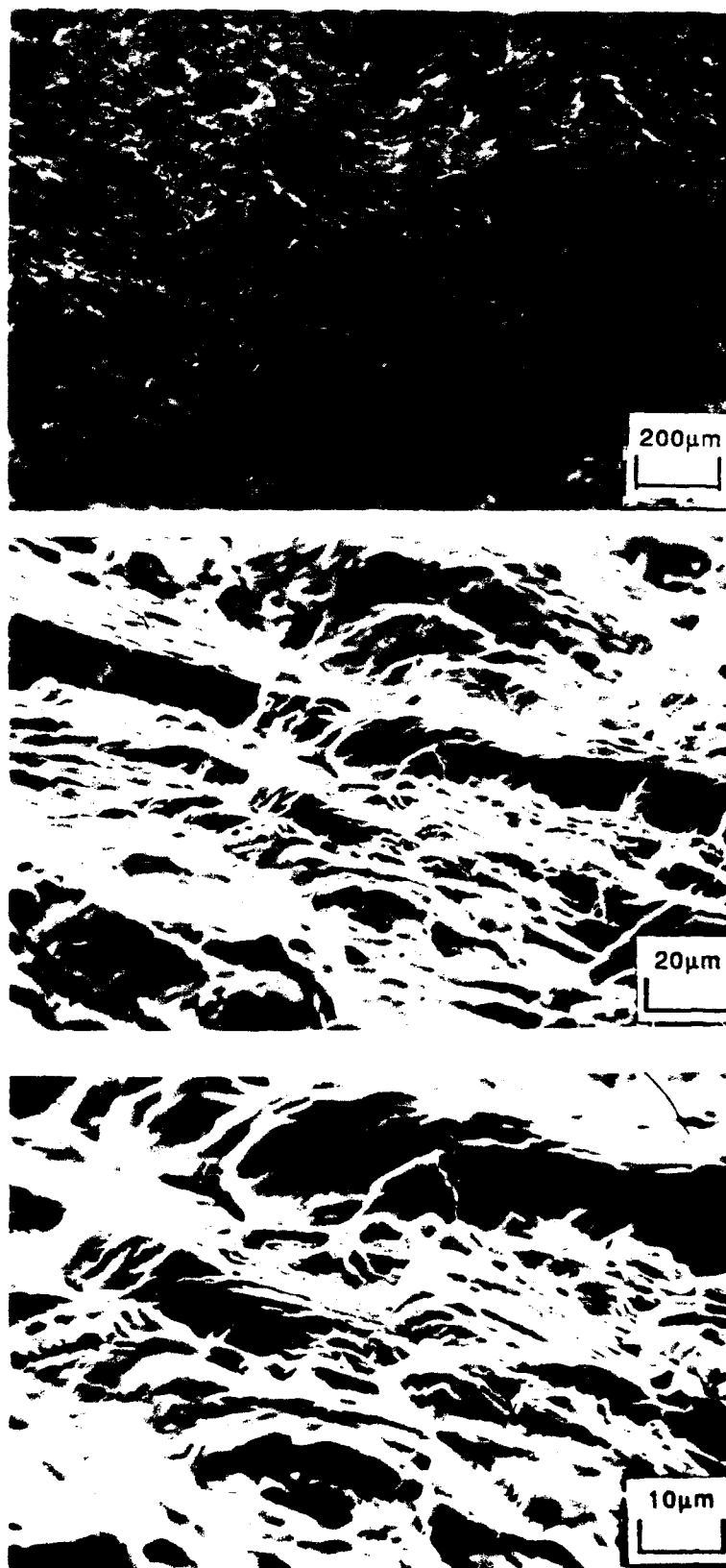


Figure 80. SEM fractographs of fatigue crack growth specimen at 425°C in air.

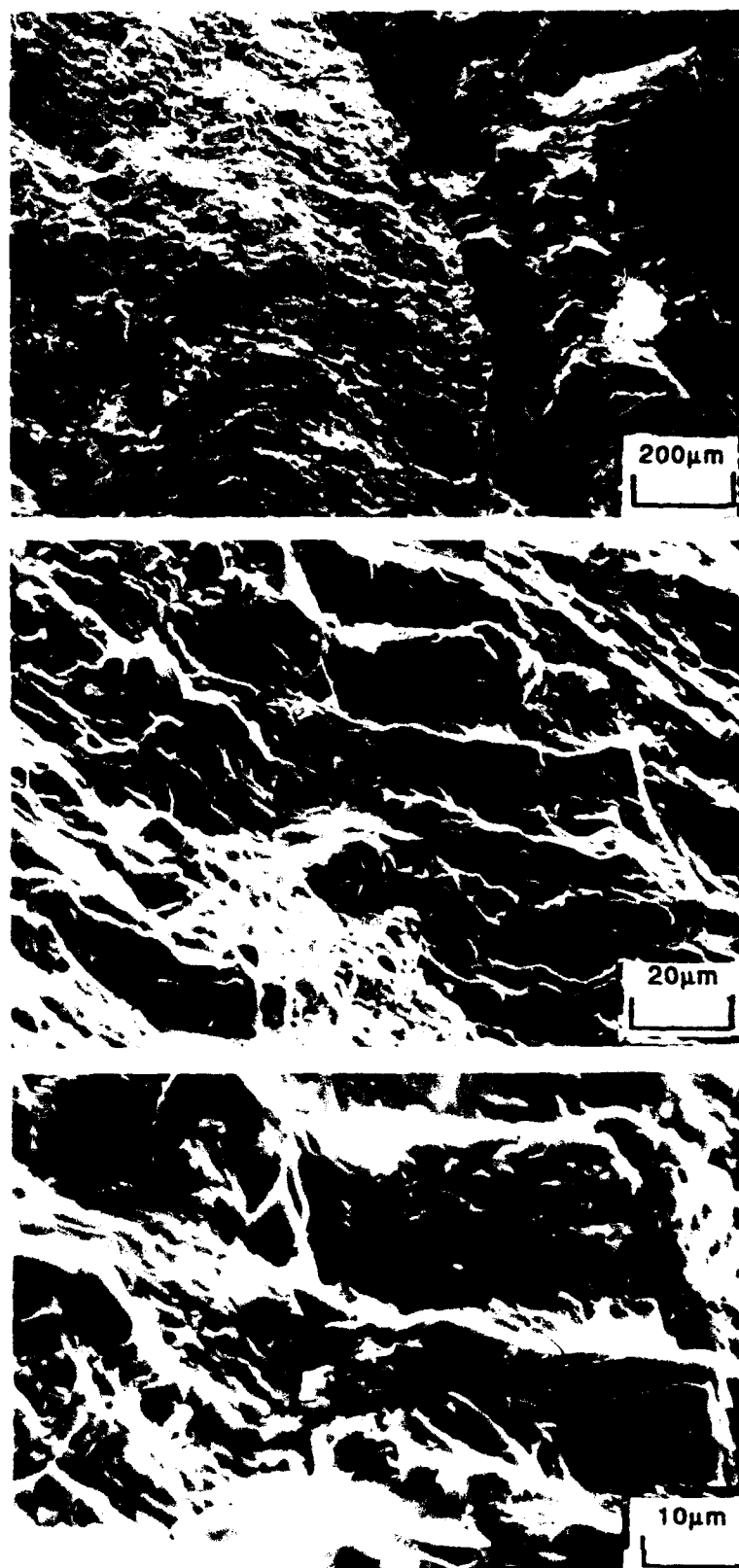


Figure 81. SEM fractographs of fatigue crack growth specimen at 540°C in air.

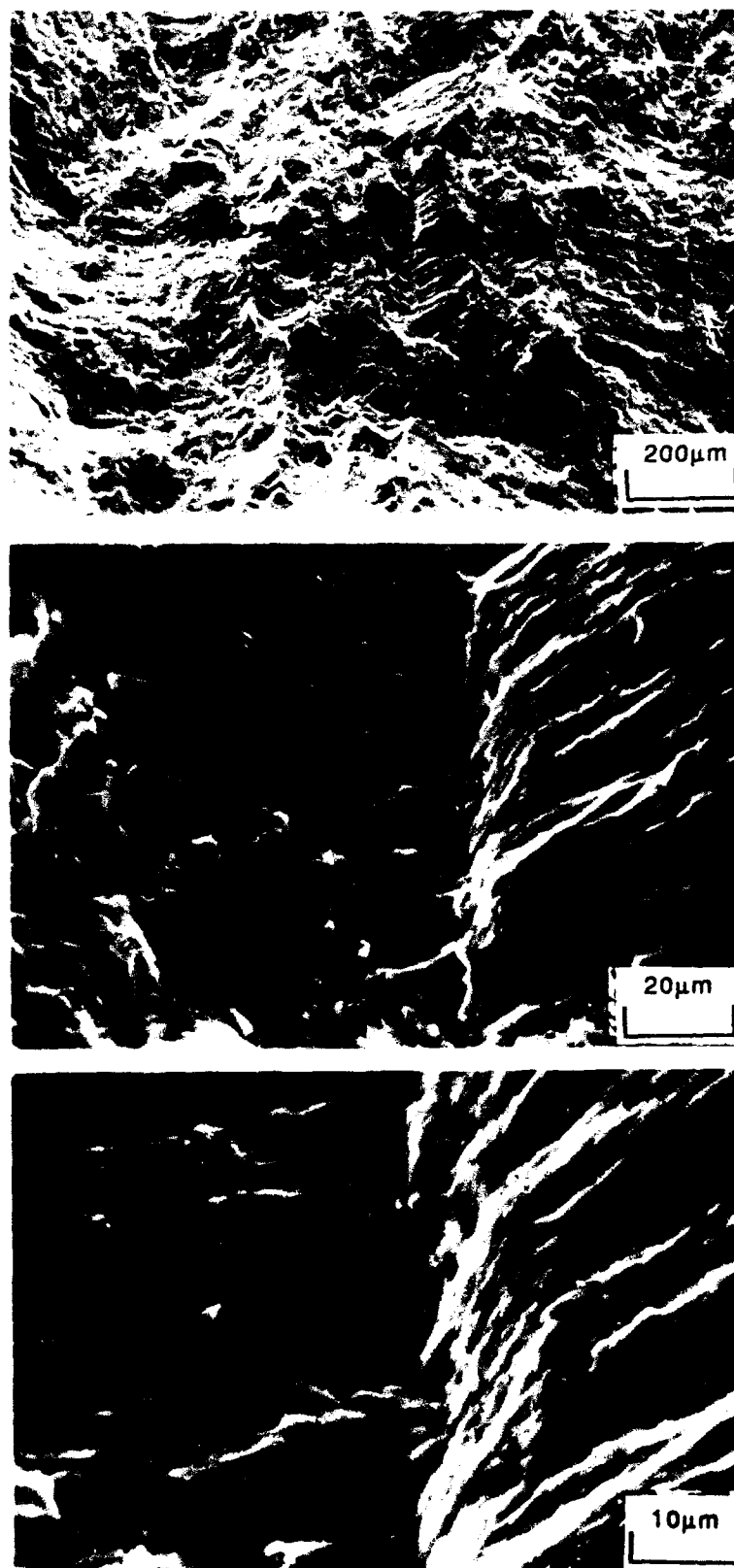


Figure 82. SEM fractographs of fatigue crack growth specimen at 650°C in air.

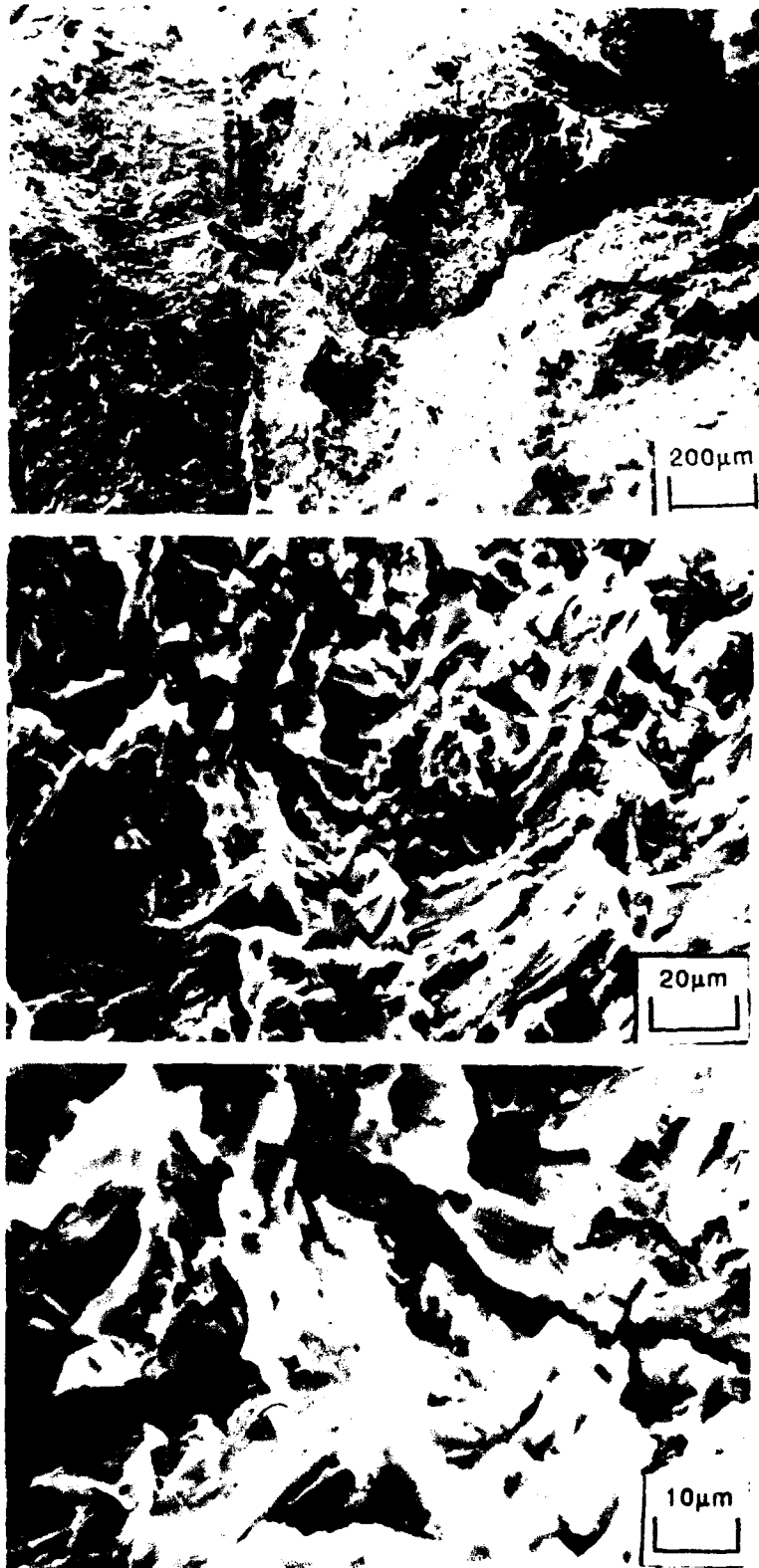


Figure 83. SEM fractographs of fatigue crack growth specimen at 650°C in ultra-high vacuum.

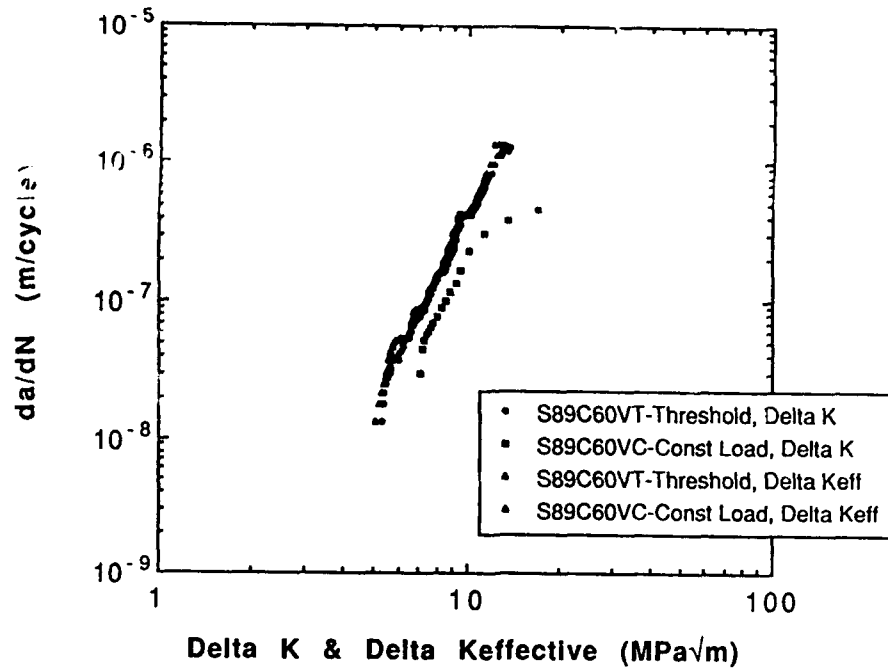


Figure 84. da/dN versus ΔK and $\Delta K_{\text{effective}}$ for fatigue crack growth test done at 650°C - specimen S89C60V

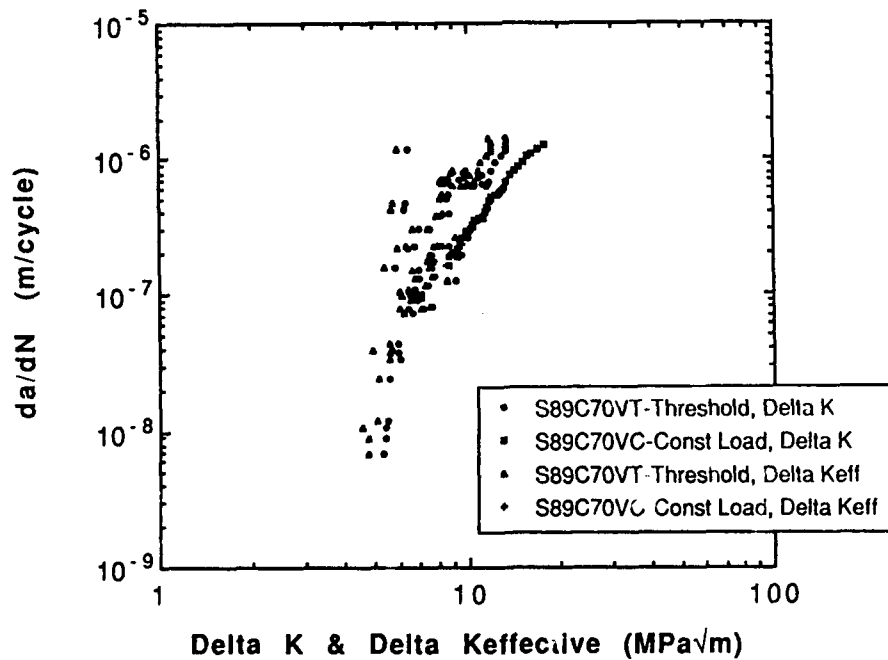


Figure 85. da/dN versus ΔK and $\Delta K_{\text{effective}}$ for fatigue crack growth test done at 650°C - specimen S89C70V

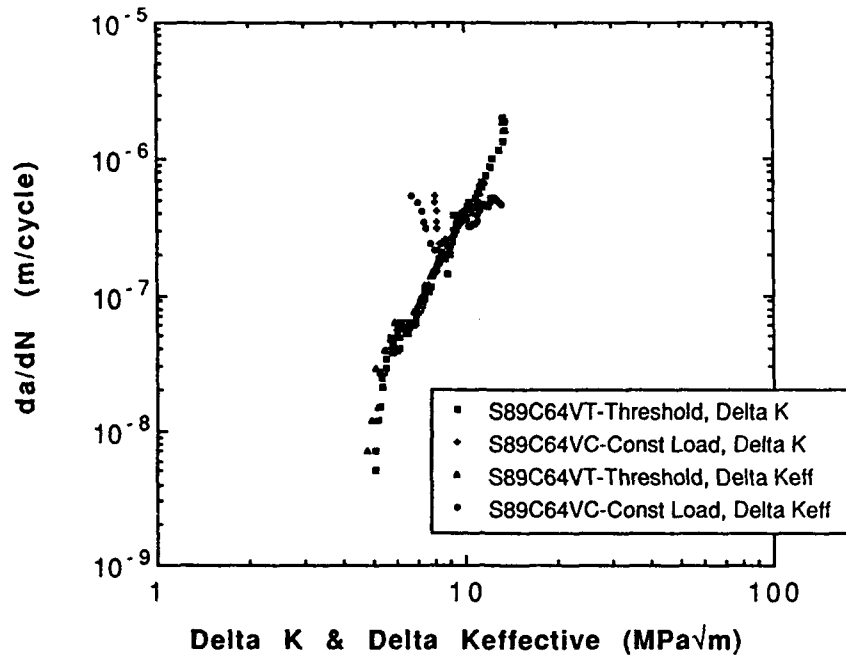


Figure 86. da/dN versus ΔK and $\Delta K_{\text{effective}}$ for fatigue crack growth test done at 650°C - specimen S89C64V

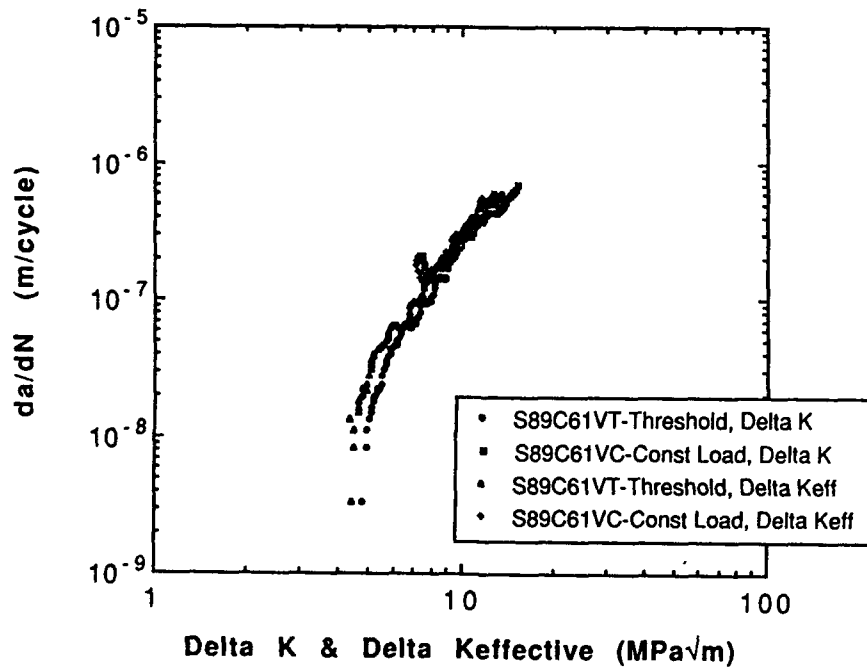


Figure 87. da/dN versus ΔK and $\Delta K_{\text{effective}}$ for fatigue crack growth test done at 540°C - specimen S89C61V

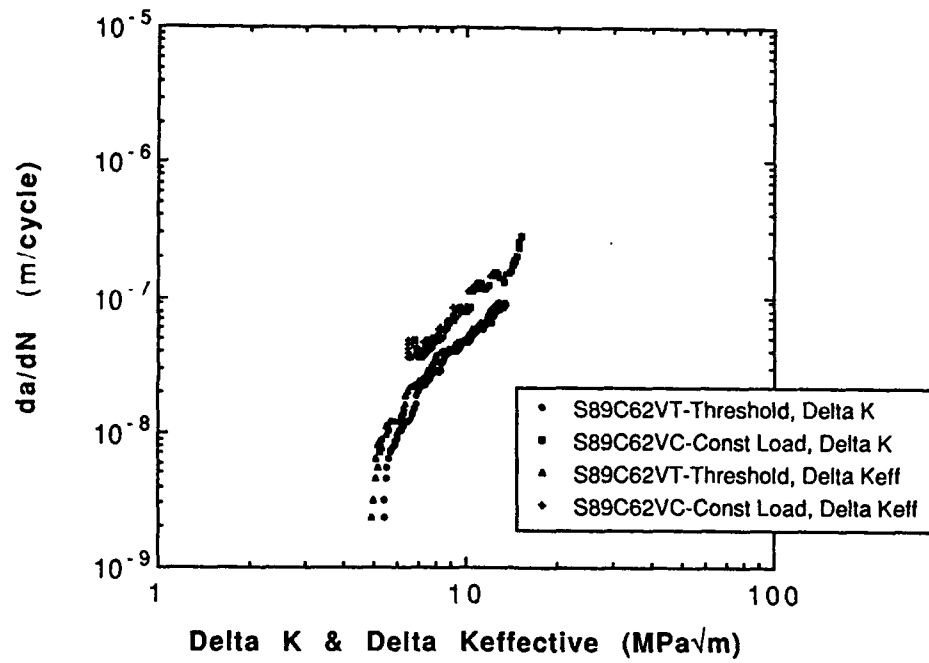


Figure 88. da/dN versus ΔK and $\Delta K_{\text{effective}}$ for fatigue crack growth test done at 425°C - specimen S89C62V

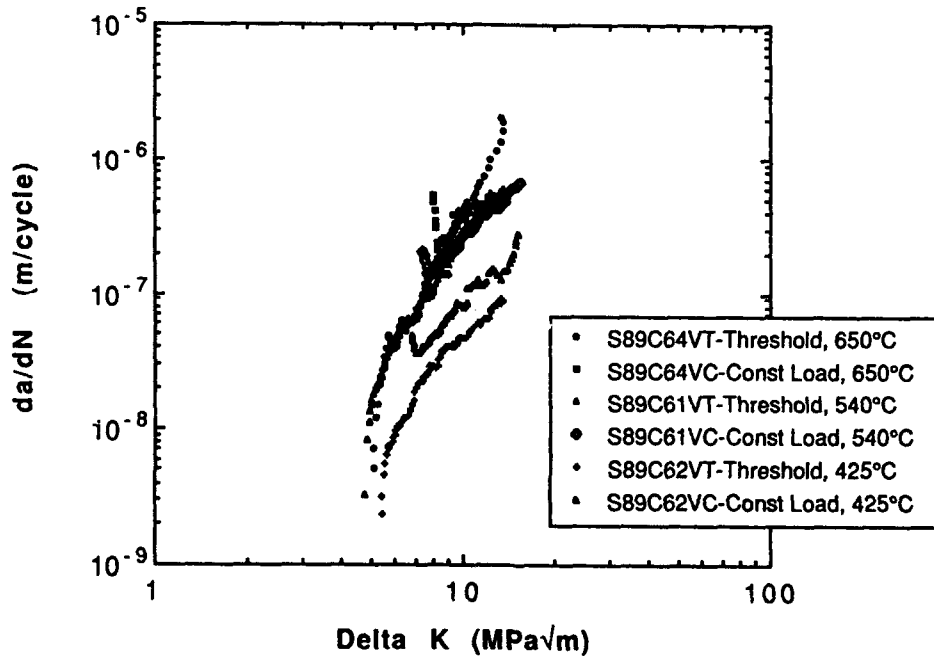


Figure 89. Summary of all the crack growth data for the transverse orientation.

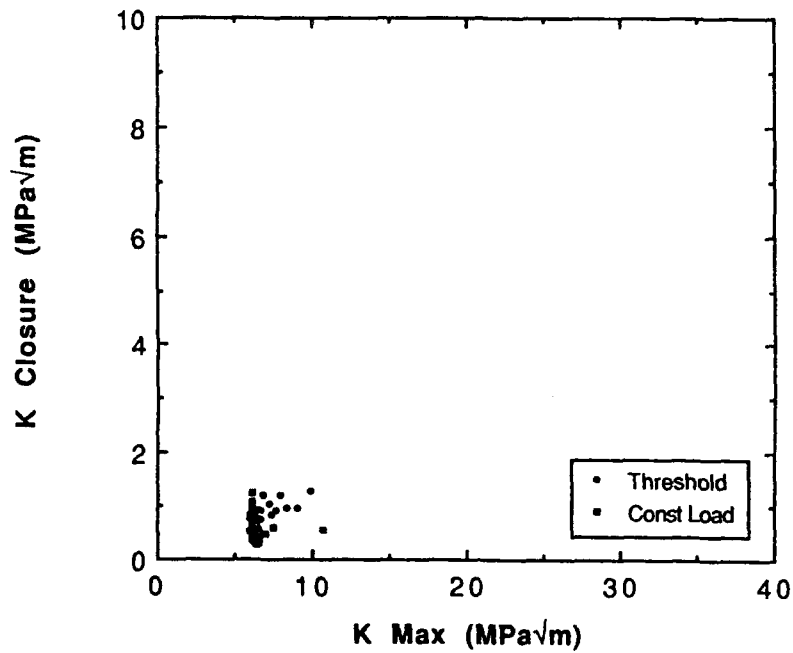


Figure 90. K_{closure} versus K_{max} for fatigue crack growth test done at 650°C for specimen with transverse orientation - Specimen S89C60V

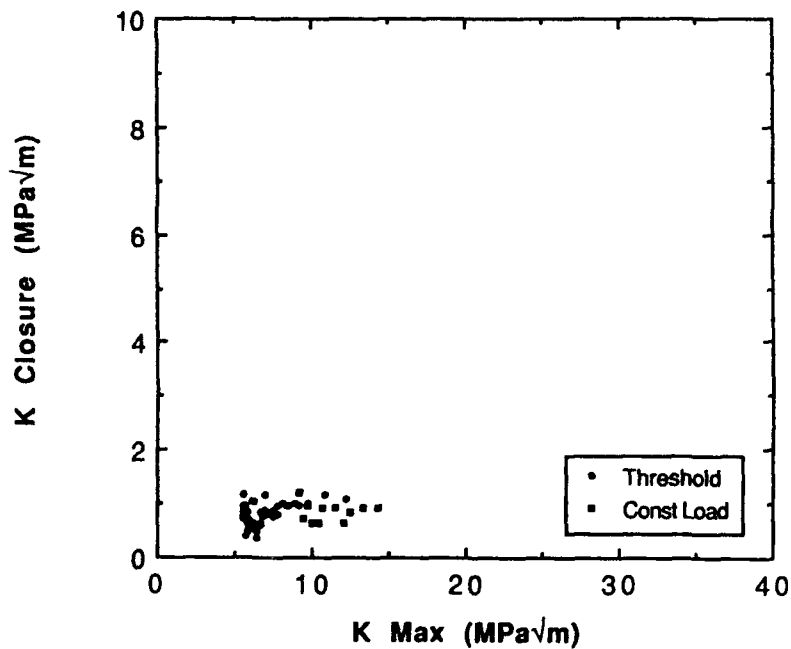


Figure 91. K_{closure} versus K_{max} for fatigue crack growth test done at 650°C for specimen with transverse orientation - Specimen S89C64V

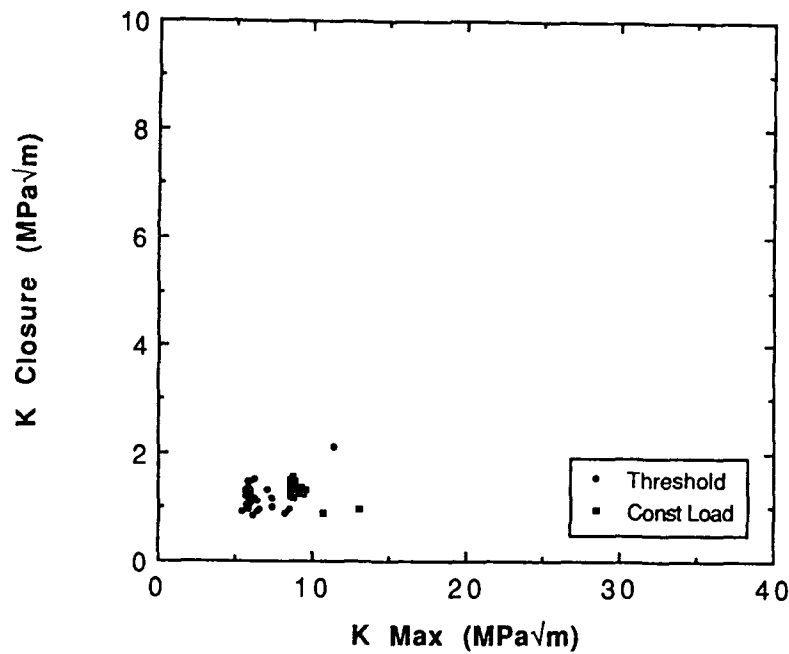


Figure 92. $K_{closure}$ versus K_{max} for fatigue crack growth test done at 650°C for specimen with transverse orientation - Specimen S89C70V

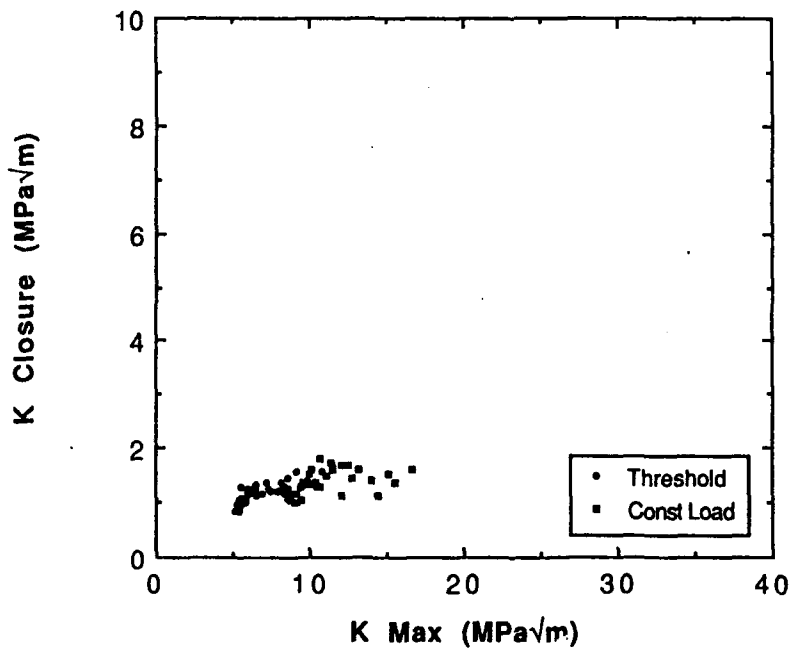


Figure 93. $K_{closure}$ versus K_{max} for fatigue crack growth test done at 540°C for specimen with transverse orientation - Specimen S89C61V

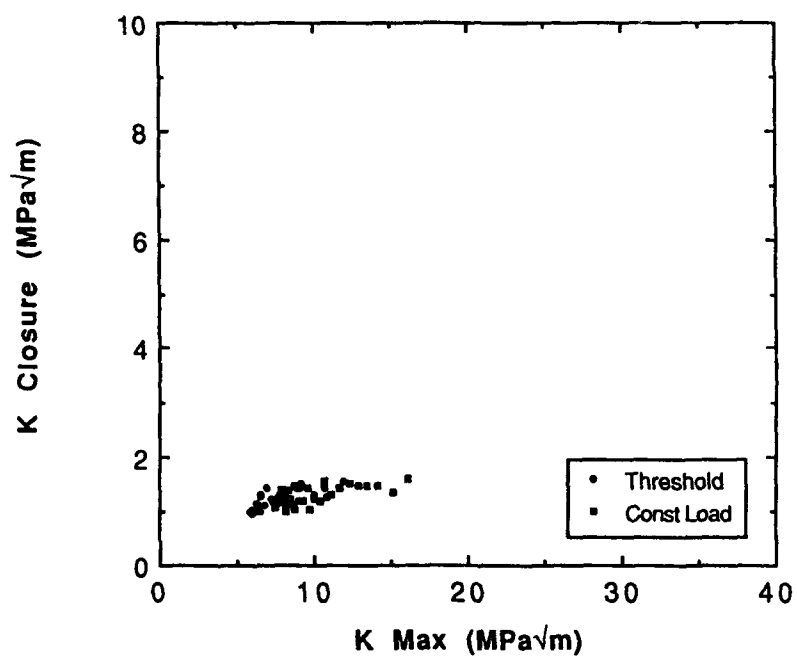


Figure 94. K_{closure} versus K_{max} for fatigue crack growth test done at 425°C for specimen with transverse orientation - Specimen S89C62V

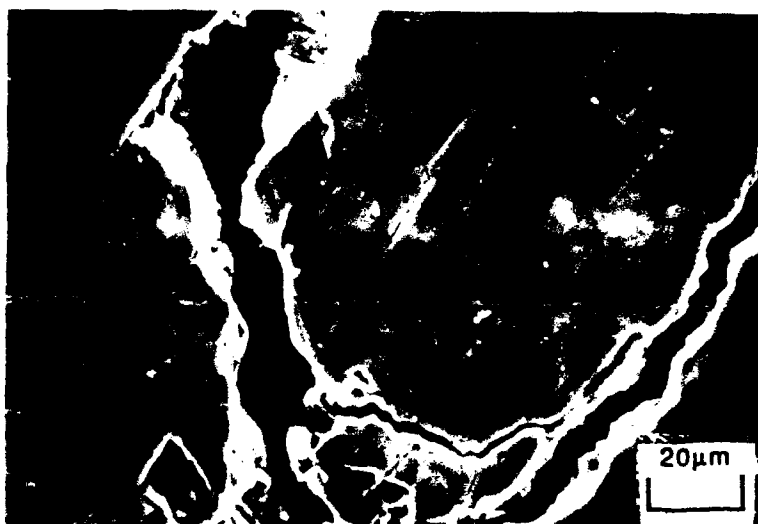
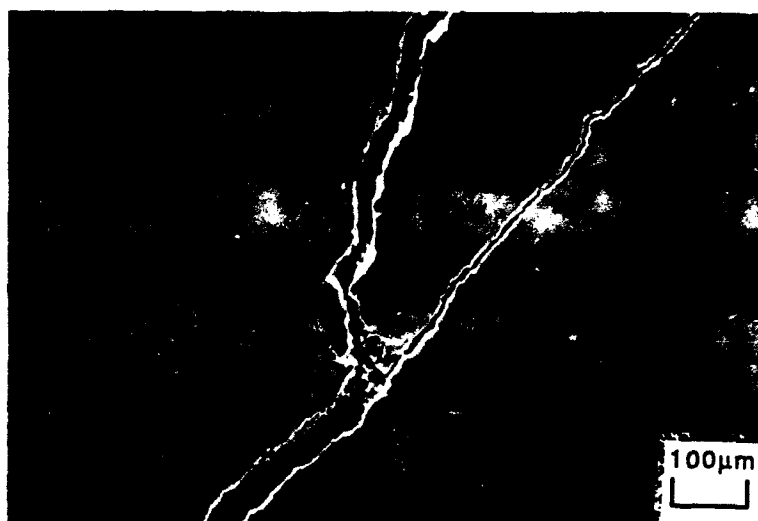


Figure 95. Typical examples of crack branching seen in the fatigue crack growth tests conducted at constant maximum stress-intensity, but at different frequencies - Specimen #S89C65

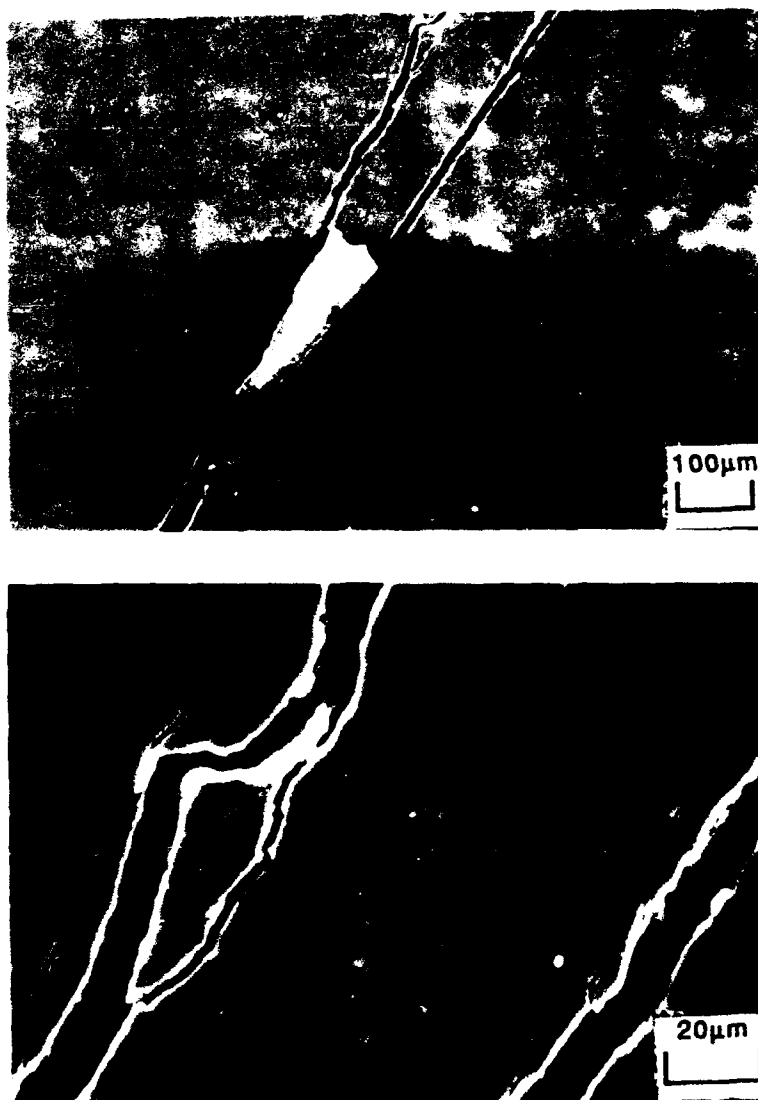


Figure 96. Typical examples of crack branching seen in the fatigue crack growth tests conducted at constant maximum stress-intensity, but at different frequencies - Specimen #S89C18



Figure 97. Typical examples of crack branching seen in the fatigue crack growth tests conducted at constant maximum stress-intensity, but at different frequencies - Specimen #S89C21

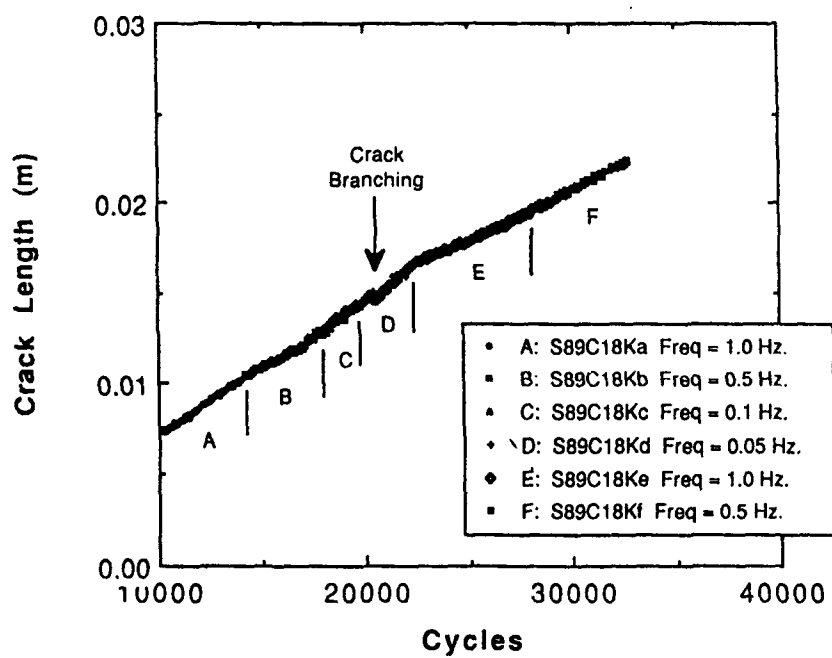


Figure 98. Typical crack length versus cycles for a fatigue crack growth test conducted at constant maximum stress-intensity, but at different frequencies - specimen #S89C18

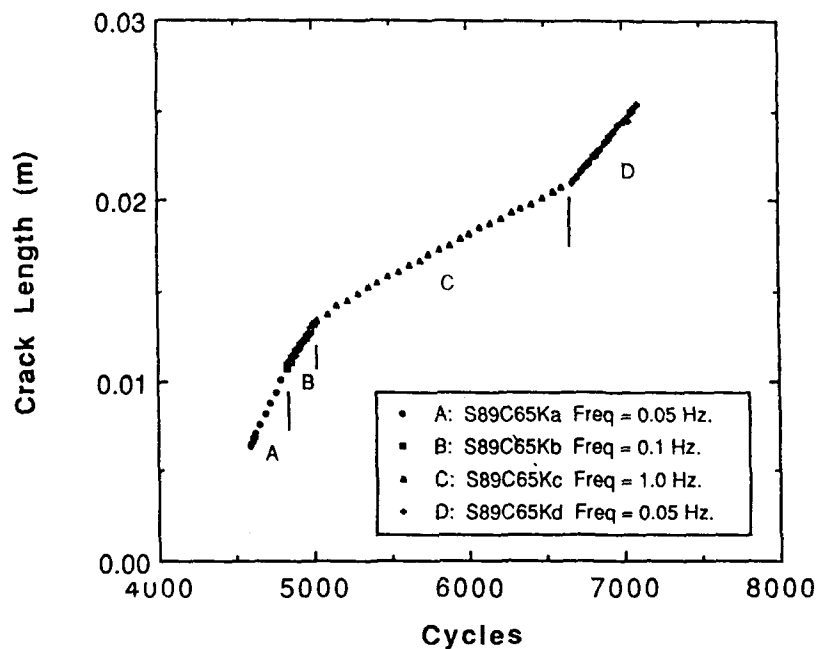


Figure 99. Typical crack length versus cycles for a fatigue crack growth test conducted at constant maximum stress-intensity, but at different frequencies - specimen #S89C65

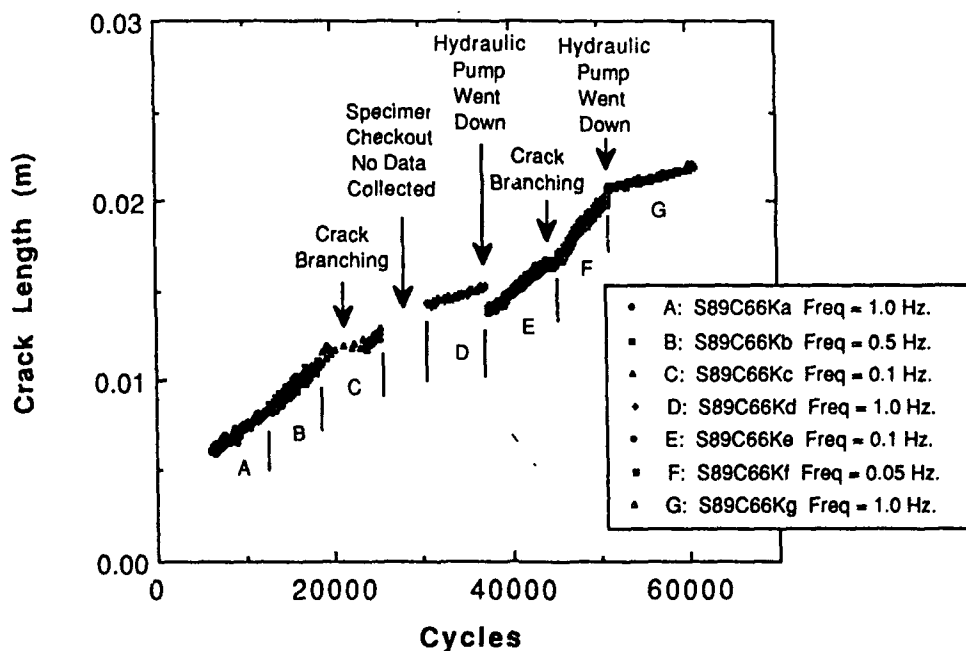


Figure 100. Typical crack length versus cycles for a fatigue crack growth test conducted at constant maximum stress-intensity, but at different frequencies - specimen #S89C66

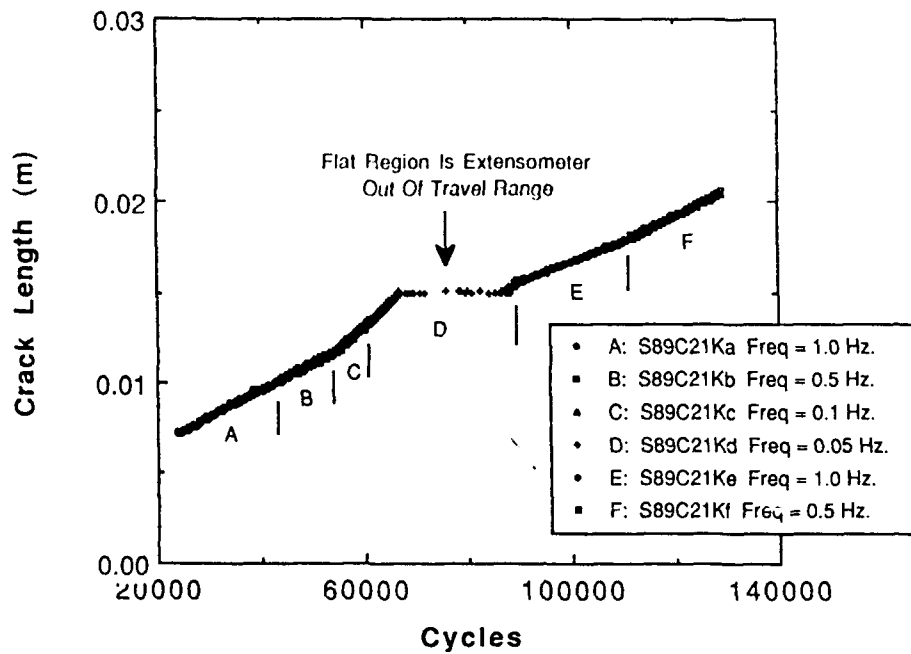


Figure 101. Typical crack length versus cycles for a fatigue crack growth test conducted at constant maximum stress intensity, but at different frequencies - specimen #S89C21

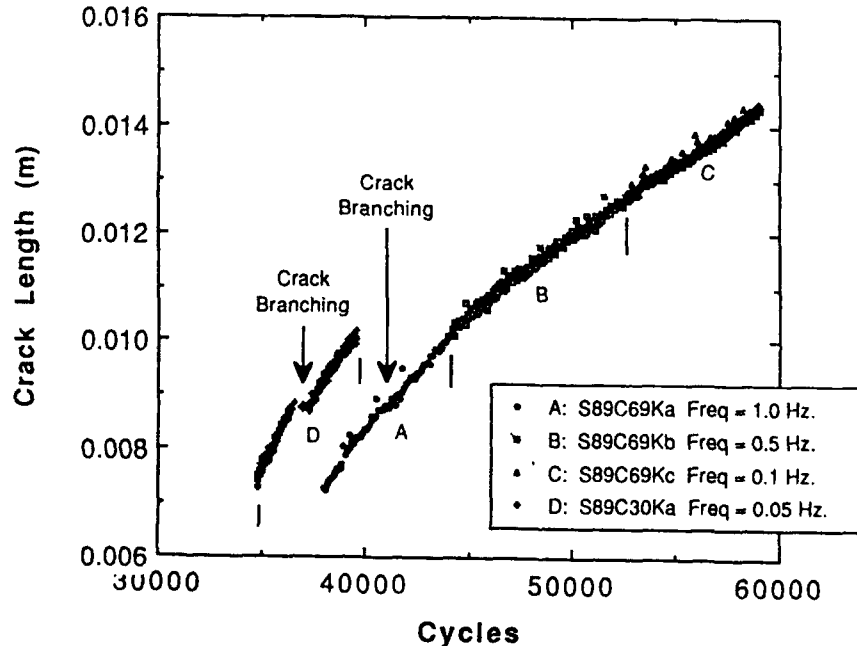


Figure 102. Typical crack length versus cycles for a fatigue crack growth test conducted at constant maximum stress intensity, but at different frequencies - specimen #S89C69&30

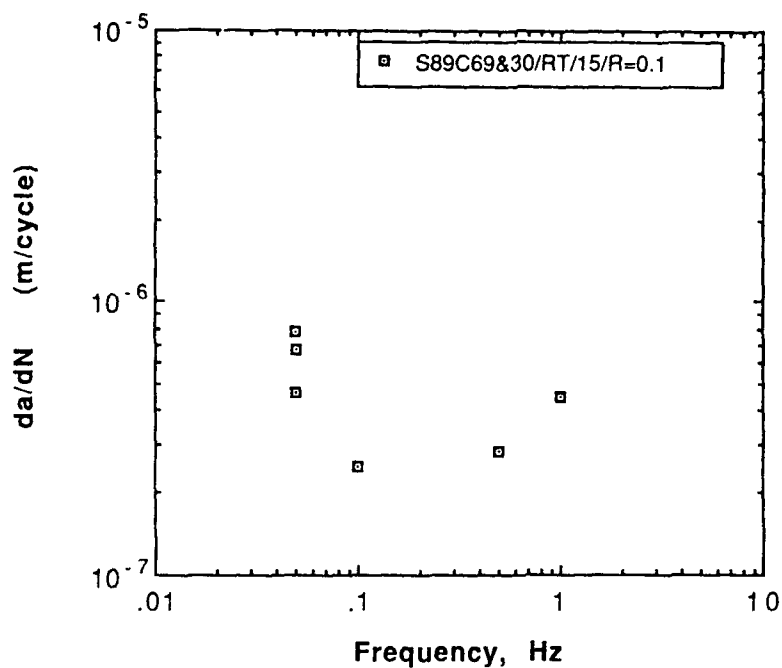


Figure 103. da/dN versus frequency for test conducted at room temperature, K_{max} of 15 $MPa\sqrt{m}$, and R-ratio of 0.1.

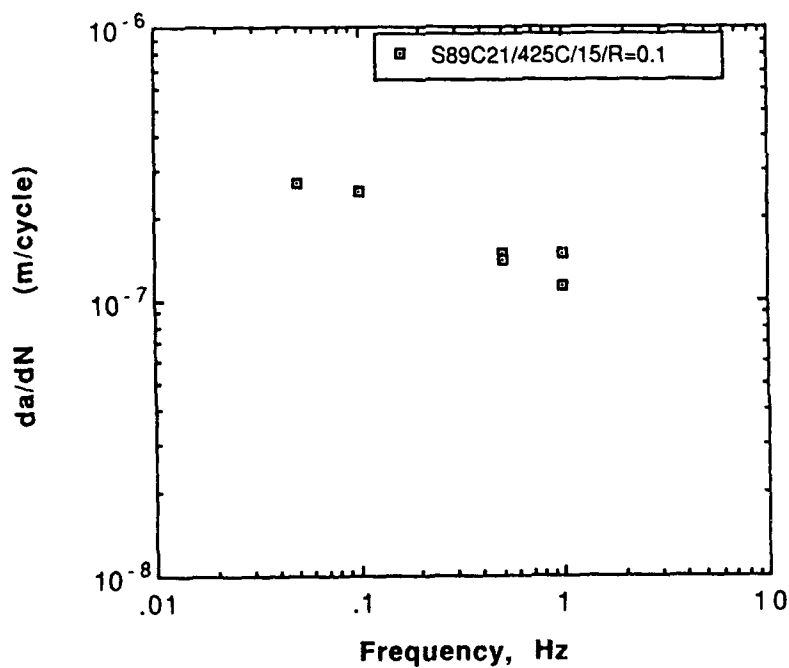


Figure 104. da/dN versus frequency for test conducted at a temperature of 425°C, K_{max} of 15 $MPa\sqrt{m}$, and R-ratio of 0.1.

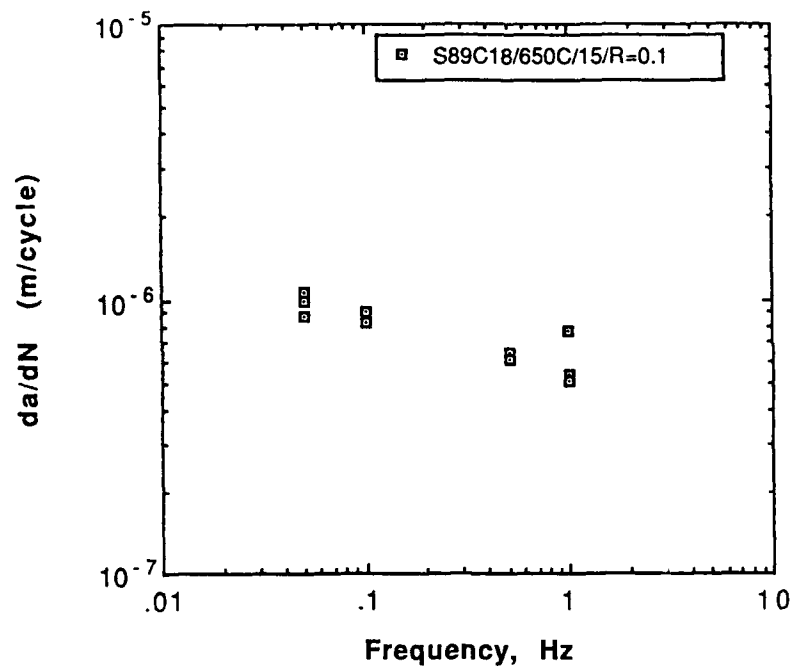


Figure 105. da/dN versus frequency for test conducted at a temperature of 650°C, K_{max} of 15 MPa \sqrt{m} , and R-ratio of 0.1.

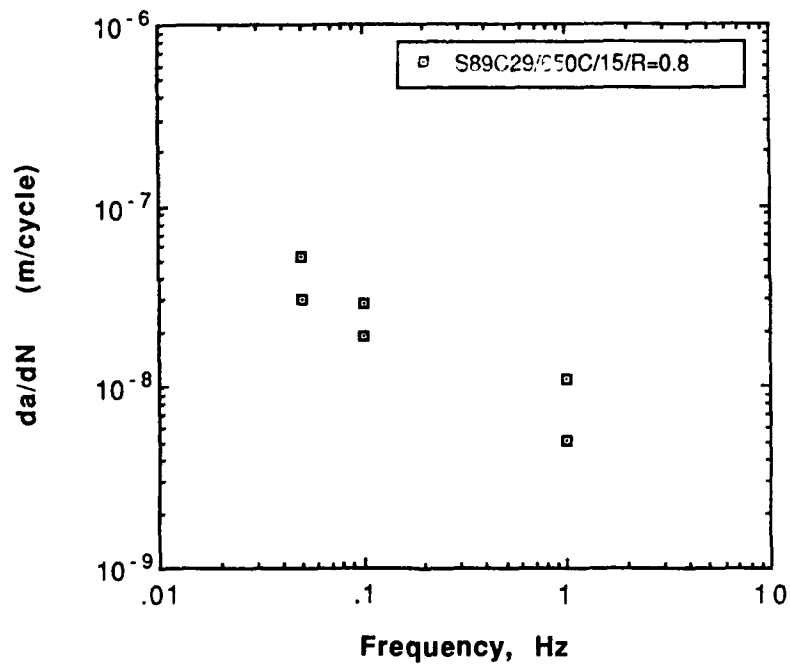


Figure 106. da/dN versus frequency for test conducted at a temperature of 650°C, K_{max} of 15 MPa \sqrt{m} , and R-ratio of 0.8.

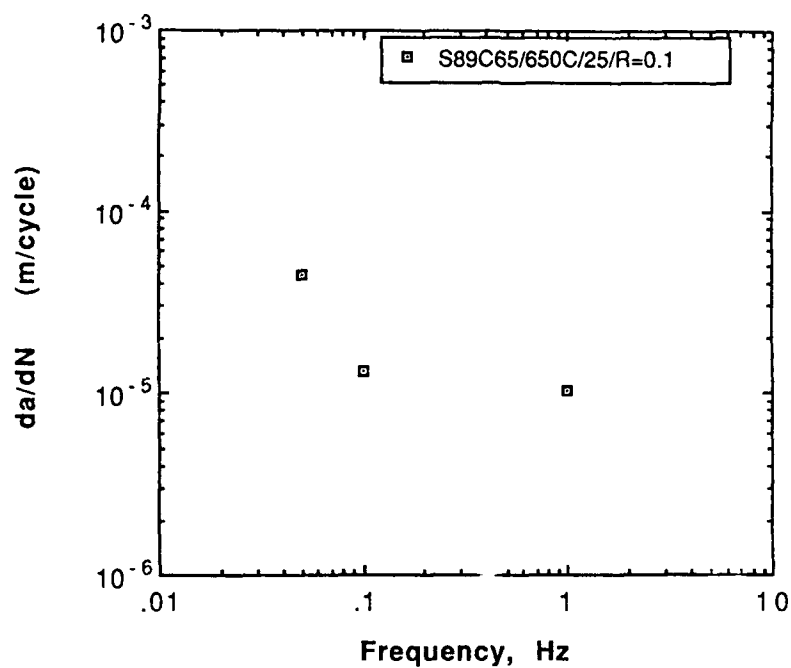


Figure 107. da/dN versus frequency for test conducted at a temperature of 650°C, K_{max} of 25 MPa√m, and R-ratio of 0.1.

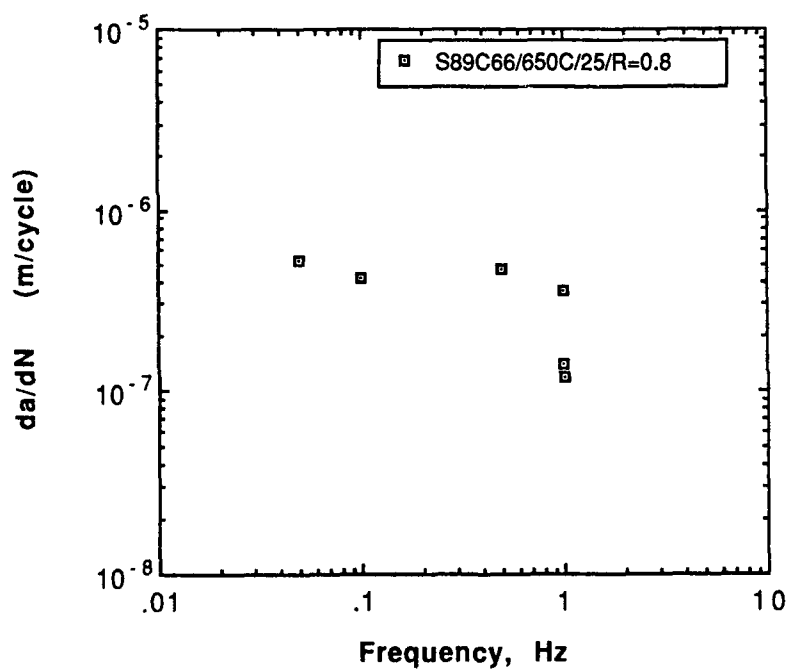


Figure 108. da/dN versus frequency for test conducted at a temperature of 650°C, K_{max} of 25 MPa√m, and R-ratio of 0.8.

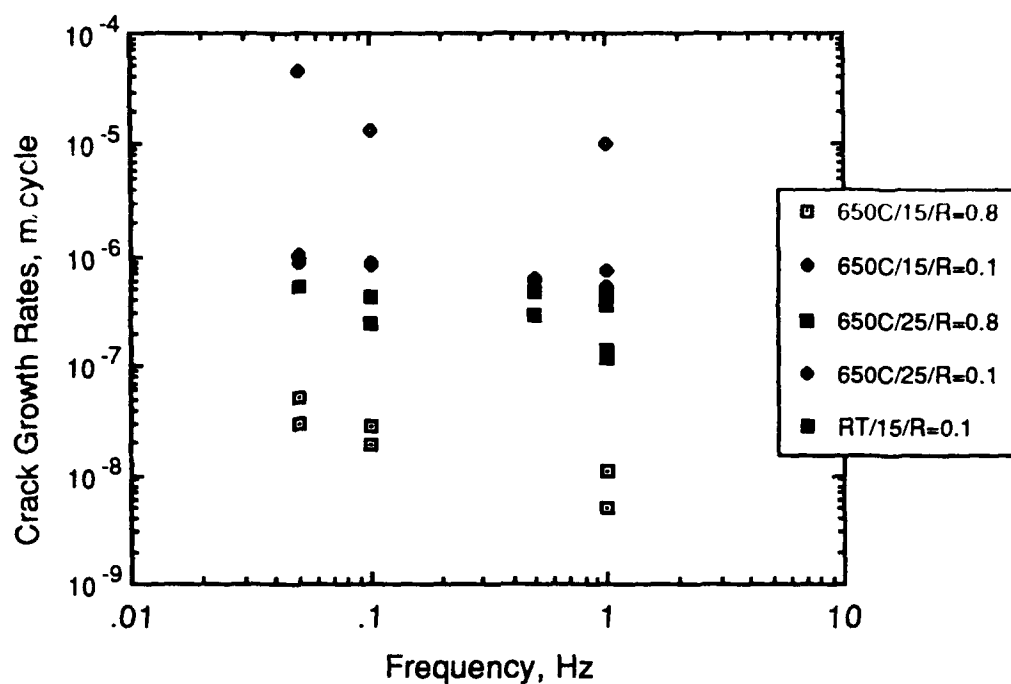


Figure 109. Summary of plots of da/dN versus frequency for test conducted under different set of conditions.

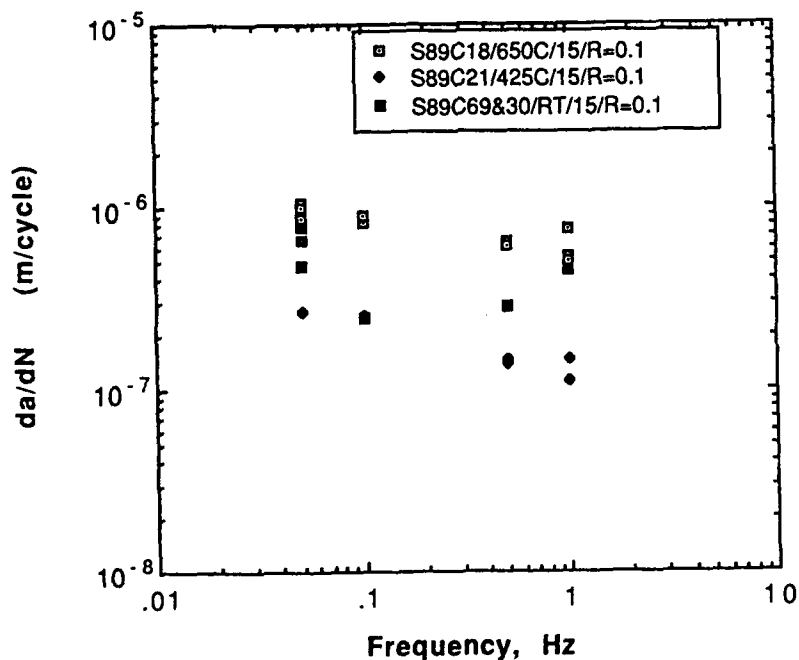


Figure 110. Effect of temperature on the da/dN versus frequency plots for tests conducted at $K_{max} = 15 \text{ MPa}\sqrt{\text{m}}$, $R = 0.1$.

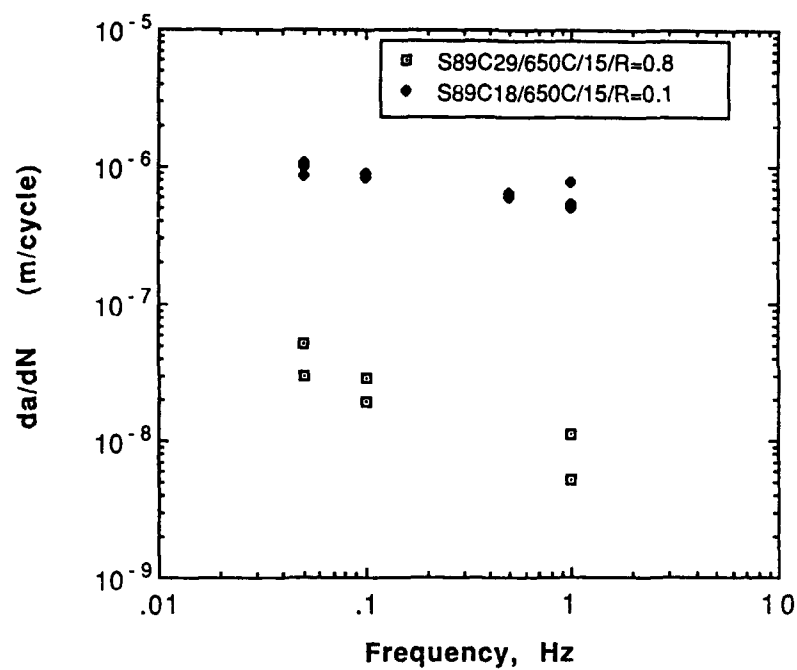


Figure 111. Effect of R-ratio on the da/dN versus frequency plots for tests conducted at 650°C and $K_{max} = 15 \text{ MPa}\sqrt{\text{m}}$.

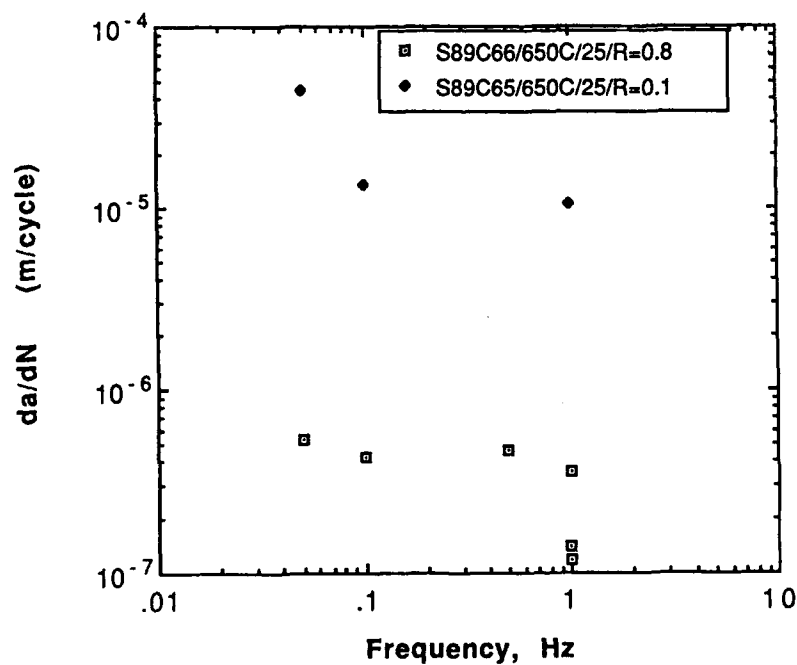


Figure 112. Effect of R-ratio on the da/dN versus frequency plots for tests conducted at 650°C and $K_{max} = 25 \text{ MPa}\sqrt{\text{m}}$.

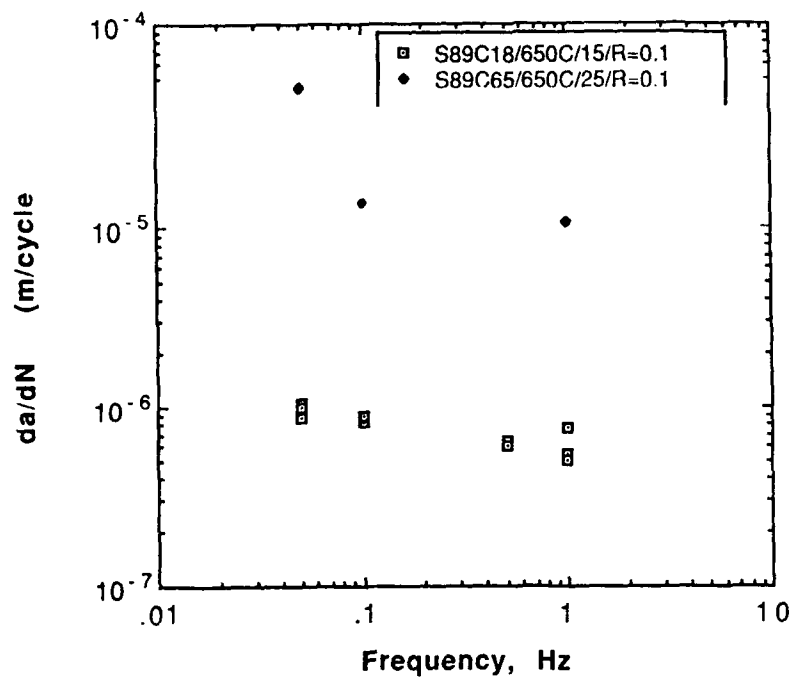


Figure 113. Effect of K_{max} on the da/dN versus frequency plots for tests conducted at 650°C and R-ratio=0.1.

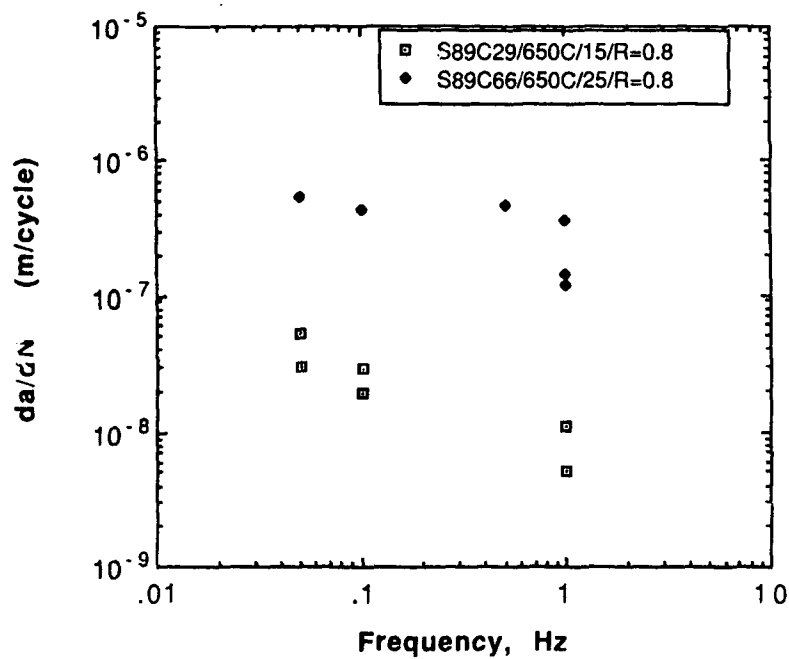


Figure 114. Effect of K_{max} on the da/dN versus frequency plots for tests conducted at 650°C and R-ratio=0.8.

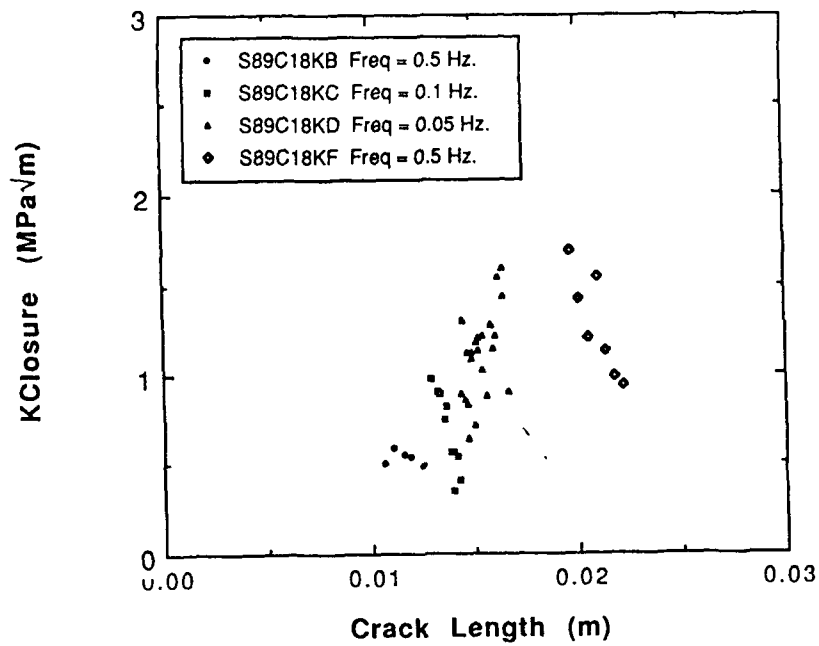


Figure 115. $K_{closure}$ versus crack length for fatigue crack growth tests conducted at constant K_{max} and constant R-ratio, but at different frequencies - specimen #S89C18

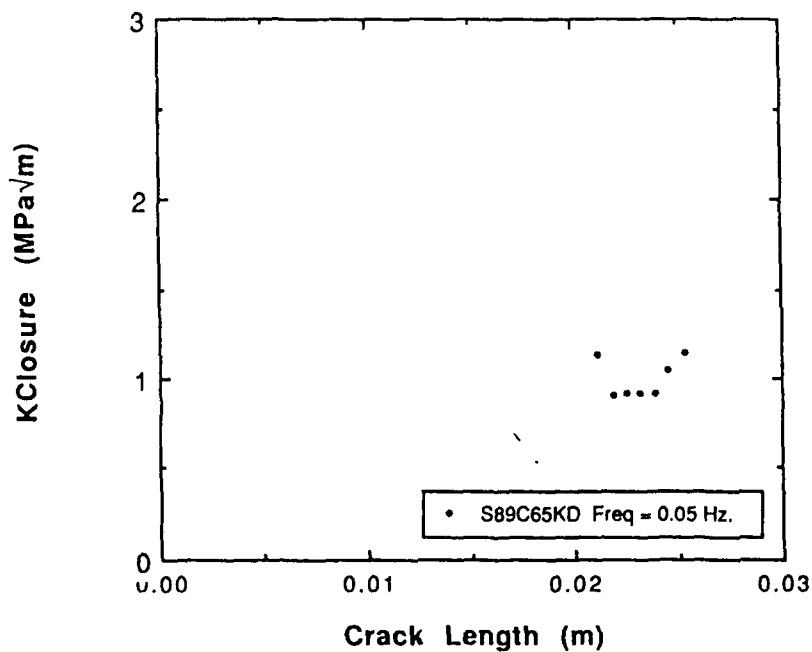


Figure 116. $K_{closure}$ versus crack length for fatigue crack growth tests conducted at constant K_{max} and constant R-ratio, but at different frequencies - specimen #S89C65

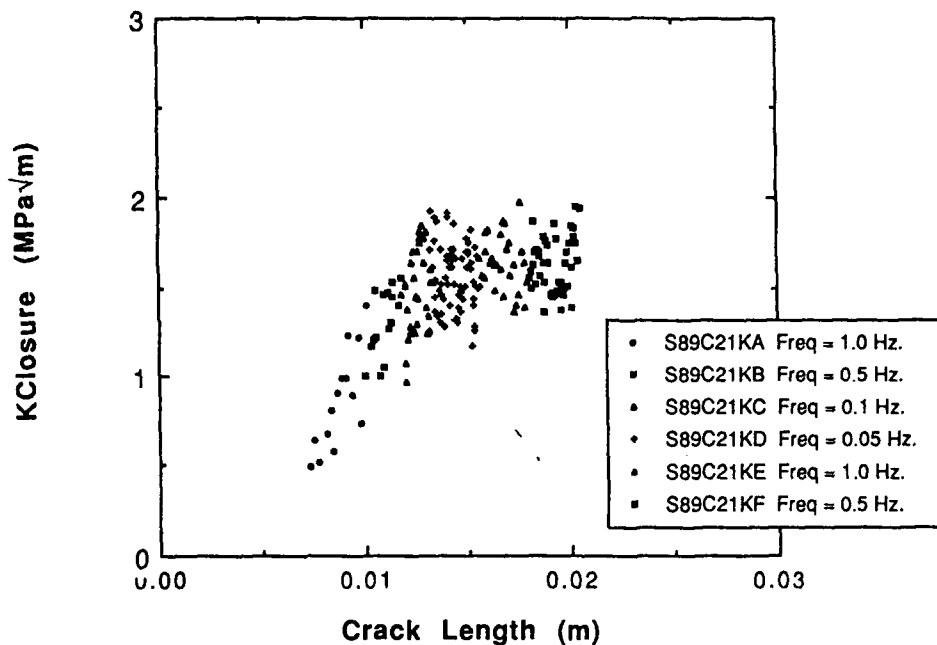


Figure 117. $K_{closure}$ versus crack length for fatigue crack growth tests conducted at constant K_{max} and constant R-ratio, but at different frequencies - specimen #S89C21

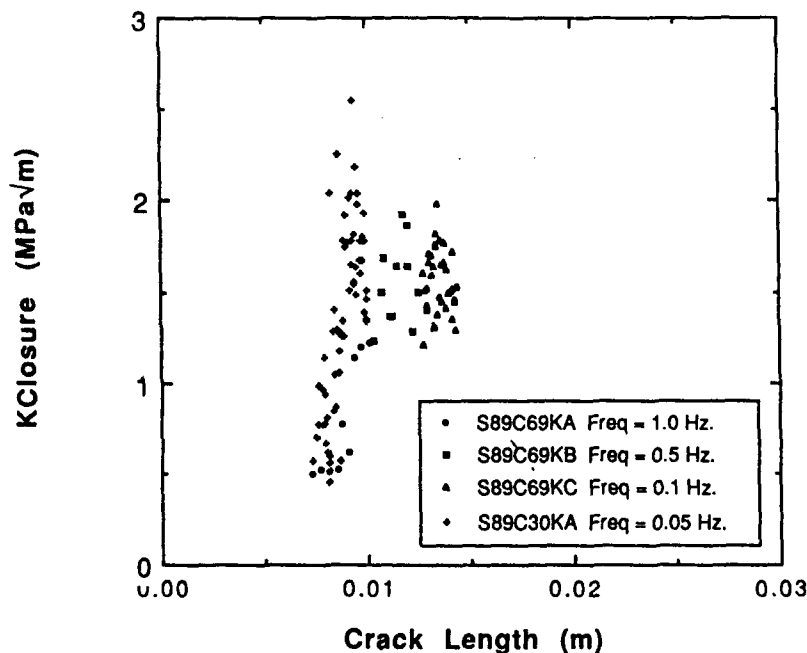


Figure 118. $K_{closure}$ versus crack length for fatigue crack growth tests conducted at constant K_{max} and constant R-ratio, but at different frequencies - specimen #S89C69&30